

VIRUS ATTACHMENT TO SURFACES: ASSESSING RELATIVE CONTRIBUTIONS
OF ELECTROSTATIC, VAN DER WAALS, AND ACID-BASE INTERACTIONS

By

Hien Thi Thu Dang

A DISSERTATION

Submitted to
Michigan State University
In partial fulfillment of the requirements
for the degree of

Environmental Engineering - Doctor of Philosophy

2018

ABSTRACT

VIRUS ATTACHMENT TO SURFACES: ASSESSING RELATIVE CONTRIBUTIONS OF ELECTROSTATIC, VAN DER WAALS, AND ACID-BASE INTERACTIONS

By

Hien Thi Thu Dang

Adhesion to surfaces plays an important role in determining pathogen transport and fate in the environment. Countertops, hospital walls, hair and skin are examples of surfaces of particular interest. While bacterial adhesion is relatively well understood, less is known about interactions of viruses with surfaces of different charges, hydrophobicities and morphologies. In this study, the attachment of bacteriophage MS2 and human adenovirus 40 (HAdV40) onto polyelectrolyte- and paint-coated surfaces has been investigated using an approach that combines experimental studies and theoretical modeling. The extended Derjaguin-Landau-Verwey-Overbeek (XDLVO) model was used to calculate the energy of virus-surface interaction. The theoretical predictions were validated in experiments that used quartz crystal microbalance with dissipation (QCM-D) to measure the mass of deposited viruses. The polyelectrolyte-coated surfaces were designed by assembling a polyelectrolyte multilayer (PEM) via alternate deposition of the negatively-charged poly(styrene-4-sulfonate) (PSS) and positively-charged poly(dimethyl diallyl ammonium chloride) (PDAD). The

paint-coated surfaces were prepared by spin-coating three household paints (water-based acrylic latex, water-based alkyd, and oil-based alkyd), which differed in terms of their chemical composition, surface charge and hydrophobicity. Experimentally observed trends in experiments MS2 deposition onto the polyelectrolyte –coated surfaces were consistent with XDLVO predictions: a) deposition onto the positively-charged surface was significantly (~ 5 to 6 times) higher than on a negatively charged one and b) deposition was enhanced at higher ionic strengths of the background electrolyte. The kinetics of deposition depended on the salinity: lower salinity led to faster deposition and a shorter time to steady-state. The data on kinetics of HAdV40 adhesion to the household paints was also in a qualitative agreement with predictions by the XDLVO theory. The quantitative discrepancies between QCM-D experiments and XDLVO theory were attributed to details of the surface morphology and the chemical heterogeneity of the deposited paint layer. For both viruses and all surfaces studied, the electrostatic and hydrophobic interactions were found to govern virus deposition behavior with van der Waals interactions playing a comparatively small role. The approach demonstrated in this study can guide the design of surfaces that resist virus adhesion. Polymeric coatings and paints so formulated should help reduce human exposure to viruses

Copyright by
HIEN THI THU DANG
2018

ACKNOWLEDGEMENTS

To my mom, thank you for all of your sacrifices in order to bring me out of poverty and into college and for always having been there for me as a best friend. If it was not for you, I would not be here.

To my advisor, Dr. Volodymyr Tarabara, thank you for giving me the great opportunity to come here to study in this wonderful school in the U.S. Without your great patience, guidance and support, I would not have reached the end of this journey.

To my committee members, Dr. Irene Xagorarakis, Dr. Rafael Auras and Dr. Wei Zhang, thank you all for being my committee members and for providing invaluable feedback and advice.

To my husband and child, thank you for being in my life to make it complete.

To the staff in the department of civil and environmental engineering at MSU, Lori Larner, Laura Post, Laura Taylor, Joseph Nguyen, thank you all for your administrative and technical support.

To all of my former and current labmates, thank you all for being such great friends and for your training, advice, and feedback during my program.

To all the sponsors that made it possible for me to study here: the National Science Foundation Partnerships for International Research and Education program under Grant IIA-1243433 and the Vietnam Education Foundation Fellowship

TABLE OF CONTENTS

LIST OF TABLES.....	ix
LIST OF FIGURES	x
CHAPTER 1: OUTLINE	1
CHAPTER 2: INTRODUCTION	3
2.1. Derjaguin-Landau-Verwey- Overbeek (DLVO) and extended DLVO (XDLVO) theories	5
2.2. The modified Derjaguin technique for a rough surface	10
2.3. Measurements using quartz crystal microbalance with dissipation.....	11
CHAPTER 3: ATTACHMENT OF HUMAN ADENOVIRUS 40 AND BACTERIOPHAGE MS2 ONTO HOUSEHOLD PAINTS	13
Abstract	13
3.1. Introduction.....	15
3.2. Materials and Methods	20
3.2.1 Reagents.....	20
3.2.2. Propagation, purification, and quantification of bacteriophage MS2 and human adenovirus 40.....	20
3.2.3. Preparation of the artificial respiratory fluid	21
3.2.4. Preparation of paint-coated surfaces	22
3.2.5. Quartz crystal microbalance with dissipation measurements	24
3.2.6. Zeta potential measurements.....	25
3.2.7. SEM images and elemental analyses for paint film surfaces	25
3.2.8. Measurement of paint layer thickness.....	26
3.2.9. Contact angle measurements	26
3.3. Results and Discussion	26
3.3.1. Surface properties of the paints: hydrophobicity and charge.....	26
3.3.2 Surface properties of HAdV40 and MS2: Hydrophobicity and charge	30
3.3.3 Characteristics of paint-coated surface: Morphology and elemental composition	30
3.3.4. DLVO and XDLVO energies of virus-paint interfacial interactions..	34
3.3.5. Deposition of viruses on paint-coated surfaces	43
3.3.6. Principal component analysis.....	51
3.4. Conclusions	55
CHAPTER 4: DEPOSITION OF BACTERIOPHAGE MS2 ONTO POLYELECTROLYTE-COATED SURFACES	57
Abstract	57
4.1. Introduction.....	59

4.2. Materials and Methods	63
4.2.1 Reagents.....	63
4.2.2 Propagation, purification and quantification of bacteriophage MS2.....	63
4.2.3. Preparation and characterization of polyelectrolyte-coated surfaces	65
4.2.4 QCM-D experiments.....	67
4.2.5. Nomenclature	68
4.3. Results and Discussion	69
4.3.1 Characteristics of polyelectrolyte multilayer coatings	69
4.3.2 XDLVO energy profiles for MS2-interactions with PEM surfaces	71
4.3.3 QCM-D measurements of MS2 deposition onto polyelectrolyte-coated surfaces.....	72
4.3.4. Principal component analysis.....	82
4.4. Conclusions	87
CHAPTER 5: SUGGESTED FUTURE RESERCH: ATTACHMENT OF AIRBORNE VIRUSES TO HUMAN SKIN AND PERSONAL CARE PRODUCTS AS A FUNCTION OF ENVIRONMENTAL PARAMETERS.....	88
5.1. Introduction.....	88
5.2. Experimental.....	90
5.2.1. Cosmetic products.....	90
5.2.2. QCM-D procedure	91
5.3. Objectives and hypotheses.....	93
APPENDICES.....	95
APPENDIX A Attachment of Human Adenovirus 40 and Bacteriophage MS2 onto Household Paints	96
APPENDIX B Deposition of Bacteriophage MS2 onto Polyelectrolyte-coated Surfaces	116
BIBLIOGRAPHY	129

LIST OF TABLES

Table 1: Composition of the three paints [89-91].	23
Table 2: Contact angles, calculated surface energy parameters, and free energy of the paint surfaces.....	29
Table 3: Elemental composition of the paints as determined by energy dispersive X-ray scattering (Figures A1-A3 in the Appendix A). a Silica signal comes from the QCM-D sensor	32
Table 4: Zeta potentials, hydrophobicity, and morphological characteristics of [PSS/PDAD] ₄ and [PSS/PDAD] _{4.5} surface coatings assembled from solutions of different background electrolyte concentrations (10 mM or 100 mM NaCl), rinsed, and exposed to either 10mM NaCl or 100 mM NaCl solutions.	70

LIST OF FIGURES

Figure 1: An example of XDLVO energy profile. The total interaction energy is a sum of Lifshitz van der Waals (LW), electrostatic double layer (EL) and acid-based (AB) interactions (source: Lin et al. [45]).	9
Figure 2: QCM-D system (source: q-sense.com)	12
Figure 3: Zeta potential as a function of pH for a) the three household paints and b) the two viruses (HAdV40 and MS2). The data sets for the viruses are adapted from studies by Shi et al. [13] and Chrysikopoulous et al. [32]. The vertical red lines mark two pH values (3.5 and 6.0) of the background NaCl electrolyte used in QCM-D experiments.	31
Figure 4: SEM images of planar view (A, B, C) and cross-section (D, E, F) for latex water-based paint (A, D), alkyd water-based paint (B, E), and alkyd oil-based paint-coated (C, F)	33
Figure 5: Profiles of DLVO and XDLVO energies of interaction between HAdV40 and paint surfaces in 1 mM NaCl: pH 3.5 (a, b, c) and pH 6.0 (d, e, f)	36
Figure 6: Profiles of DLVO and XDVO energy of interaction between HAdV40 and paint surfaces in 150 mM NaCl: pH 5.2 (a, b, c) and pH 7.2 (d, e, f)	37
Figure 7: Profiles of DLVO and XDLVO energy of interaction between MS2 and paint surfaces in 1 mM NaCl: pH 3.5 (a, b, c) and pH 6.0 (d, e, f)	41
Figure 8: Profiles of DLVO and XDLVO energy of interaction between MS2 and paint surfaces in 100 mM NaCl and pH 3.5	42
Figure 9: Kinetics of HAdV40 deposition onto the paint surface: 1 mM NaCl at pH 3.5 and pH 6.0 (b) and 150 mM NaCl at pH 5.2 (c) and pH 7.2 (d)	47
Figure 10: Kinetics of MS2 deposition onto the paint surfaces in 1 mM NaCl: pH 3.5 (a) and pH 6.0 (b) and in 100 mM NaCl at pH 3.5 (c)	50
Figure 11: Principal component analysis (PCA): factor loadings (a) and factor scores (b)	54
Figure 12: DLVO and XDLVO energy profiles of MS2 interaction with as-prepared (i.e. MS2-free) surfaces of 10-[PSS/PDAD] ₄ (a, b) and 100-[PSS/PDAD] ₄ (c, d) in 10 mM NaCl (a, c) and 100 mM NaCl (b, d) solutions. The	

profiles correspond to early stages of the phase 1 of MS2 deposition (see Figure 14).....73

Figure 13: DLVO and XDLVO energy profiles of MS2 interaction with as-prepared (i.e. MS2-free) surfaces of 10-[PSS/PDAD]_{4.5} (a, b) and 100-[PSS/PDAD]_{4.5} (c, d) in 10 mM NaCl (a, c) and 100 mM NaCl (b, d) solutions. The profiles correspond to early stages of phase 1 of the MS2 deposition (see Figure 15).....74

Figure 14: Kinetics of MS2 deposition onto (a) 10-[PSS/PDAD]₄, and (b) 100-[PSS/PDAD]₄ surfaces from solutions of different ionic strengths (*IMS2* = 10 mM or 100 mM NaCl). Corresponding dissipation data are given in Appendix B (Figure B5).....78

Figure 15: Kinetics of MS2 deposition onto (a) 10-[PSS/PDAD]_{4.5} and (b) 100-[PSS/PDAD]_{4.5} surfaces from solutions of different ionic strengths (*IMS2* = 10 mM or 100 mM NaCl). Corresponding dissipation data are given in Appendix B (Figure B6).....79

Figure 16: Principal component analysis (PCA): factor loadings (a) and factor scores (b).....86

Figure 17: Schematics of QCM-D with electro spray aerosol generator (source: Lee et al. [117]).....92

CHAPTER 1: OUTLINE

This dissertation is structured as a collection of several chapters. The present chapter (Chapter 1) outlines this structure and the contents of each chapter. Chapter 2 is the Introduction that describes the motivation for the present work, the overarching hypothesis, and the background information on research methods employed throughout this work. Chapters 3, and 4 are detailed accounts of two different projects that form the core of the dissertation. Each of these two chapters is a manuscript that, at the time of this writing, has been submitted to a journal. Chapter 5 offers suggestions for possible future research.

Chapter 2 provides an overview of viruses (e.g., norovirus (NoVs) and human adenoviruses (HAdVs)) as a threat to human health and focuses on virus adsorption to different surfaces as a possible route for transmitting viral infections. The Chapter describes the XDLVO theory as a predictive tool for understanding virus attachment to surfaces and provides background information on quartz crystal microbalance with dissipation (QCM-D) as the experimental technique for probing virus-surface interactions.

Chapter 3 describes a study on HAdV40 and bacteriophage MS2 attachment onto household paints. In this study, we employed QCM-D to study virus adsorption experimentally. Effects of virus properties (hydrophobicity, surface charge, and hydrodynamic size), solution chemistry (ionic strength and pH), and paint surface properties (hydrophobicity, surface charge, roughness) were

investigated. The XDLVO virus-surface interaction energies were used to predict virus adsorption and compare the predictions with experimental results obtained in QCM-D studies. The calculations accounted for the paint surface roughness using the modified Derjaguin technique. The work has established an approach to quantifying virus adhesion onto paints and can be helpful for formulating paints resistant to virus adhesion.

Chapter 4 presents a study on MS2 attachment to polyelectrolyte multilayer (PEM)-coated surfaces. As in Chapter 3, the approach combines numerical (XDLVO) modelling and experimental (QCM-D) studies. MS2 was either used directly from the stock for deposition experiment or further purified using precipitation with 6 KDa polyethylene glycol prior to the experiment. PEMs were in situ assembled on the QCM-D sensor surface. Effects of PEM properties (surface charge, hydrophobicity, roughness), PEM deposition conditions (ionic strength of the PEM deposition solution) and solution chemistry (ionic strength) of the MS2 suspension were investigated.

Chapter 5 is structured as an outline of a research proposal. Motivation for the proposed research is provided along with specific objectives and related hypotheses. The proposal relies on the use of QCM-D technique to explore virus deposition from air onto surfaces of practical importance (e.g., human skin, coating formed from lipstick and other personal care products, human and animal hair) as a function of environmental parameters (e.g. humidity) and virus properties.

CHAPTER 2: INTRODUCTION

Pathogens have been reported to account for approximately 38.6 million food-related illnesses per year in the U.S., of which 30.9 million illnesses (~80%) are caused by viruses. Noroviruses (NoVs) alone are responsible for approximately 23 million illnesses each year [1]. NoVs are also believed to be the top cause of waterborne diseases contributing to 45% outbreaks, followed by adenoviruses (24% outbreaks) in the U.S. [2]. Non-enveloped, single-strand RNA viruses, NoVs are among the smallest pathogens (27 to 32 nm in size). They infect humans of all ages [3], are extremely contagious and spread most commonly through the fecal-oral route [4]. They are the most common agent of gastroenteritis [1] and cause post-infectious irritable bowel syndrome [4].

HAdVs have the diameter in the 70 to 100 nm range and are non-enveloped double-strand DNA viruses. They have been associated with respiratory infections, gastroenteritis, pneumonia, ocular and genitourinary infections; their most common transmission pathways are with respiratory droplets, via contaminated food and water or through the fecal-oral route [2]. HAdV 40 and 41 have been reported to be among the most common causes for respiratory infections and gastroenteritis in children. As a part of the Seattle Virus Watch program, an early (1965 – 1969) study by Fox et al. [5] determined that HAdV caused 5% and 3% of infectious illnesses in infants and 4 years old children, respectively.

To understand virus transport and fate and thus reduce human exposure to viruses, numerous studies have been conducted on virus adsorption to different surfaces such as soils [6-8], organic matter [9, 10], membrane filters [11-14] and activated carbon [15, 16]. Thanks to the similarity between NoVs and the bacteriophage MS2, the latter is often used as a NoV surrogate in adsorption studies [7-9, 12]. Studies on HAdV adsorption are few and are mostly limited to the context of the virus adsorption and elution (VIRADEL) process [13, 17-31]. Employing bacteriophages as surrogates for human viruses avoids health risks and helps gain valuable data quickly. Yet, there is a need for studies with human viruses to validate predictions based on the prior work with phages and to discover virus-specific behaviors.

Adsorption studies show that virus properties such as surface charge [11, 12], hydrophobicity [10, 19, 23, 31-33], size and shape [10, 33, 34] and isoelectric point (IEP) [33] are significant controlling factors for virus adsorption. Virus morphology and can also have an impact on adsorption. For example, tail fibers are reported to promote virus adsorption [33] while protruding hydrophilic loops are found to hinder adsorption [9, 10, 35]. In addition to virus properties, environmental conditions such as ionic strength of the aqueous phase [29], pH [10], composition of the eluate (in tests on virus elution from surfaces) [19, 21, 23, 31] and the specific ions in the water matrix [19, 22, 23, 25] also significantly impact virus adsorption.

In our study, we investigated attachment of HAdV40 and MS2 (a surrogate for NoV) to paint-coated and polyelectrolyte (PEM)-coated surfaces. Three different household paints: latex and alkyd water-based and alkyd oil-based paints were spin-coated on a QCM-D sensor. Four different PEM films were assembled on QCM-D sensor surfaces by alternately depositing poly(sodium-4-styrenesulfonate) (PSS) and poly(diallyldimethylammonium chloride) (PDAD) using the layer by layer (LbL) technique. We hypothesized that (1) electrostatic and acid-base interactions control virus-surface interaction; (2) surface roughness enhances virus attachment, and (3) HAdV40 shows higher propensity to attach to surfaces than MS2 does. To test the hypotheses, virus deposition tests were conducted with surfaces of different charges and hydrophobicities exposed to virus solutions of varying ionic strengths and pH. The XDLVO theory was employed to interpret experimental results. Surface morphology was quantified by AFM imaging and accounted for in the XDLVO predictions via a modified Derjaguin model.

2.1. Derjaguin-Landau-Verwey- Overbeek (DLVO) and extended DLVO (XDLVO) theories

DLVO theory has been widely used to calculate the energy of interaction between various surfaces as a function of surface properties, properties of the medium and the distance that separate the surfaces [36, 37]. The classic DLVO theory includes Lifshitz van der Waals (*LW*) and electrostatic double layer (*EL*) interactions. The *EL* interactions are either attractive or repulsive depending on

electrical charge of the surfaces. The LW interactions are usually attractive and are longer-range than the EL interactions. Some studies demonstrated that the DLVO theory is only applicable to surfaces that are chemically inert [38-41] so the model does not accurately predict virus adhesion to surfaces where hydrogen and chemical bonds are involved. This limitation can be partly overcome by extending DLVO to include a short-ranged acid-base (AB) interaction thereby accounting for hydrogen bonding [39, 42]. AB interactions can be attractive (hydrophobic attraction) or repulsive (hydrophilic repulsion) and up to 10-100 times greater than electrostatic and van der Waals interactions [43].

According to the XDLVO theory [39], the total energy of interaction E_{slv}^{XDLVO} between a virus (v) and paint-coated surface (s) in aqueous medium (l) is a sum of Lifshitz van der Waals E_{slv}^{LW} , electrostatic double layer E_{slv}^{EL} , and acid-based E_{slv}^{AB} energies (Figure 1):

$$E_{slv}^{XDLVO} = E_{slv}^{LW} + E_{slv}^{EL} + E_{slv}^{AB} \quad (2)$$

In the expression above,

$$E_{slv}^{LW} = -\frac{Aa}{6d} \quad (3)$$

$$E_{slv}^{EL} = \pi\epsilon_r\epsilon_0a \left[2\psi_c\psi_s \ln\left(\frac{1+e^{-\kappa_D d}}{1-e^{-\kappa_D d}}\right) \right] + (\psi_c^2 + \psi_b^2) \ln(1-e^{-2\kappa_D d}) \quad (4)$$

$$E_{slv}^{AB}(d) = 2\pi a \lambda \Delta G_{d_0}^{AB} \exp\left(\frac{d_0 - d}{\lambda}\right) \quad (5)$$

where, a is the virus radius, d is the virus-surface separation distance [38, 43], ε_r is the dielectric constant of water ($\varepsilon_r = 79$), ε_0 is the relative permittivity in vacuum ($\varepsilon_0 = 8.854 \cdot 10^{12} \text{ CV}^{-1}\text{m}^{-1}$), ψ_c and ψ_b are the surface potentials of the virus and the surface, respectively, κ_D is the reverse Debye length, d_0 is the minimum separation distance ($d_0 = 0.158 \text{ nm}$), λ is the characteristic delay length of the AB interaction ($\lambda = 0.6 \text{ nm}$) [44] and A is the Hamaker constant given by eq. (4):

$$A = -12\pi y_0^2 \Delta G_{y_0}^{LW}. \quad (6)$$

The AB and LW free energies of adhesion per unit area, $\Delta G_{d_0}^{AB}$ and $\Delta G_{d_0}^{LW}$ are given by eqs. 7 and 8, respectively.

$$\Delta G_{d_0}^{AB} = 2\sqrt{\gamma_s^+}(\sqrt{\gamma_s^-} + \sqrt{\gamma_v^-} - \sqrt{\gamma_l^-}) + 2\sqrt{\gamma_s^-}(\sqrt{\gamma_s^+} + \sqrt{\gamma_v^+} - \sqrt{\gamma_l^+}) - 2(\sqrt{\gamma_s^+ \gamma_v^-} + \sqrt{\gamma_s^- \gamma_v^+}) \quad (7)$$

$$G_{d_0}^{LW} = 2(\sqrt{\gamma_l^{LW}} - \sqrt{\gamma_s^{LW}})(\sqrt{\gamma_v^{LW}} - \sqrt{\gamma_l^{LW}}) \quad (8)$$

where γ^+ is the electron acceptor parameter, γ^- is the electron donor parameter, γ^{LW} is the apolar surface energy component, and indices l, s, and v refer to

liquid, surface and virus. The surface energy components of the surface (γ_s^{LW} , γ_s^+ and γ_s^-) are calculated based on the measured contact angles, θ , of three probe liquids (DI, glycerol and diiodomethane) and the known surface tension components of the probe liquids (γ_l^{LW} , γ_l^+ and γ_l^-).

$$(1 + \cos\theta)\gamma_l^{TOT} = 2 \left(\sqrt{\gamma_s^{LW} \gamma_l^{LW}} + \sqrt{\gamma_s^+ \gamma_l^-} + \sqrt{\gamma_s^- \gamma_l^+} \right) \quad (9)$$

The hydrophobicity of a surface can be evaluated based on its free energy of cohesion when immersed in water (ΔG_{sls}). ΔG_{sls} is twice the interfacial tension γ_{sl} between the surface and water:

$$\Delta G_{sls} = -2\gamma_{sl} = 2 \left(\sqrt{\gamma_s^{LW}} - \sqrt{\gamma_l^{LW}} \right)^2 - 4 \left(\sqrt{\gamma_s^+ \gamma_s^-} + \sqrt{\gamma_l^+ \gamma_l^-} - \sqrt{\gamma_s^+ \gamma_l^-} - \sqrt{\gamma_s^- \gamma_l^+} \right) \quad (10)$$

A positive value of ΔG_{sls} indicates a hydrophilic surface while a negative value indicates that the surface is hydrophobic.

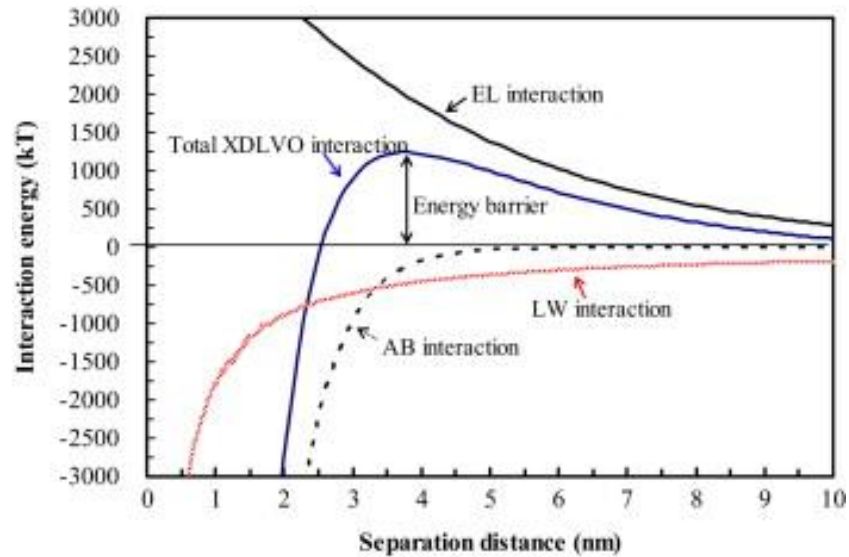


Figure 1: An example of XDLVO energy profile. The total interaction energy is a sum of Lifshitz van der Waals (LW), electrostatic double layer (EL) and acid-based (AB) interactions (source: Lin et al. [45]).

Viruses are not perfect spheres and the deviation from sphericity lowers the predictive power of the DLVO and XDLVO models. Although the theories have been extended to apply to some simple non-spherical shapes [46], the range of these – still idealized, morphologies are very limited. In this study, we focused on MS2 and HAdV40, both of which are relatively close to be spherical but neither is a perfect smooth sphere. MS2 has an icosahedral capsid and short hydrophilic polypeptide loops (~1 nm) protruding from it [35]. HAdV40 has short (~18 nm) and long fibers (~30 nm) terminated with globular knobs [47]. The size of HAdV40 was determined to be ~70 nm by TEM and ~90-120 nm by DLS [13, 48]. This suggested that TEM measurement failed to measure in low electron-density of the hydration layer region. Some studies showed that virus's fibers and tail interfere with adhesion leading to discrepancies between experimental results

and DLVO/XDLVO modeling predictions. Shi et al. [13] reported that the fibers of HAdV40 are longer than the Debye lengths at different pH in 1 mM NaCl and thus suggested that fibers enhanced HAdV40 adsorption to surfaces. Loops of MS2 are too short to have an impact on its ability to bind to surfaces [49]. They are also dense and hydrophilic [35] resulting in higher EL and AB repulsive forces and thus increased steric hinderance.

2.2. The modified Derjaguin technique for a rough surface

Studies on surface roughness [50-53] suggest that roughness enhances colloid deposition in the primary and secondary minima by lowering energy barrier and reducing hydrodynamic shear near the surface where colloid interactions occur. This leads to a modified Derjaguin technique where surface roughness is included in the calculation of XDLVO energies to predict virus adsorption.

The total interaction energy between a sphere and rough surface ($U_{SR}(d)$) at a separation distance d , is the sum of the sphere-asperity ($U_{SA}(d)$) and sphere-flat plate ($U_{SP}(d)$) interaction energies [50, 54].

$$U_{SR}(d) = \eta U_{SA}(d) + (1 - \eta) U_{SP}(d) \quad (11)$$

where η is the fraction of interactions between a sphere and asperity and $(1 - \eta)$ is the fractions of interaction between a sphere and flat plate. The value of η depends on the geometry of the rough surface. In our work, AFM imaging

indicated that roughness features on the painted surfaces had convex morphology (see Figure A5 in Appendix A) such that the following relationship [54] held for each virus-paint pair:

$$a < \left(\frac{\rho^2}{8r} - \frac{r}{2} \right) \quad (12)$$

where ρ is the asperity separation, r is the asperity radius, and a is the radius of the attaching colloid (virus in our case). Thus η is given by [54]:

$$\eta = \frac{\pi e^2}{\rho^2} \quad (13)$$

where $e = [(a + r)^2 - a^2]^{1/2}$.

2.3. Measurements using quartz crystal microbalance with dissipation

Virus deposition onto a surface can be quantified using QCM-D (Figure 2) as long as the QCM-D sensor can be coated with a material that appropriately represents the surface of interest. By detecting shifts in QCM sensor's vibration frequency, this technique can measure deposited mass with nanogram sensitivity and can offer insights into the viscoelastic behavior of the adsorbed layer by measuring dissipation shifts [55]. QCM-D has been used to study the attachment of bacteriophages (e.g., MS2 [56], T4D [57]), norovirus virus-like particle [58, 59], human viruses (e.g., adenovirus [60]), and pathogenic plant viruses (e.g., cowpea mosaic virus [61], maize chlorotic mottle virus [62]) to various surfaces such as polyelectrolyte multilayers [9, 57, 60, 61], clays [9, 56], bare QCM

crystals [56, 59, 63] or self-assembled monolayers [58, 61, 62, 64]. The efficiency of virus attachment to a QCM sensor increases with an increase in the ionic strength of the deposition solution and is facilitated in the presence of divalent cations [56, 59]. Studies on virus adsorption using QCM-D also point to differences in the adsorption behavior between different virus strains, possibly due to strain-to-strain variation in capsid surface properties (e. g. distribution of amino acid residues) [59, 64]. Armanious et al. [64] studied differences in adsorption behaviors of MS2, fr, GA and Q β bacteriophages that have similar sizes (28.6-29.4 nm outer diameter and 21.0-21.4 nm inner diameter) but different surface charges, hydrophobicity and morphologies. The consensus appears to be that virus adsorption is mainly governed by electrostatic, hydrophobic [64] and steric [9] interactions while van der Waals interaction is of secondary importance [64].



Figure 2: QCM-D system (source: q-sense.com)

CHAPTER 3: ATTACHMENT OF HUMAN ADENOVIRUS 40 AND BACTERIOPHAGE MS2 ONTO HOUSEHOLD PAINTS

Abstract

Attachment of bacteriophage MS2 and human adenovirus 40 (HAdV40) onto negatively and positively charged paint-coated surfaces were studied using quartz crystal microbalance with dissipation monitoring (QCM-D). Effects of pH and ionic strength on virus attachment were probed using virus suspensions in simple electrolyte solutions and in a model respiratory fluid. The Derjaguin-Landau-Verwey-Overbeek (DLVO) and extended DLVO (XDLVO) theories were used to predict virus adsorption. The paint-coated surfaces were prepared by spin-coating the paints on QCM-D sensors. Three household paints with distinct charge and hydrophobicity values were tested: water-based acrylic latex paint, water-based alkyd paint, and oil-based alkyd paint. The QCM-D results showed that HAdV40 favorably adsorbed to the painted surfaces, while the opposite was observed for MS2. An increase in ionic strength enhanced virus adsorption. The adsorption kinetics of HAdV40 underwent two distinct phases. Phase 1 was governed by virus-paint interaction and was largely attributed by hydrophobicity and charge of the paints. Phase 2 occurred when the surface was partly covered by the virus-covered surfaces and was dependent of ionic strength. The distinct phases were more clearly manifest for HAdV40. The XDLVO theory proved to be a better tool for predicting of virus adsorption than the DLVO theory, especially for deposition from high ionic strength solutions. Electrostatic and acid-base

interactions governed virus adsorption; while the van der Waals interaction played a relatively minor role . The roughness of the paint surface had negligible impact on the total XDLVO energy of virus-paint interaction. The principal component analysis (PCA) separated the data points in groups due to different charges of the paints and energy barriers of their XDLVO energy profiles.

3.1. Introduction

Human adenovirus (HAdV) has been recognized as one of the most common agents causing respiratory tract diseases and gastroenteritis in children. As a part of the Seattle Virus Watch program, an early (1965 – 1969) study by Fox et al. determined that HAdV caused 5% and 3% of infectious illnesses in infants and 4 years old children, respectively [5]. A recent study by Rocholl et al. [65] on respiratory viruses at the Primary Children's Medical Center in Salt Lake City, UT, showed that from December 2000 to May 2002 adenoviruses accounted for 7.5% of respiratory illness cases; in this study, 90% of the patients were 5 years old or younger.

According to the National Human Activity Pattern Survey, humans spend an average of 87 % time indoors [66]. The concentration of virus-like and bacterium-like particles in buildings is $\sim 10^5$ particles/m³, wherein the ratio of virus to bacteria is 0.9 ± 0.1 [67]. One can expect pathogen concentrations to be higher in hospitals and other locations where care is provided to infected individuals. In the U.S., 1.7 million cases of healthcare-associated infections leading to 99,000 deaths were reported in 2002 [68]. Contaminated surfaces such as clothes, walls and medical care instruments are considered to contribute to up to 40% of such infections [69].

To understand virus transport and fate, numerous studies have been conducted on virus adsorption to surfaces such as soils [6-8], organic matter [9, 10],

membrane filters [11-14] and activated carbon [15, 16]. To our knowledge, there have been no published work on virus attachment to paints, which is a very a common type of surface in hospitals and other indoor environments. Many commercially available paints are designed to be waterproof and contain biocidal materials. The hydrophobicity of the paints helps repel water but promotes adhesion of aqueous colloids including pathogens. At the same time, the biocide additives (e .g. silver, titanium dioxide, copper and zinc oxide, often in the form of nanoparticles) target bacterial, but not viral pathogens. In sum, common household paints are not designed to resist adhesion of or inactivate viruses.

There have been multiple studies on virus adhesion to various surfaces. Most of this work though employed bacteriophages such as MS2 [7-9, 12]; while adsorption of human viruses has been less explored. Adsorption of HAdV has been explored in the context of the virus adsorption and elution (VIRADEL) process [13, 17-31]. HAdV adsorption is mainly governed by electrostatic [13, 21-24] and hydrophobic [19, 23, 31] interactions with ionic strength [29], solution chemistry of the eluent [19, 21, 23, 31] and the composition of the water matrix [19, 22, 23, 25] all affecting the adsorption process. Shi et al. [13] studied HAdV40 recovery from tap and surface waters by cross-flow ultrafiltration and found that membranes with a higher negative charge and hydrophilicity afforded higher recoveries. In addition, using polyanions and surfactants to disrupt electrostatic and hydrophobic interaction between the virus and the membranes helped achieve nearly 100% efficacy of elution. Li et al. [23] studied HAdV5 adsorption to electropositive charged nanoalumina filters and negatively charged

HAWP filters. It was found that filters played an important role in virus adsorption; for example, nanoalumina filters helped recover 82-91 % infectious viruses at pH 6 and HAWP filters did 78-90 % infectious viruses at pH 9. With higher filter rates, nanoalumina filters had an advantage in recovering infectious viruses from large water volumes (up to 10 L). Therefore, the nanoalumina filters were considered more effective than the HAWP filters in terms of virus recovery, filter rates, pre-filtration and pH adjustment. Lambertini et al. [22] studied HAdV 41 recovery using glass wool filter and found that virus strain, water matrix and pH contributed to virus recovery, wherein virus adsorption peaked at pH 6.5 and then decreased dramatically at pH 7.5. The virus recovery was 70%, 14%, 19%, 21% and 29% for poliovirus, coxsackievirus B5, echovirus 18, adenovirus 41 and norovirus, respectively. Poliovirus recovery significantly differed in tap and well 1 waters, so did HAdV41 and poliovirus recoveries in tap and well 2 waters; while norovirus and HAdV40 recoveries were different in well 1 and 2 waters. HAdV41 and poliovirus adsorption peaked in the pH range of 6.0-6.5 and at pH 6.5, respectively and it decreased dramatically at pH 7.5 for HAdV41 and with increasing pH for poliovirus. A study by Wong et al. [49] revealed that HAdV had a much higher retention time than MS2, especially in high ionic strength, leading to a much lower HAdV recovery; for example HAdV recovery was reduced by 2 and 3 orders of magnitude at the IS of 10 and 1000 mM, respectively while MS2 recovery decreased by less than 30%.

Viruses can deposit onto painted walls as a result of direct contact with infected humans or from respiratory droplets produced by such persons. Respiratory

droplets can be an effective vector for pathogen transmission because they carry high viral load. A high concentration of adenovirus ($1.6 \cdot 10^6$ to $3.7 \cdot 10^8$ genome copies per mL (GC/mL)), one of the most common pathogens causing respiratory and gastroenteritis infections in humans, was found in respiratory tract secretions of patients with adenovirus pneumonia [70]. Children hospitalized with lower respiratory tract infections presented the adenovirus load of 10^4 to 10^9 GC/mL in nasopharyngeal aspirate [71]. TT virus was measured at a high load of $3.1 \cdot 10^7$ to $1.5 \cdot 10^{11}$ GC/mL in nasal samples of patients with acute respiratory diseases [72]. The number of droplets expelled was estimated to be 947 to 2085 droplets per cough [73], 112 to 6720 over 5 min of talking [73] and $\sim 10^6$ droplets per sneeze [74]. Yang et al. estimated that a patient with influenza A viruses could shed $1.8 \cdot 10^3$ PFU/m³ by a single cough [75]. Large droplets ($\geq 100 \mu\text{m}$) and are effectively removed by gravity while small droplets ($20 \mu\text{m}$) often dry out via evaporation and can shrink half their initial size in less than a second. Xie et al. [74] quantified droplet transport using the Wells evaporation-falling curve and showed that larger droplets (60 to $100 \mu\text{m}$) produced by sneezing, coughing and breathing could travel more than 6 m, 2 m and 1 m, respectively with the initial velocities of 50 m/s, 10 m/s, and 1 m/s, respectively before they completely evaporate.

Virus deposition onto a surface can be quantified using quartz crystal microbalance as long as the QCM sensor can be coated by a material that adequately represents the surface in question. By detecting shifts in QCM

sensor's frequency, this technique can measure mass with nanogram sensitivity and can offer insights into the viscoelastic behavior of the adsorbed layer by measuring dissipation shifts [55]. QCM-D has been used to study the attachment of bacteriophages (MS2 [9, 56, 64], T4D [57]), norovirus virus-like particle (VLPs) [58, 59], adenovirus [60], air borne viruses [63] and pathogenic plant viruses [61, 62] to various surfaces such as polyelectrolyte multilayers [9, 57, 60, 61], clays [9, 56], bare QCM crystals [56, 59, 63] or self-assembled monolayers [58, 61, 62, 64]. The efficiency of virus attachment to a QCM sensor increases with an increase in the ionic strength and is facilitated in the presence of divalent cations [56, 59]. The QCM-D results also point to differences in the adsorption behavior between different virus strains, possibly due to strain-to-strain variation in capsid surface properties (e. g. distribution of amino acid residues) [59, 64]. Armanious et al. [64] attributed differences in adsorption behaviors of MS2, fr, GA and Q β bacteriophages that have similar sizes (28.6-29.4 nm outer diameter and 21.0-21.4 nm inner diameter) but different surface charges, hydrophobicity and morphologies. The consensus appears to be that virus adsorption is mainly governed by electrostatic, hydrophobic [64] and steric [9] interactions while van der Waals interaction is of secondary importance [64].

In this study, attachment of two viruses with disparate physicochemical characteristics - bacteriophage MS2 and HAdV40 – to paint-coated surfaces was investigated by combining QCM-D measurements and XDLVO modeling of virus –surface interactions. The three household paints evaluated in this work are

compositionally different and present surfaces covering a range of electrical charges and energies.

3.2. Materials and Methods

3.2.1 Reagents

All the reagents used for this study were of high purity (>98%). DI water with a resistivity of 18.2 M Ω -cm was used to prepare all the solutions. Sodium polyphosphate (NaPP), sodium chloride, and diiodomethane were purchased from Sigma-Aldrich. Tween 80 was purchased from Fisher Scientific while glycerol was purchased from J. T. Baker.

3.2.2. Propagation, purification, and quantification of bacteriophage MS2 and human adenovirus 40

MS2 and HAdV40 were purchased from American Type Culture Collection (ATCC). To propagate MS2 (ATCC 15597-B1), an actively growing broth culture was prepared first by adding 100 μ L of *E. coli* incubating overnight in soy broth for 6 h at 37 $^{\circ}$ C. The broth culture was then spiked with 0.1 mL of the diluted phage suspension ($\sim 10^6$ plaque forming units per mL (PFU/mL)) and incubated overnight at 37 $^{\circ}$ C. The MS2 suspension was centrifuged at ~ 5000 rpm for 15 min to remove cellular debris from the culture broth [76]. The supernatant was filtered through a 0.22 μ m filter (Millex-GS, Merck Millipore) and then further purified by dialysis with a 100 kDa membrane (Float-A-Lyzer G2, Spectra/Por) [77, 78] in 1 mM NaCl for 24 h. During the dialysis, the buffer was exchanged

after the first 12 h. The MS2 concentration in the stock was measured to be $4 \cdot 10^{11}$ PFU/mL using the standard double agar layer method.

HAdV40 (ATCC VR-931) was propagated in A549 cells. To purify HAdV40, the virus suspension was dialyzed with a 100 kDa dialysis device (Spectra/Por) in 1 mM NaCl for 24 h. The buffer was exchanged after the first 12 h. The HAdV40 concentration in the stock was measured using a quantitative real-time PCR (qPCR) and was determined to be $\sim 10^{10}$ GC/mL.

3.2.3. Preparation of the artificial respiratory fluid

Human adenovirus concentration ($\sim 10^8$ GC/mL), pH value (7.2) and salinity (150 mM NaCl) in the model RF mimicked those reported for human RF [73, 75, 79]. The pH value of patients' RF depends on their medical status [80], including asthma [81, 82] and smoking [83]; we selected pH 7.2 [84, 85] as an average pH measured from the patients infected with an adenovirus. We also used pH 5.2, the value typical for patients with acute asthma [82]. The mass concentration of proteins in human RF was reported to be 76.3 ± 18.2 g/L [79], which is $\sim 3 \cdot 10^6$ larger than that of the adenovirus. This leaves QCM-D unable to detect mass change of adsorbed virus separately from that of adsorbed protein. Therefore, we did not include protein in the model RF.

3.2.4. Preparation of paint-coated surfaces

The three Marquee brand (Behr Process Co.) paints used in this study were exterior semi-gloss ultrapure white No. 5450 (a water-based latex paint), exterior semi-gloss enamel white base No. 3900 (water-based alkyd paint), and interior/exterior semi-gloss enamel white No. 3800 (oil-based alkyd paint). The paints had different solvents and binders and thus presented a range of hydrophobicities and charges (Table 1). Based on % solids by weight and weight per gallon values provided by the manufacturer [86-88], the dried paint density was calculated to be 1.59, 1.67 and 1.79·g·cm⁻³ for latex water-based, alkyd water-based and alkyd oil-based paints, respectively.

To produce a thin paint film for QCM-D measurements, the as-purchased paints were diluted by a factor of 100. The water-based paints were diluted with DI water while the oil-based paint was diluted with light distillate (petroleum). Prior to spin-coating, the diluted paints were gently shaken for at least 2 h on a shaker. The diluted paint (0.5 mL) was then pipetted onto a clean QCM sensor. The paint-covered sensor was immediately spin-coated at 1500 rpm for 20 s and then heated in an oven at 80 °C for 30 min to remove the solvent. The annealed paint-coated sensors were used in QCM-D measurements of virus attachment.

Table 1: Composition of the three paints [89-91].

Component		Latex water-based exterior paint	Alkyd water-based exterior paint	Alkyd oil-based interior/exterior paint
Binder (film former)		Acrylic latex	Alkyd	Alkyd
Solvent (thinner)		Water	Water	Distillates (petroleum), hydrotreated light, kerosene
Pigments and fillers	TiO ₂	10 - 30 %wt	10 – 30 %wt	10 – 30 %wt
	SiO ₂ (amorphous)	1 – 5 %wt	1 – 5 %wt	1 – 5 %wt
	Al(OH) ₃	1 – 5 %wt	1 – 5 %wt	none
	CaCO ₃	none	None	1 – 5 %wt
	Mg ₃ Si ₄ O ₁₀ (OH) ₂	none	None	1 – 5 %wt
Additives		2-ethylhexyl benzoate (1 – 5 %wt)	Nepheline syenite (1 – 5 %wt)	none

3.2.5. Quartz crystal microbalance with dissipation measurements

The QCM-D E4 system was used to measure changes in mass on the quartz crystal surface and viscoelastic properties of the deposited layer via frequency and dissipation shifts, respectively. Prior to measurement, gold QCM-D sensors were soaked in a 5:1:1 mixture of DI water, hydrogen peroxide (30%) and ammonia (25%) at 75 °C for 5 min. The sensors were then rinsed with DI water, dried in N₂ and cleaned by O₃ for 20 min to remove hydrocarbon contaminants. The cleaned sensors were mounted into the flow module and the resonance frequency in air was determined. This was followed by a 5-min measurement to establish a stable baseline. This step was also repeated for the annealed paint-coated sensors. The frequencies acquired for the clean and annealed coated sensors were fitted into the Sauerbrey equation [92] to determine the thickness of the paint films based on the measured change in mass per unit surface area, Δm (ng·cm⁻²):

$$\Delta m = -\frac{C\Delta f}{n} \quad (1)$$

where C is the mass sensitivity constant ($C = -17.7 \text{ ng}\cdot\text{Hz}^{-1}\cdot\text{cm}^{-2}$), n is the overtone number ($n = 3$), and Δf is the frequency shift (Hz). The thickness of the paint film was calculated by dividing Δm by the paint density (ng cm⁻³).

QCM-D tests were carried out at 25 °C in a continuous flow mode at a flow rate of 0.15 mL/min using a digital peristaltic pump (IPC, 4 channels, ISMATEC). To

acquire QCM resonances, paint-coated sensors were first contacted with NaCl solution of the ionic strength (10 or 100 mM) that matched that of the virus suspension to be used in the QCM-D measurement that followed. A stable baseline was established and maintained for at least 5 min before the surfaces were challenged with a virus suspension. The MS2 and HAdV40 stocks were diluted to obtain a concentration of $4 \cdot 10^8$ PFU/mL and 10^7 GC/mL, respectively. The pH of the virus suspension was adjusted with 1 mM HCl and 1 mM NaOH. The virus suspension was also adjusted for ionic strength at 1, 100 and 150 mM NaCl. The QCM-D measurement was carried out for 1 h with frequency and dissipation shifts recorded every 1 min.

3.2.6. Zeta potential measurements

The ζ -potential values for paint surfaces were measured using an electrokinetic analyzer (EKA, Anton Paar) as a function of pH. The paints were coated on glass slides and then dried at room temperature for 7 days as recommended by the manufacturer. The pH values tested were 2.5, 3.5, 4.0, 5.0, 6.0, 7.0, 8.0, 9.0, and 10.0. Every ζ -potential measurement was carried out three times.

3.2.7. SEM images and elemental analyses for paint film surfaces

The paint-coated surfaces were imaged using JEOL 7500F scanning electron microscope (SEM). Energy dispersive X-ray scattering (EDS) was employed to assess the chemical makeup of the coatings. The films were mounted face-up on aluminum stubs using double-stick carbon tape. A small drop of carbon

suspension cement (when imaging top surfaces) or a thin coat (~2.7 nm) of Iridium (for imaging sample cross-sections) was used to form conducting bonds between the film and the stub.

3.2.8. Measurement of paint layer thickness

The thickness of paint-coated films was also estimated based on SEM images of film cross-sections. To expose a cross-section of the film, the paint-coated sensor was fractured with a pair of tweezes. The sample was then mounted on a stub with epoxy and then coated with Iridium to make it conductive.

3.2.9. Contact angle measurements

The samples were prepared as described in section 2.7. Contact angles of DI water, glycerol, and diiodomethane on the dried surfaces were then measured using a goniometer (model 250, Ramé-Hart). Contact angle values were calculated by DROPimage Advanced software based on recorded droplets shapes. Every measurement was repeated at least twice.

3.3. Results and Discussion

3.3.1. Surface properties of the paints: hydrophobicity and charge

Based on the measured values of contact angles the components of the surface energy and free interfacial interaction energies of the paints were computed (Table 2). The square root of the electron donor parameter ($\sqrt{\gamma^+}$) was calculated

to be very small and negative (from -1.1 to -2.1) so the value of γ^+ was assumed to be zero. Negative values of $\sqrt{\gamma^+}$ or $\sqrt{\gamma^-}$ are often reported for microbial cell surfaces due to hydration [93, 94]; this is more likely to occur for surfaces that have higher γ^{LW} and lower water contact angle values. Hwang [94] demonstrated that negative $\sqrt{\gamma^+}$ and $\sqrt{\gamma^-}$ are also calculated for solid surfaces depending on the choice of the apolar liquid in contact angle measurements. The zero (or very close to zero) value of γ^+ makes paint surfaces monopolar and leads to the zero value of the polar component, γ^{AB} , ($\gamma^{AB} = \sqrt{\gamma^- \gamma^+}$, of the total surface energy. Comparing the electron acceptor parameter (γ^-) of different paints, they ranked in the following order of decreasing basicity: alkyd water-based paint ($\gamma^- = 31.6$ mJ/m²) > latex water-based paint ($\gamma^- = 28.4$ mJ/m²) > alkyd oil-based paint ($\gamma^- = 11.9$ mJ/m²). With $\gamma^{AB} = 0$, the total surface energy (γ^{tot}) is equal to the apolar surface energy component (γ^{LW}): $\gamma^{tot} = \gamma^{LW} + \gamma^{AB} \cong \gamma^{LW}$).

While the hydrophobicity of a surface can be roughly evaluated based on its contact angle with water, a more accurate measure of hydrophobicity is given by the free energy of interfacial interaction (ΔG_{sls}) of two surfaces, identical to the one in question, when immersed in water. The negative sign of ΔG_{sls} indicates that the surface is hydrophobic. The absolute value of ΔG_{sls} is proportional to the degree of hydrophobicity or hydrophilicity. As shown in Table 2, the paints ranged from strongly hydrophobic ($\Delta G_{sls} = - 37.9$ mJ/m² for alkyd oil-based paint) to weakly hydrophobic ($\Delta G_{sls} = - 1.6$ mJ/m² for alkyd water-based paint).

Figure 3a shows zeta potential values of the three paints in 1 mM NaCl as functions of pH. The isoelectric point (pI) of the oil-based paint is ~ 4.5 while the pI values of the two water-based paints are both ~ 2.9.

Table 2: Contact angles, calculated surface energy parameters, and free energy of the paint surfaces

Parameter	Latex water-based paint	Alkyd water-based paint	Alkyd oil-based paint
Contact angle ($^{\circ}$) with probe liquids			
H ₂ O	96.3 ± 2.5	78.5 ± 1.6	82.5 ± 1.0
Glycerol	110.4 ± 0.5	93.3 ± 4.0	84.7 ± 1.3
Diiodomethane	69.8 ± 2.4	47.2 ± 2.3	39.0 ± 1.6
Surface energy parameter (mJ/m ²)			
γ^{LW}	23.0 ± 1.6	38.5 ± 1.5	40.3 ± 0.8
γ^{+}	0.0	0.0	0.0
γ^{-}	15.9 ± 4.1	26.5 ± 2.6	11.9 ± 2.0
γ^{AB}	0.0	0.0	0.0
γ^{tot}	23.0 ± 1.6	38.5 ± 1.5	40.3 ± 0.8
Free energy of interfacial surface-surface interaction in water $\Delta G_{s/s}$ (mJ/m ²)	-22.1 ± 10.7	-2.74 ± 4.6	-37.9 ± 6.2

3.3.2 Surface properties of HAdV40 and MS2: Hydrophobicity and charge

Figure 3b shows zeta potential values of the two viruses (HAdV40 and MS2) in 1 mM NaCl as functions of pH. The pI values for HAdV40 and MS2 were reported to be ~ 4.3 [13] and 3.1 [95], respectively. Based on the pI estimates for the viruses and the paints, one can identify pH ranges for each virus-paint pair where the virus and the paint possess charges of opposite signs making the electrostatic interaction attractive. In the case of the oil-based paint, such pH windows are 3.1 – 4.2 and 4.2 – 4.3 for MS2 and HAdV40, respectively. In the case of the water-based paints, the pH windows of favorable electrostatic interactions are 2.9 – 3.1 and 2.9 – 4.3, for MS2 and HAdV40, respectively.

3.3.3 Characteristics of paint-coated surface: Morphology and elemental composition

Paint film thicknesses calculated from the Sauerbrey equation (eq. (1)) are 37 ± 25 , 42 ± 30 , and 45 ± 26 nm for the latex water, alkyd water, and alkyd oil-based paints, respectively. These values were calculated by dividing the total weight of paints by its coverage area and thus represent an average thickness for an entire film. Due to the difficulty of measuring thickness for such a thin layer on areas covered with binders only, the measured thickness represents only an average height of accumulated pigments.

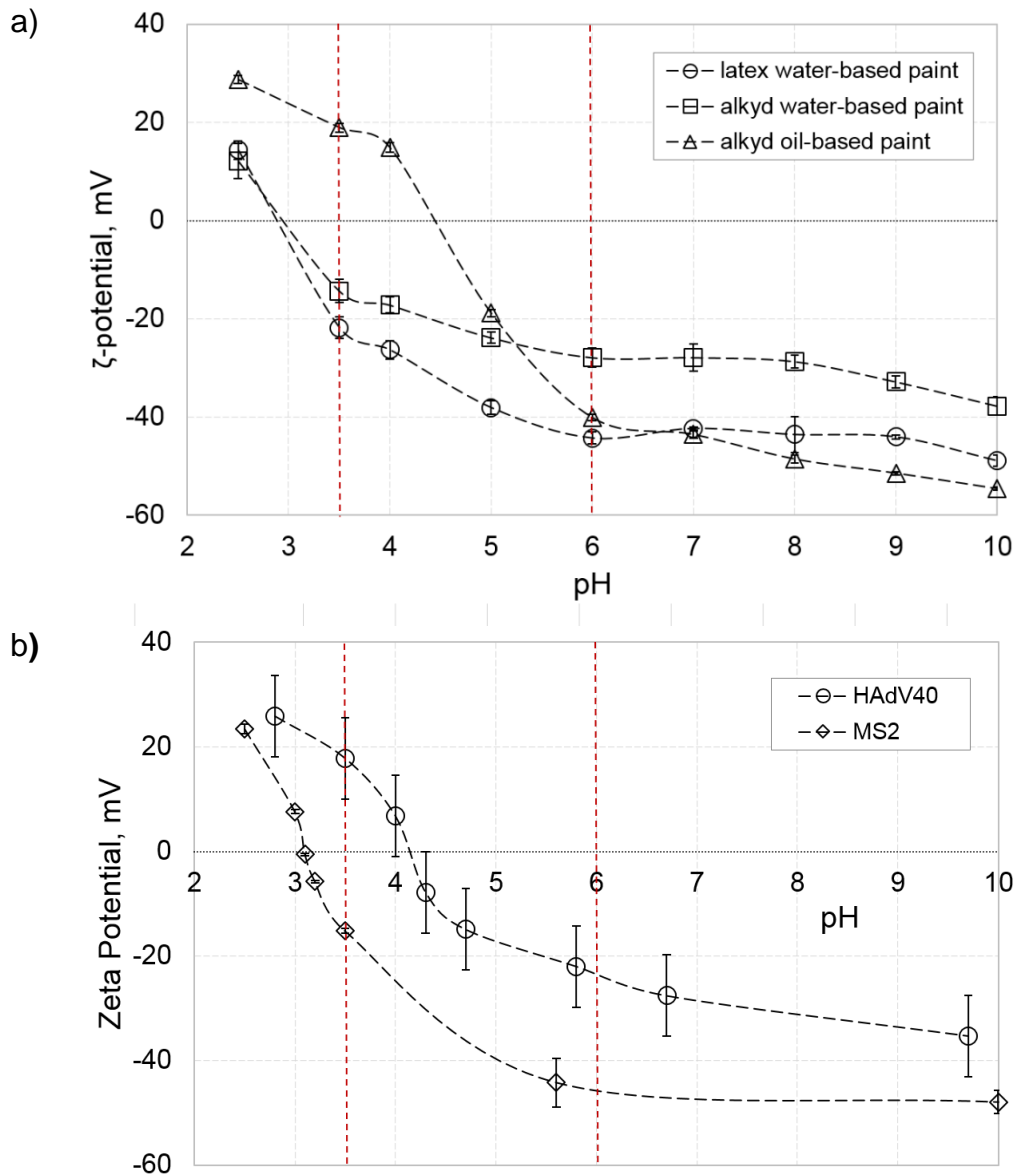


Figure 3: Zeta potential as a function of pH for a) the three household paints and b) the two viruses (HAdV40 and MS2). The data sets for the viruses are adapted from studies by Shi et al. [13] and Chrysikopoulous et al. [32]. The vertical red lines mark two pH values (3.5 and 6.0) of the background NaCl electrolyte used in QCM-D experiments.

Table 3: Elemental composition of the paints as determined by energy dispersive X-ray scattering (Figures A1-A3 in the Appendix A).
 a Silica signal comes from the QCM-D sensor

Element	Latex water-based paint		Alkyd water-based paint		Alkyd oil-based paint	
	Filler	Matrix	Filler	Matrix	Filler	Matrix
Ti	3.4 - 37.9	0.6	0.8 - 11.0	-	0 - 11.5	
Al	0.6 - 7.9	1.2	1.3 - 8.2	-	-	
Si ^a	1.7 - 18.7	37.1	24.3 - 34.6	44.9	0.3 - 19.1	45.4
C	5.5 - 65.4	51.8	13.0 - 32.9	46.5	16.7 - 34.6	44.7
O	11.9 - 47.0	9.4	20.3 - 46.5	8.5	34.6 - 50.3	9.9
Ca				-	0 - 32.4	-
Mg				-	0.3 - 2.4	-
Na			- 7.2	-	-	-

SEM images (Figure 4) as well as EDS elemental analysis (Table 3; also see Figures A1-A3 in the Appendix A) show a thin layer of the binder with protruding particles of the pigment material. Spin coating a thicker layer on the QCM-D sensor would have achieved a smoother paint surface; however, such heavier coating would have decreased the sensitivity of the QCM-D method or made QCM-D measurements impossible [96]. For example, when the paint solutions prepared for spin-coating were diluted less than 50-fold it was impossible to establish a baseline for QCM-D measurements.

The pigment particles were distributed evenly over the coated surfaces. The prevalent component of the matrix (the area of the surface without the pigment particles) was carbon (Table 3), a major constituent of the binder material.

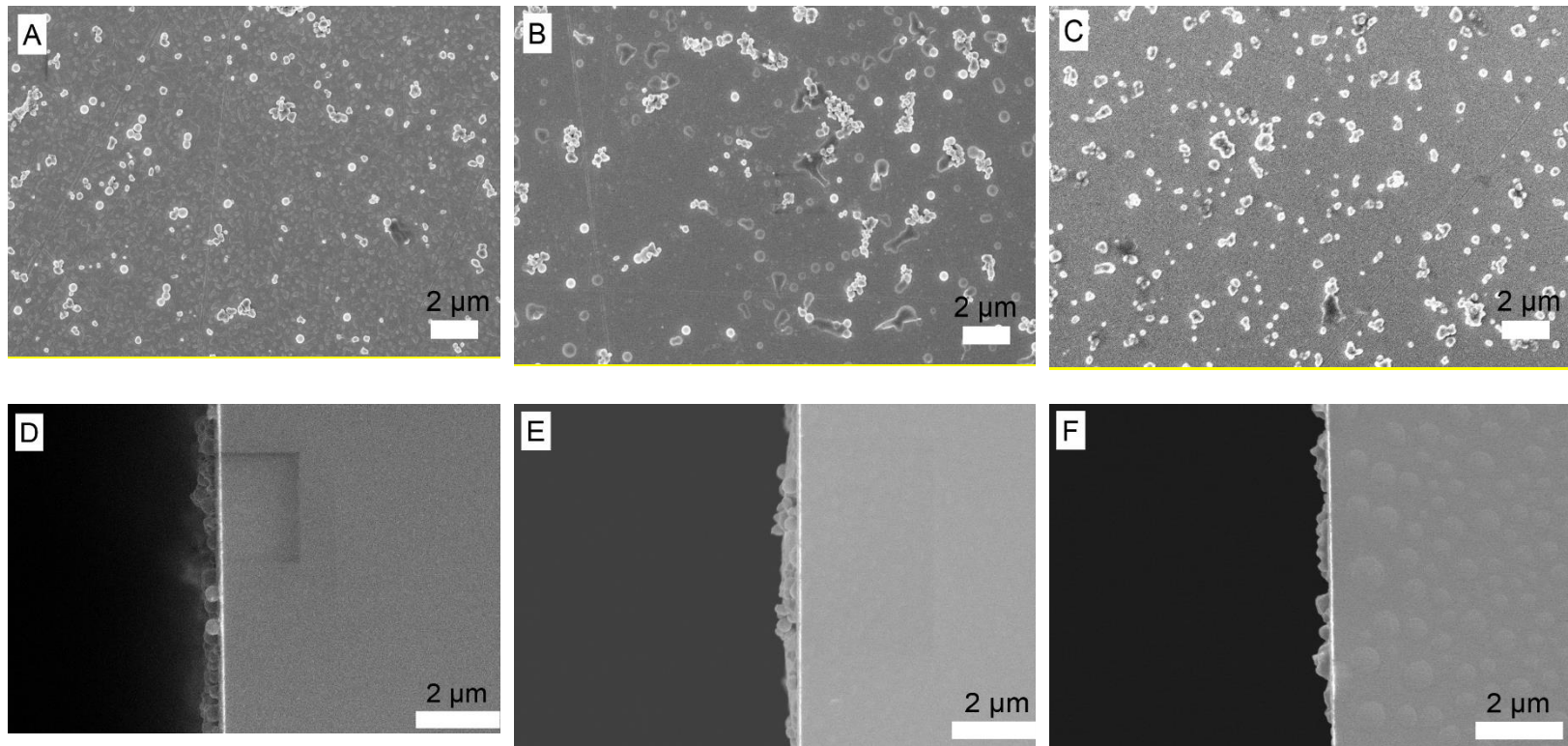


Figure 4: SEM images of planar view (A, B, C) and cross-section (D, E, F) for latex water-based paint (A, D), alkyd water-based paint (B, E), and alkyd oil-based paint-coated (C, F)

Based on the SEM images (Figure 4), the average paint film thickness was estimated to be $\sim 232 \pm 126$, 274 ± 115 , and 217 ± 88 nm, for the latex water, alkyd water, and alkyd oil-based paints, respectively

3.3.4. DLVO and XDLVO energies of virus-paint interfacial interactions

3.3.4.1. Human adenovirus 40

Figure 5 shows the total energy of DLVO and XDLVO interfacial interaction between HAdV40 and painted surfaces in 1 mM NaCl and pH 3.5 and 6.0. The calculated LW interaction is attractive for all the paints; of which it is the most attractive for alkyd oil-based paint, followed by the alkyd water-based paint and the least attractive for the latex water-based paint. The acid-base interaction of HAdV40 and each paint is attractive and is highest for the most hydrophobic ($\Delta G_{sls} = -37.9$ mJ/m², Table 2) oil-based paint.

In 1 mM NaCl and pH 3.5 (Figure 5a, b, c), the positively charged HAdV40 ($\zeta = 17.8$ mV) is electrostatically repulsive to alkyd oil-based paint ($\zeta = 18.9$ mV) and electrostatically attractive to both alkyd water ($\zeta = -14.3$ mV) and latex water ($\zeta = -21.8$ mV) paints (Figure 3a). The DLVO and XDLVO profiles both predict attractive virus interaction for the water-based paints. They also predict unfavorable adsorption for the oil-based paint by showing energy barriers ($\Phi_{max}^{DLVO} = 12.67$ at ~ 2.6 nm, $\Phi_{max}^{XDLVO} = 11.2$ kT at ~ 4.8 nm) and shallow secondary minima ($\Phi_{min2} = \sim 0.1$ kT at ~ 67 nm). The AB interactions change the DLVO energy profiles in short distances by lowering both the primary minima

of all the paints and the energy barrier of the oil-based paint by approximately 1.5 kT. In this case, EL interactions suppressed AB interactions in prediction of virus adsorption.

In 1 mM NaCl and pH 6.0 (Figure 5d, e and f), the negatively charged HAdV40 ($\zeta = -23.0$ mV) is electrostatically repulsive all paints as they too carry a negative charge ($\zeta = -44.3$ mV, -40.1 mV, -27.9 mV for latex water, alkyd oil, and alkyd water paints, respectively). The DLVO and XDLVO both display energy barriers ($\Phi_{max} > 24$ kT) and shallow secondary minimum ($\Phi_{min2} \leq 0.1$ kT). Though the AB interactions lower the DLVO energy profiles in short distances, including the primary minimum and energy barriers (by approximately 4 kT), both the DLVO and XDLVO profiles agree on predicting unfavorable HAdV40 adsorption for all the paints. AB interactions again do not appear to dominate virus adsorption in low ionic strength.

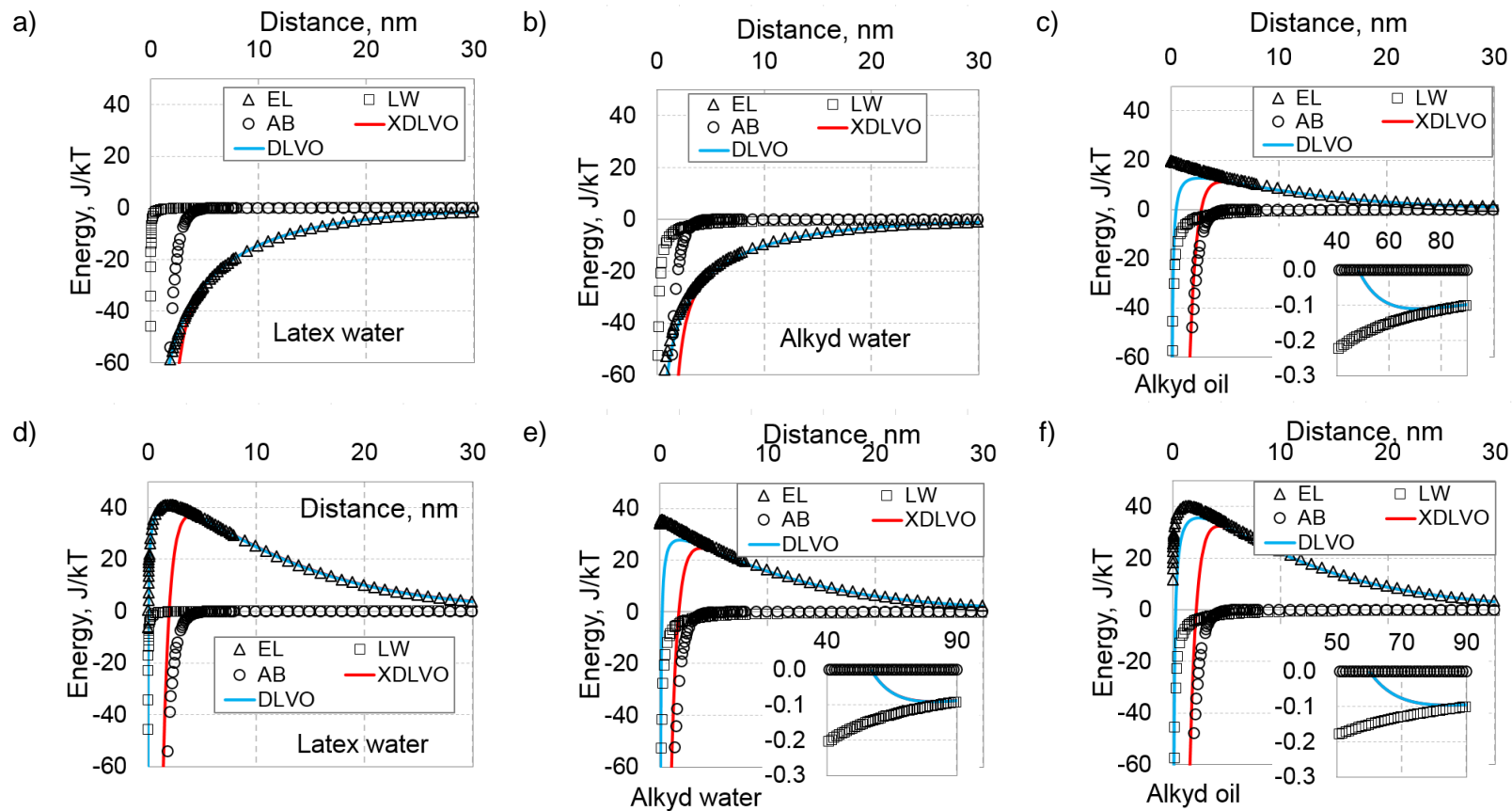


Figure 5: Profiles of DLVO and XDLVO energies of interaction between HAdV40 and paint surfaces in 1 mM NaCl: pH 3.5 (a, b, c) and pH 6.0 (d, e, f)

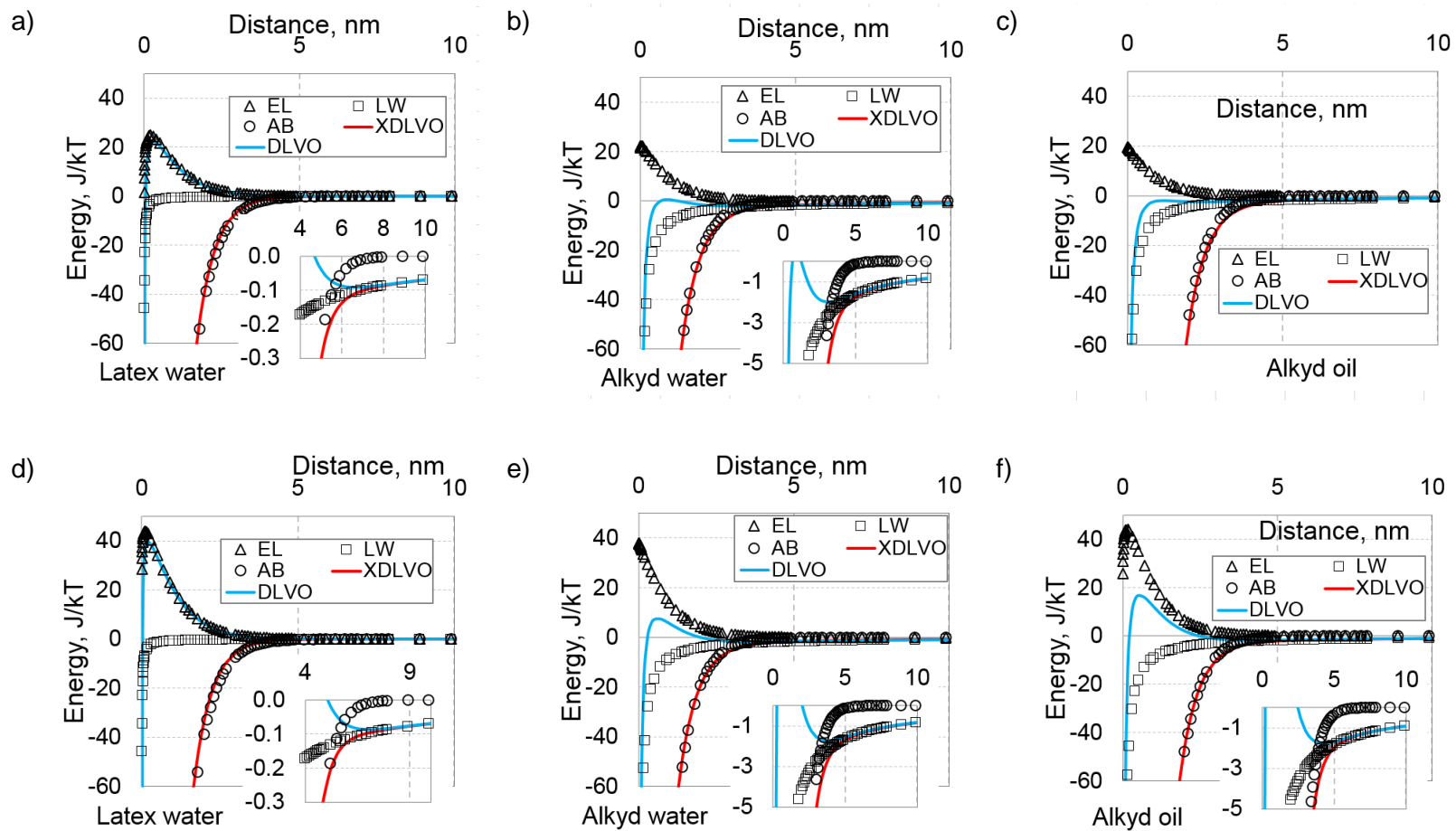


Figure 6: Profiles of DLVO and XDLVO energy of interaction between HAdV40 and paint surfaces in 150 mM NaCl: pH 5.2 (a, b, c) and pH 7.2 (d, e, f)

In 150 mM NaCl and pH 5.2 (Figures 6a, b, c), DLVO energy profiles show overall attractive interactions for the oil-based paint but energy barriers and secondary minimum for latex ($\Phi_{max} = 22.8$ kT, $\Phi_{min2} = 0.09$ kT) and alkyd ($\Phi_{max} = 0.62$ kT, $\Phi_{min2} = 2.00$ kT) water-based paints. This indicates unfavorable virus adsorption for latex water-based paint, followed by alkyd water-based paint. The oil-based paint was predicted to be the most favorable for HAdV40 adsorption. However, XDLVO energy profiles show overall attractive virus interactions for all the paints. AB interactions appear to significantly change DLVO profiles. When compared with the experimental results, XDLVO theory is more accurate than DLVO in virus prediction. Therefore, AB interactions in this case overtake EL interactions to control virus adsorption.

In 150 mM NaCl and pH 7.2 (Figures 6d, e, f), DLVO energy profiles display energy barriers for all the paints ($\Phi_{max} > 7$ kT) and secondary minima ($\Phi_{min2} = \sim 0.1$ kT for latex and 1.7 kT for alkyd paints). DLVO profiles predict unfavorable virus adsorption for latex paint and possible deposition in secondary minima for alkyd paints. XDLVO profiles present overall attractive interactions, indicating favorable virus adsorption for all the paints. XDLVO theory again proves more successful in predicting virus adsorption. Therefore, AB interactions play an important role and thus suppress EL interactions to control virus adsorption in high ionic strength.

3.3.4.2. Bacteriophage MS2

At pH 3.5, the negatively charged MS2 is electrostatically attractive to alkyd oil-based paint and repulsive to the water-based paints (Figure 3). At pH 6.0, MS2 and all three paints are carrying negative charges so that the electrostatic interactions between MS2 and each paint are repulsive. MS2 attachment to the oil-based paint should also be facilitated by this paint's higher hydrophobicity (Table 2).

The calculated LW interaction is least attractive for latex water-based paint and most attractive for alkyd oil-based paint. The calculated AB interactions are repulsive for all the paints.

In 1 mM NaCl and pH 3.5, the DLVO energy profiles show overall virus attraction with the oil-based paint; deep primary minima and energy barriers ($\Phi_{max} = 4.9$ kT for latex and 2.3 for alkyd water-based paint) (Figure 7a, b, c). It is likely for virus to acquire enough kinetic energy to overcome these energy barriers to deposit in the primary minima. Therefore, DLVO profiles predict favorable virus adsorption for the oil-based paint and possible adsorption for the water-based paints. In contrary, the XDLVO energy profiles show high energy barriers ($\Phi_{max} > 161$ kT) for all the paints and a secondary minimum ($\Phi_{sec} = 9.7$ kT) for alkyd-oil-based paint. This indicates unfavorable adsorption to the water-based paints and possible adsorption in the secondary minimum to the oil-based paint. Comparing with DLVO energy profiles, XDLVO profiles are more consistent with the QCM-D

results. AB interactions significantly change DLVO energy profiles and suppress other interactions to control virus adsorption.

In 1 mM NaCl and pH 6 and, DLVO energy profiles show no secondary minima but high energy barrier ($\Phi_{max} > 16$ kT) for all the paints, indicating unfavorable adsorption. XDLVO profiles also display high energy barriers ($\Phi_{max} > 180$ kT), indicating no virus adsorption to all the paints. Both DLVO and XDLVO theories are consistent with the QCM-D results. Even though AB interactions significantly change the DLVO energy profiles in short distances, especially increasing the energy barriers, they do not control virus adsorption in this case.

In 100 mM NaCl and pH 3.5 (Figure 8a, b, c), DLVO energy profiles display overall attractive interactions for the alkyd paints but an energy barrier ($\Phi_{max} = 3.9$ kT) for the latex paint. It predicts favorable adsorption for the alkyd paints and possible adsorption in the primary minimum for the latex paint. In contrast, XDLVO profiles show high energy barriers ($\Phi_{max} > 130$ kT) and shallow secondary minima ($\Phi_{sec} < 1$ kT) for all the paints, predicting unfavorable adsorption. Comparing with the QCM-D results, XDLVO theory is more successful in prediction of virus adsorption. Therefore, AB interactions prove to control virus adsorption in this condition - high ionic strength.

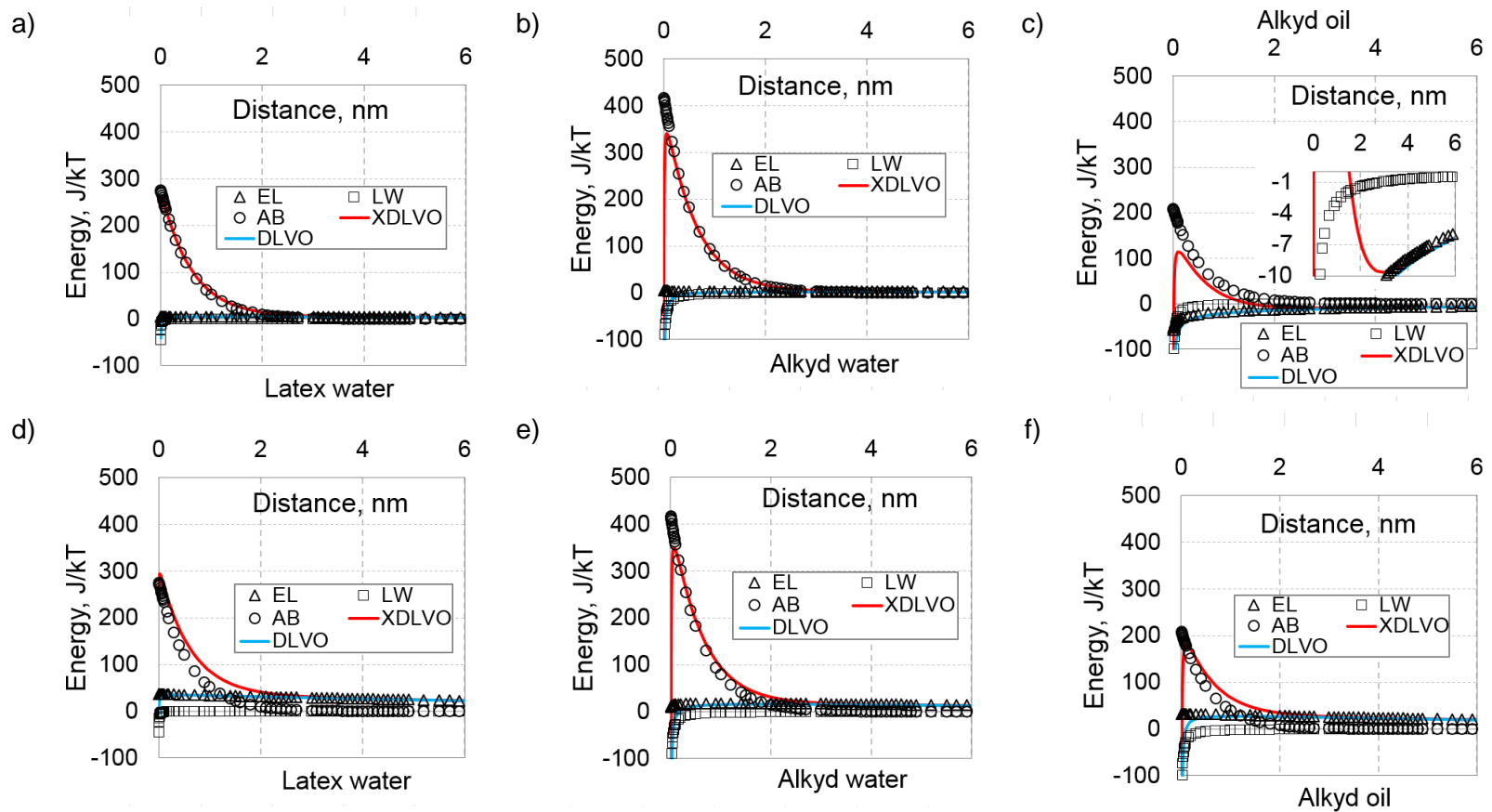


Figure 7: Profiles of DLVO and XDLVO energy of interaction between MS2 and paint surfaces in 1 mM NaCl: pH 3.5 (a, b, c) and pH 6.0 (d, e, f)

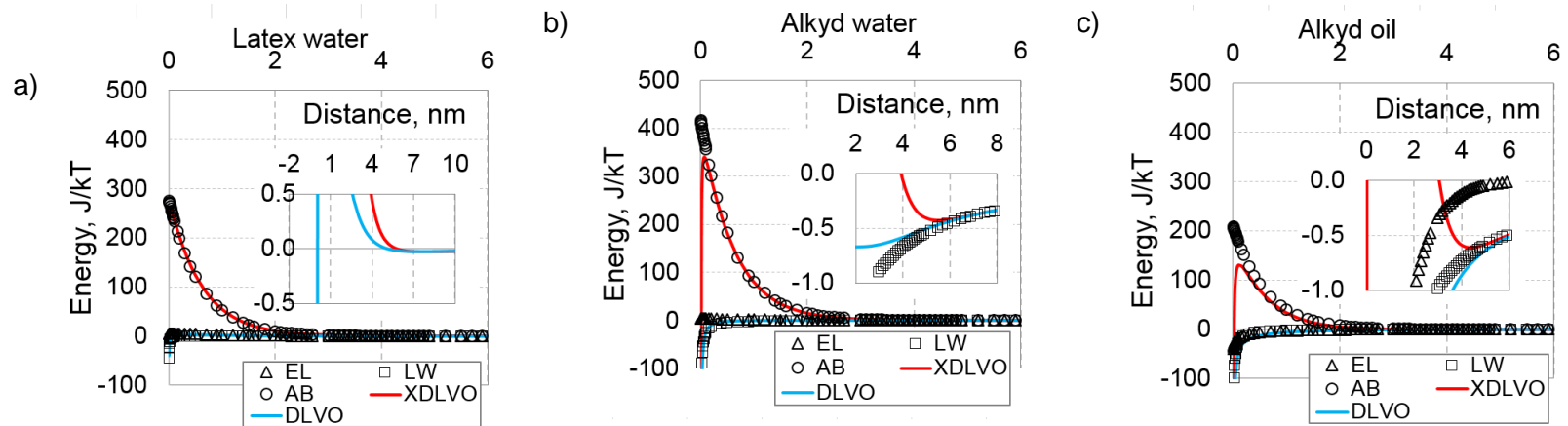


Figure 8: Profiles of DLVO and XDLVO energy of interaction between MS2 and paint surfaces in 100 mM NaCl and pH 3.5

3.3.5. Deposition of viruses on paint-coated surfaces

3.3.5.1. Deposition of HAdV40

Figure 9 shows the deposition kinetics of HAdV40 to the paint-coated surfaces from 1 mM and 150 mM NaCl background solution at different pH values. The kinetics undergo two distinctively different phases: a rapid growth in virus adsorption in a short period of time (< 10 min) (phase 1) and a slow increase in virus adsorption (phase 2). The phase 1 adsorption is caused by virus-paint interactions; while the phase 2 by interactions between virus and virus-coated surfaces. The following trends of deposition kinetics are observed:

1. The phase 1 adsorption kinetics was fastest for alkyd oil-based paint ($(\frac{dm}{dt})_1 = \sim 85.2$ in at pH 3.5 and ~ 69.7 at pH 6.0), followed by latex water-based paint and the alkyd water-based paint had the slowest kinetics of adsorption in 1 mM NaCl, regardless of electrostatic repulsion (Figure 9a and b). This is consistent with the paints' order of hydrophobicity: alkyd oil-based paint ($\Delta G_{sls} = -37.9$ mJ/m²) is the most hydrophobic, followed by the latex water-based paint ($\Delta G_{sls} = -22.1$ mJ/m²) and the alkyd water-based paint is the least hydrophobic ($\Delta G_{sls} = -1.6$ mJ/m²). Therefore, AB interactions may control virus adsorption in this case.
2. The kinetics of HAdV40 adsorption is identical for the oil-based paints; while it was slower in phase 1 but more progressive in phase 2 for the water-based paints in 1 mM NaCl (Figure 9a and b). This is expected for

- the oil-based paint due to similar EL and AB interactions in both pH 3.5 and 6.0. As for the water-based paints, EL interactions become more repulsive at pH 6.0, resulting in slower adsorption in phase 1; more binding area available after phase 1 could be the reason for higher virus adsorption in phase 2.
3. The phase 1 adsorption kinetics for the oil-based paint was faster but lasts shorter than those of the water-based paints in 1 mM NaCl (Figure 9a and b). The short-distance AB interactions may be responsible for fast adsorption but soon be weakened.
 4. The phase 1 adsorption kinetics for the water-based paints at pH 5.2 and 7.2 (Figure 9c and d) is slower than those in at pH 3.5 (Figure 9a) but faster than those at pH 6.0 (Figure 9b). This is expected for the water-based paints to have higher adsorption caused by the attractive EL interactions at pH 3.5 and by increasingly suppressed EL repulsion in high ionic strength at pH 5.2 and 7.2. This trend was not observed for the oil-based paint; namely its adsorption kinetics is lower in higher ionic strength (Figure 9c and d). The QCM-D data showed that the oil-based paint became rigid in 1 mM NaCl but more viscoelastic in 150 mM NaCl. Restructure of surface morphology may contribute to its virus adsorption.
 5. The phase 2 adsorption kinetics in high ionic strength (Figure 9c and d) is more progressing than those in low ionic strength (Figure 9a and b). At

higher ionic strength the electrostatic repulsion between virus and virus-coated surfaces is screened out, resulting in higher virus adsorption. In addition, this behavior also may be facilitated by virus aggregation at the higher ionic strength [33, 34].

6. Adsorption kinetics in high ionic strength at pH 7.2 (Figure 9d) is more identical for all the paints; while that is more progressing for the water-based paint than for the oil-based paint at pH 5.2 (Figure 9c). This could be explained that the surfaces are more negative at higher pH value, resulting in thicker screening layer of Na^+ . In this case, the electrostatic repulsion maybe suppressed leading to equal virus deposition on the paints. At pH 5.2 and 150 mM NaCl, a thin layer of screening Na^+ does not significantly block the electrostatic interaction, resulting in a similar deposition behavior observed in 1 mM NaCl.
7. The dissipations increased during virus deposition for the water-based paints (see Appendix A, Figure A6), indicating that the HAdV40 later exhibits viscoelastic behavior that is sustained with the growth of the deposit. However, the dissipation for the oil-based paint decreased in 1 mM NaCl (see Appendix A, Figure A6a and b) but increased in 150 mM NaCl (see Appendix A, Figure A6c and d)). This indicates that HAdV40 deposit on this surface is getting more viscoelastic in high ionic strength but more rigid in low ionic strength as more HAdV40 accumulates on the

surface in; such behavior may be caused by restructuring and consolidation of the virus deposit.

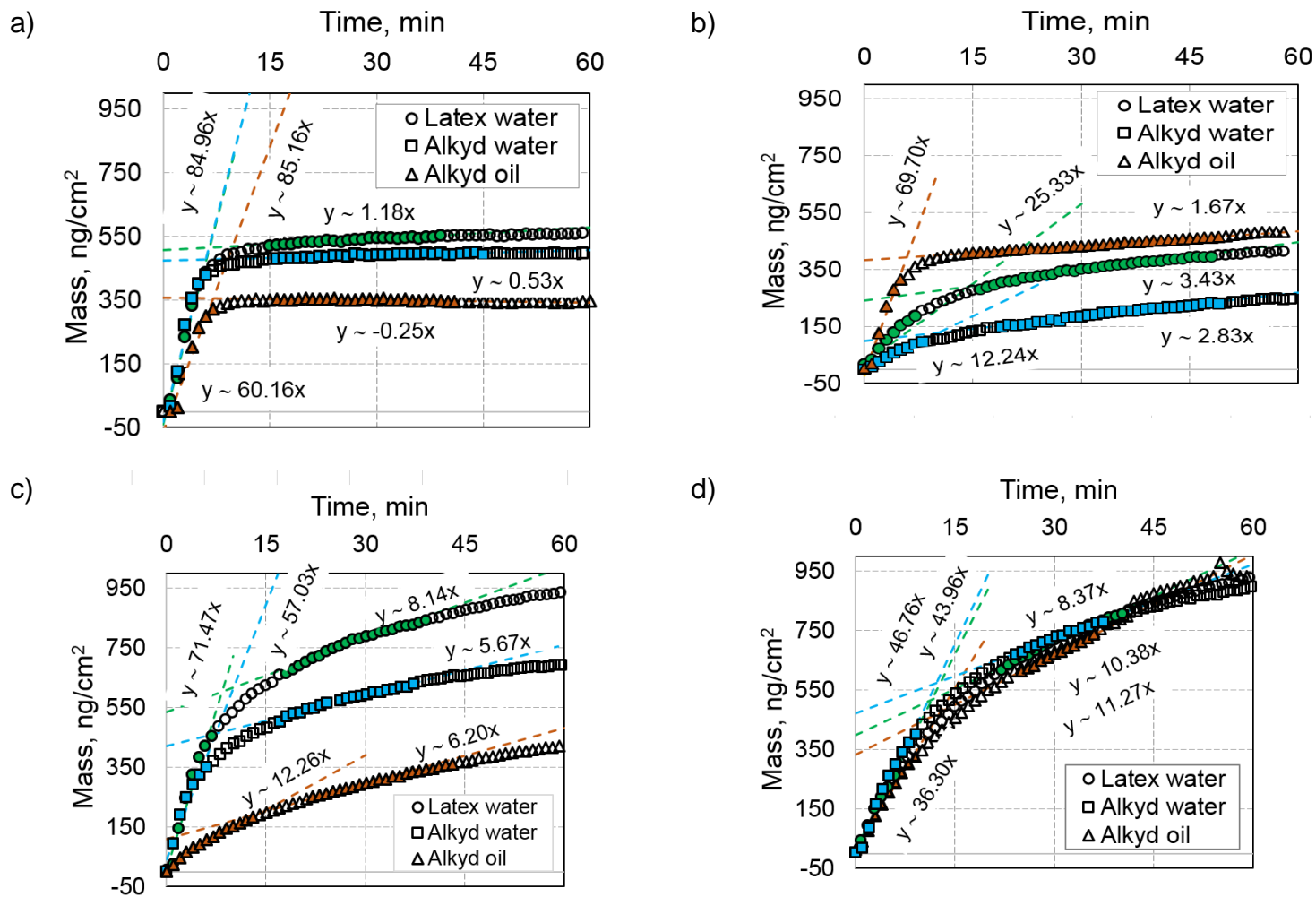


Figure 9: Kinetics of HAdV40 deposition onto the paint surface: 1 mM NaCl at pH 3.5 (a) and pH 6.0 (b) and 150 mM NaCl at pH 5.2 (c) and pH 7.2 (d)

3.3.5.2. Deposition of MS2

Figure 10 shows the adsorption kinetics of MS2 on the painted surfaces during 1 h in 1 mM and 100 mM NaCl at different pH values (pH 3.5 and 6.0). Unlike the kinetics of HAdV40 adsorption, the two phases do not appear clearly for MS2 adsorption kinetics. The followings are observations of MS2 adsorption kinetics to the paint-coated surfaces.

1. There were no statistically significant differences between the deposited mass recorded for different paints at the same pH and ionic strength. All the paints were observed repulsive to MS2 adsorption, regardless of EL and AB interactions. The XDLVO theory show high energy barriers and shallow secondary minima ($\Phi_{sec} < 1 \text{ kT}$) - except for the oil-based paint ($\Phi_{sec} = \sim 9.7 \text{ kT}$) at pH 3.5 and in 1 mM NaCl (Figure 7) - indicating unfavorable virus adsorption. Therefore, AB repulsion may suppress EL interactions to control MS2 adsorption to surfaces in this case.
2. MS2 deposited more favorably to surfaces at lower pH value and in higher ionic strength. An improved MS2 deposition at pH 3.5 may be due to the contribution of aggregation. Some studies show that at lower pH ($\text{pH} \leq 4$) MS2 tends to aggregate [97, 98]. In this case, the results provided by QCM-D may results from both adsorption and aggregate processes. For the water-based paints that are negative at pH 3.5, the surfaces become less negative in higher ionic strength because of the electrostatic

screening by the salt, leading to a higher MS2 deposition. However, for alkyd oil-based paint that is positive at pH 3.5, even though the electrostatic attraction was screened in higher ionic strength, the hydrophobic interaction between the surface and virus may remain significant due to a larger particle size. This increased hydrophobic interaction might suppress the decreased electrostatic attraction, resulting in more MS2 deposition in 100 mM NaCl.

3. HAdV40 deposited much more favorably to the painted surfaces (Figure 9) than MS2 did under the same conditions (Figure 10). This probably be attributed by the AB interactions between virus and surfaces; namely AB interactions are attractive for HAdV40 but repulsive for MS2. In addition, HAdV40's larger size and the presence fibers of its surface also may contribute to its favorable attachment; while MS2's hydrophilic loops may hinder its adsorption. This interpretation was observed in other studies, which showed that larger size and surface fibers promote virus adsorption [13, 33, 34].

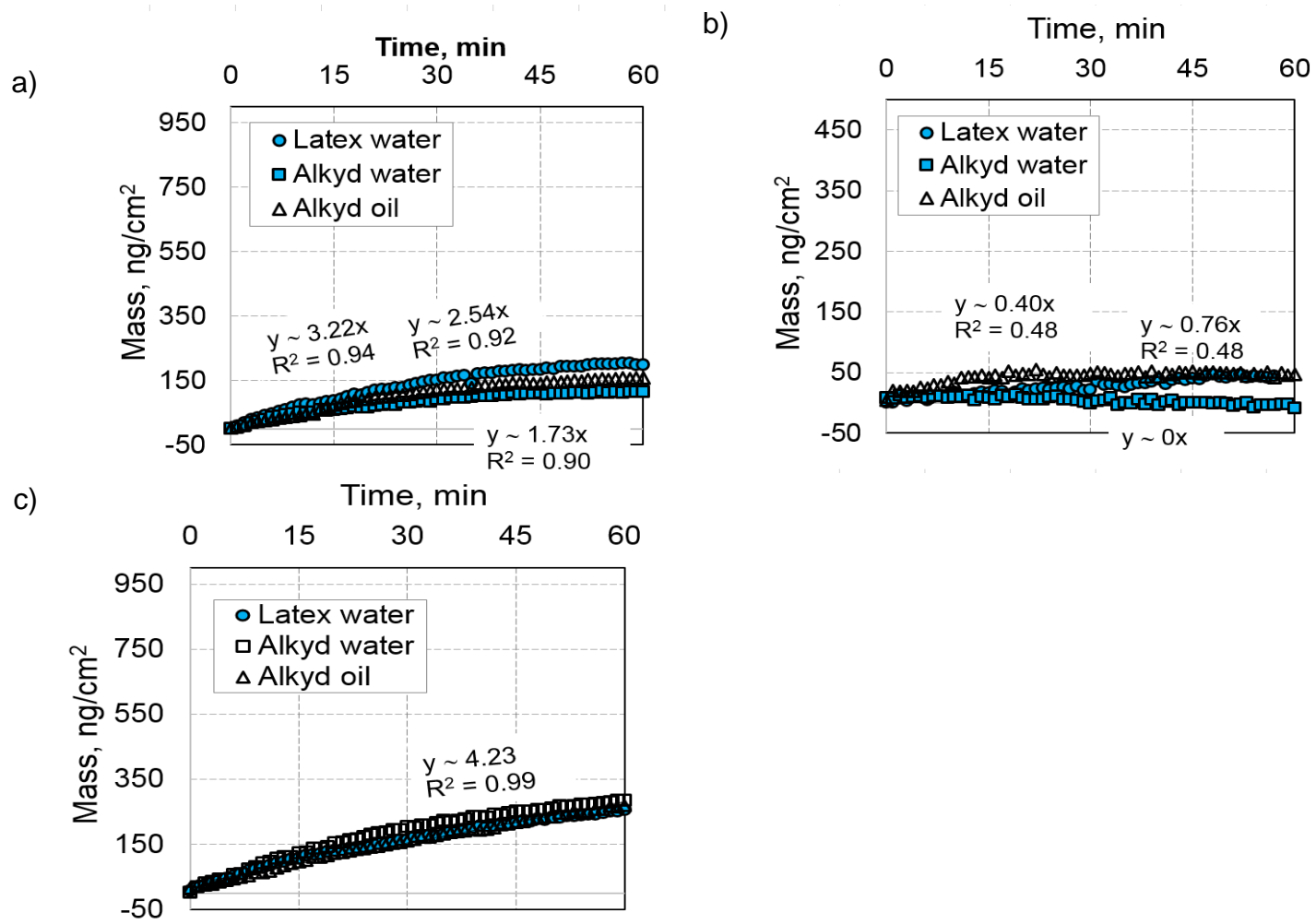


Figure 10: Kinetics of MS2 deposition onto the paint surfaces in 1 mM NaCl: pH 3.5 (a) and pH 6.0 (b) and in 100 mM NaCl at pH 3.5 (c)

3.3.6. Principal component analysis

The PCA data matrix included the following active variables: deposition rates during phases 1 and 2 ($(dm/dt)_1$ and $(dm/dt)_2$), zeta potential of the painted surfaces (ζ), and the free energy of interfacial interaction (ΔG_{iwi}) of the paints. Two XDLVO energy profile metrics – the height of the energy barrier and the depth of the secondary minimum during deposition phase 1 (Φ_{max} and Φ_{Sec}) were used as supplementary variables.

In Figure 11, we use the following notation to describe different virus deposition scenarios: **a-X-Y-b**. In this notation, **a** is the ionic strength (mM) of the virus deposition solution, **X** is the virus (MS2 and HAdV40), **Y** is the paint used for virus deposition (LW = latex water-based paint; AW = alkyd water-based paint; AO = alkyd oil-based paint) and **b** is the pH of the deposition solution. For example, 1-MS2-LW-3.5 denotes an experiment where MS2 bacteriophage was deposited to the latex water-based paint from 1 mM NaCl electrolyte with pH 3.5. As another example, 150-HAdV-AW-7.2 denotes an experiment where HAdV40 was deposited to the alkyd water-based paint in 150 mM NaCl and pH 7.2.

Figure 11 show factor loadings (a) and factor scores (b) of different virus deposition experiments. The principal components F1 and F2 capture more than 61% of the variance. The factor loadings (Figure 11a) is used to study the importance of variables to the principal components and their correlation to each

other; while the factor scores (Figure 11b) provides information about classification of datasets.

The factor loadings (Figure 11a) present the following information:

1. The vertical principal component (F2) is linked to paint' hydrophobicity (measured in terms of ΔG_{iwi}) while the horizontal principal component (F1) is linked to paint's electrical charge (ζ_{paint}).
2. The deposition rate in phase 1 $(dm/dt)_1$ is independent of paint hydrophilicity .

The following observations can be made based on the factor scores (Figure 11b):

1. The principal component (F1) separates the two viruses: HAdV40 with low Φ_{max} and high $(dm/dt)_1$ from MS2 with high Φ_{max} and low $(dm/dt)_1$.
2. The principal component (F2) separates the most hydrophobic ($\Delta G_{iwi} = -38.0$ mJ/m²) oil-based paint from the least hydrophobic acrylic water-based paint ($\Delta G_{iwi} = -2.7$ mJ/m²). The latex water-based paint of intermediate hydrophobicity ($\Delta G_{iwi} = -22.1$ mJ/m²) corresponds to F2 values near zero.

3. The factor scores plot classifies the data points in clusters with different viruses and paints.
- a. Data points with alkyd water-based paint are in the upper positive domain (in green shades). Those with latex water-based paint are in the lower positive domain (in violet shades). Those with alkyd oil-based paint are in the negative domain (yellow shades)
 - b. The principal component F2 correlates to the magnitude of Φ_{max} for MS2-paint interactions. For examples, the green shade corresponds to the highest Φ_{max} , followed by the pink shade. The yellow shade has the lowest Φ_{max} .
 - c. 1-MS2-AO-6.0 is located far away from the other two data points with MS2 because ζ_{paint} at pH 6.0 is negative (-40 mV); while it is positive at pH 3.5 (18 mV) for the other two data points.
 - d. Two data point (1-HAdV-AO-3.5) is located in the positive domain for MS2 due to the positive charge of the paint (-40 mV) at pH 3.5.

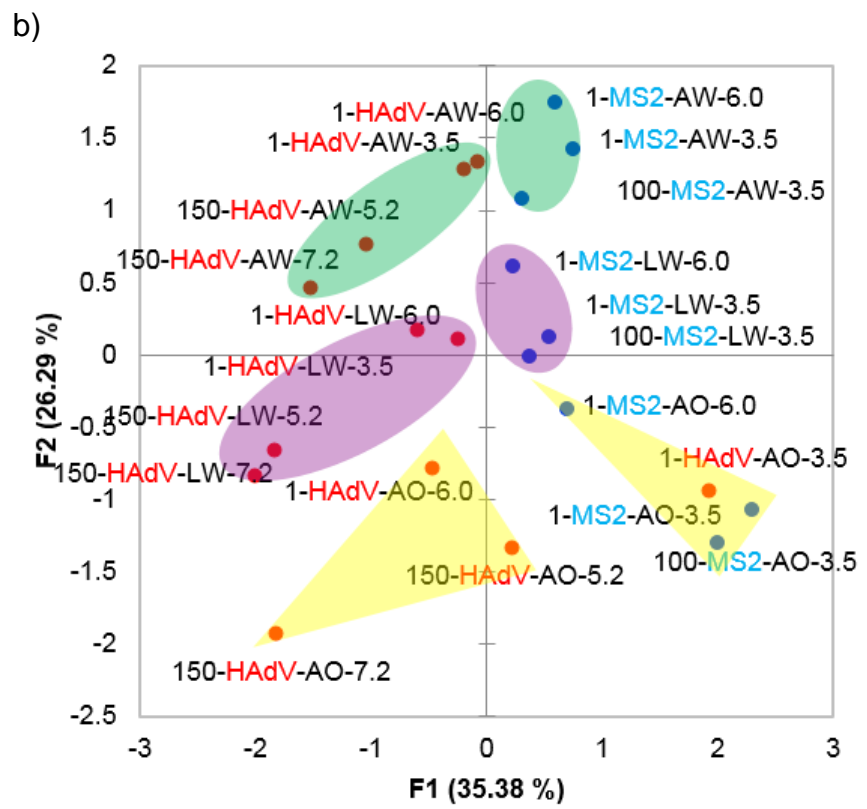
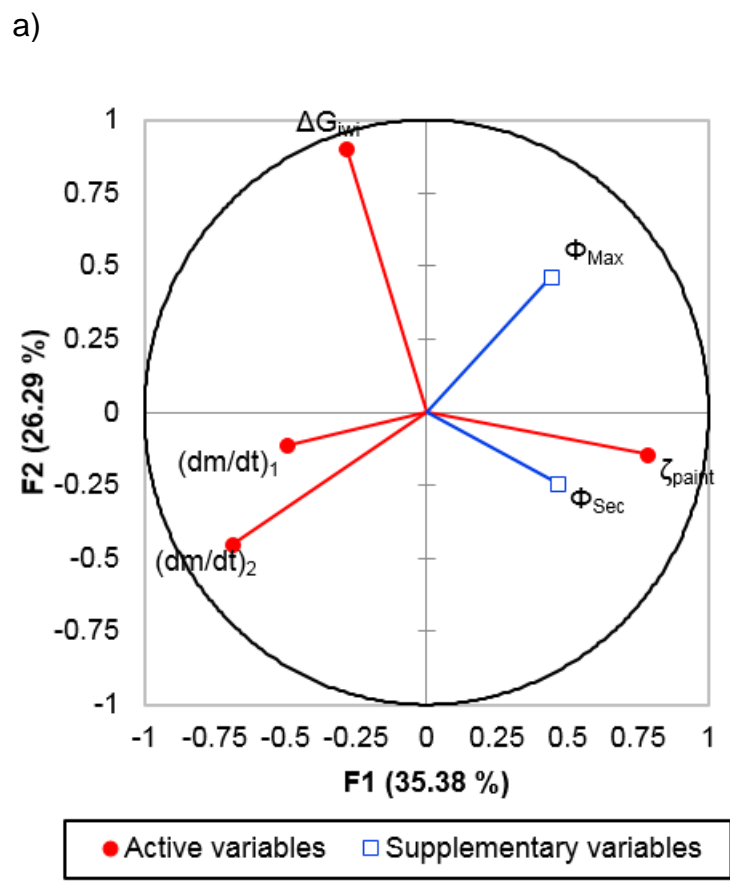


Figure 11: Principal component analysis (PCA): factor loadings (a) and factor scores (b)

3.4. Conclusions

Attachment of bacteriophage MS2 and human adenovirus 40 onto negatively and positively charged paint-coated surfaces were studied using quartz crystal microbalance with dissipation monitoring.

1. The DLVO and XDLVO theories were used to predict virus adsorption. Comparing with the DLVO theory, the XDLVO predictions are more consistent with the QCM-D results and thus more successful in explaining of virus adsorption, especially in high ionic strength and more evidently for MS2 than for HAdV40.
2. Both the experimental results and modeling methods pointed to a more favorable adsorption for HAdV40 than for MS2. This is attributed to more attractive AB interactions and, tentatively, to adsorption facilitated by fibers of HAdV40.
3. The kinetics of HAdV40 adsorption undergo 2 distinctive phases; the separation between two phase was less clear for MS2 adsorption.

The viscoelastic behavior of the deposited layer depended on the types of the virus and surface: the layers formed on the water-based paints became more viscoelastic with deposited HAdV40 while the opposite trend was observed for the oil-based paint. This trend was not clearly observed for MS2 deposition

because of low mass gain. The approach demonstrated in this study can guide the design of surfaces that resist virus adhesion. Paints formulated should help reduce human exposure to viruses.

CHAPTER 4: DEPOSITION OF BACTERIOPHAGE MS2 ONTO POLYELECTROLYTE-COATED SURFACES

Abstract

Deposition of bacteriophage MS2 onto polyelectrolyte-coated surfaces was studied using a combination of experimental studies and modeling. Quartz crystal microbalance with dissipation (QCM-D) measurements were performed with MS solutions of different ionic strengths ($I_{MS2} = 10$ or 100 mM NaCl) and surfaces of different charges and hydrophobicities. The experimental results were compared with the predictions by the Derjaguin-Landau-Verwey-Overbeek (DLVO) and extended DLVO (XDLVO) theories. Each surface coating was designed by assembling a polyelectrolyte multilayer via layer-by-layer deposition of poly(styrene-4-sulfonate) (PSS) and poly(dimethyl diallyl ammonium chloride) (PDAD) on a QCM-D sensor from solutions of either high or low ionic strength ($I_{LbL} = 100$ mM or 10 mM NaCl) yielding the total of four different surfaces. The increase in I_{MS2} led to an increase of the deposited mass on the negative surface and a decrease of the deposited mass on the positive surface, pointing to the importance of electrostatic interactions between the virus and the surface. Short range hydrophilic repulsion prevented deposition into the primary minimum. We conclude that MS2 adsorption was governed by electrostatic and hydrophobic interactions while van der Waals interactions played a relatively minor role. The results point to the potential use of easily coated polyelectrolyte

multilayers for regulating virus adsorption. Specialty coatings can be created to control virus adhesion to surface and reduce human exposure to viruses.

Keywords: polyelectrolyte multilayers, layer-by-layer deposition, bacteriophage MS2, XDLVO

4.1. Introduction

Deposition of virus to surfaces play an important role in determining the likelihood of human exposure to viral pathogens. Of especial concern are noroviruses (NoVs) recognized as the leading agent of gastroenteritis in humans, accounting for more than 90% viral gastroenteritis and ~ 50% all the outbreaks of gastroenteritis worldwide [99]. Non-enveloped, single-stranded RNA viruses with the diameter in the 27 to 32 nm range, NoVs were estimated to cause ~900,000 gastroenteritis cases and ~64,000 hospitalizations in children younger than 5 years old in developed countries, up to 1.1 million hospitalizations and 218,000 deaths in children in developing countries every year [100].

Studies on virus fate and transport often employ bacteriophages as surrogates for human viruses. Provided physicochemical characteristics such as size, morphology, charge, and hydrophilicity match that of the target human virus, bacteriophages are close-to-ideal model microorganisms that are convenient and safe to work with. A suitable surrogate for NoVs have is the MS2 phage that several key similarities with NoVs: the ability to persist in the intestinal tract, positive sense RNA genome, single-stranded RNA, resistance to various disinfection treatments and same size range [101]. A member of the *Leviviridae* family, MS2 infects *E. coli* cells, has an icosahedral capsid and comprises 180 sequence-identical protein monomers. MS2 is ~ 27 nm in diameter and has ~ 1 nm loops of hydrophilic amino acids extruding from the capsid. Some studies [9, 35] suggested that these loops cause steric forces to hinder virus adsorption.

The surface charge of MS2 is believed to stem from the ionizable amino acids located on the outer capsid surface [10]. The isoelectric point (IEP) of these amino acids was calculated to be 3.9, which falls within the range of IEP values (3.5 to 4) measured for this bacteriophage [10, 32, 95]. MS2 was reported to aggregate around its IEP and at $\text{pH} \leq 4.5$ in 1 mM and 100 mM NaNO_3 [95, 102] and at $\text{pH} \leq 4$ in 10 mM NaCl [10]; pH was found to be a more important factor than ionic strength in controlling aggregation [95].

Numerous studies have been conducted on MS2 adsorption to different surfaces such as soils [32-34, 103], natural organic matter [9, 10, 104] and membrane filters [11, 12, 76, 105]. Virus properties such as surface charge [11, 12], hydrophobicity [10, 32, 33], size and shape [10, 33, 34] were reported to affect virus adsorption. The hydrophilic loops of MS2 are believed to induce steric forces that hinder adsorption [9, 10, 35]. Identifying dominant interactions that govern virus adsorption is a key to understanding its fate and transport. Environmental conditions such as solution ionic strength and pH also impact virus adsorption [10].

Elucidating the relative importance of different interactions between a virus and a surface is instrumental for understanding virus fate and transport. The DLVO [9, 103, 104] and, more recently XDLVO theories [32, 105-107] have been broadly applied to describe virus-surface interactions. DLVO could explain experimental results in some (e.g. [103]) but not all (e.g. [9, 10, 104]) studies. In consistence with DLVO, Tong et al. [103] reported an increase of MS2 deposition on

bentonite and kaolinite when the salt concentration in the virus suspension increased. For example, in a study on deposition kinetics of MS2 to coated surfaces [9] DLVO energy profiles exhibited no energy barrier in ionic strengths > 60 mM while the attachment efficiencies were low (~ 0.2). The extended DLVO (XDLVO) accounts for hydrophobic interactions. These forces were shown to make a significant contribution to the overall energy of interaction between phages (MS2, Φ X174) and clay surfaces [32]. Chattopadhyay et al. concluded that hydrophobic interactions controlled adsorption of T2, MS2 and Φ X174 phages to clays [33].

Virus deposition onto a surface can be quantified using quartz crystal microbalance (QCM) as long as the QCM sensor can be coated by a material that adequately represents the surface in question. By detecting shifts in QCM sensor's frequency, this technique can measure mass with nanogram sensitivity and, by measuring dissipation shifts, can offer insights into the viscoelastic behavior of the adsorbed layer [55]. QCM-D has been used to study the attachment of bacteriophages (MS2 [9, 10, 103], T4D [57]), norovirus virus-like particle (VLPs) [58, 59], adenovirus [60], air borne viruses [63] and pathogenic plant viruses [61, 62] to various surfaces such as bare QCM crystals [56, 59, 63], natural organic matter [9], polyelectrolyte multilayers [57, 60, 61], clays [9, 56], or self-assembled monolayers [58, 61, 62, 64]. Armanious et al. [10] attributed differences in adsorption behaviors of MS2, Φ GA and Q β bacteriophages that have similar sizes (28.6-29.4 nm outer diameter and 21.0-21.4 nm inner diameter) but different surface charges, hydrophobicity and morphologies. The consensus

appears to be that virus adsorption is mainly governed by electrostatic, hydrophobic [10] and steric [9] interactions while van der Waals interaction is of secondary importance [10].

Adsorption to polyelectrolytes surfaces is of interest due various applications of these materials as coatings for macroscopic and colloidal surfaces. Cationic polyelectrolytes such as polyacrylamide are used as flocculants in water treatment applications. Polyelectrolyte multilayers feature excellent ion separation properties and are used to make nanofiltration membranes [108]. The ability to easily remove polyelectrolytes from a surface make them promising as sacrificial layers for various applications from surface fouling control [109-111] to virus detection [112, 113]. In many of these applications, virus deposition on such surfaces occurs in a flow-through system, which motivated the use of QCM-D in exploring virus attachment to polyelectrolytes. In addition to their practical relevance, polyelectrolyte multilayers are excellent model surfaces where in changes in thickness [114-116], surface morphology [111], charge [110, 113], hydrophobicity [110, 111, 113] and the degree of swelling [114] can be easily controlled by adjusting deposition conditions such as the number of deposition cycles [114, 117], types of PEs [114], ionic strength [108, 116, 118], salt types [117] and solvent concentration [114, 116].

In this study, we employed quartz crystal microbalance with dissipation (QCM-D) to quantify MS2 deposition onto four different polyelectrolyte multilayer surfaces of different charges and hydrophobicities. The bacteriophage was deposited from

solutions of low and high ionic strength ($I_{MS2} = 10$ mM or 100 mM) to probe the relative importance of electrostatic interactions between MS2 and PEM surfaces. Predictions by DLVO and XDLVO theories were evaluated based on consistency with the QCM-D results. Principal component analysis was used to identify correlations and general trends in the dependence of deposition kinetics on virus and surface properties.

4.2. Materials and Methods

4.2.1 Reagents

All reagents were of high purity (>98%). Deionized water with a resistivity of 18.2 M Ω ·cm was used to prepare all solutions. Poly(diallyldimethyl ammonium chloride) (PDAD, MW ~ 70,000 Da) and poly(allylamine hydrochloride) (PSS, MW ~ 100,000 to 200,000 Da) were purchased from Aldrich.

4.2.2 Propagation, purification and quantification of bacteriophage MS2

4.2.2.1 MS2 propagation

The bacteriophage MS2 was purchased from American Type Culture Collection (ATCC). To propagate MS2, an actively growing broth culture was prepared by incubating few drops of overnight *E. coli* in soy broth for 6 h at 37 °C. The broth culture was then spiked with 0.1 mL of the diluted phage suspension (~10⁶ PFU/mL) and incubated overnight at 37 °C. The MS2 suspension was centrifuged at ~5000 rpm for 15 min to remove debris [76]. The supernatant was

filtered through a 0.22 µm filter (Millex-GS, Merck Millipore) and then stored at 4°C as a S2 stock for future use.

4.2.2.2 MS2 purification

To further purify MS2, polyethylene glycol 6000 (Sigma-Aldrich) and NaCl were added into the MS2 stock to a final concentration of 10 % and 0.5 M, respectively [76, 119]. The mixture was stirred gently overnight to settle down MS2 and then followed by centrifuging at 10,000 rpm for 30 min. After centrifugation, the supernatant was discarded and the pellets were suspended with 1 mM NaCl. Pellets were suspended by vibrating the sample on a shaker over 24 h. After the pellets were completely dissolved, the MS2 suspension was filtered through 0.22 µm filter and then dialyzed through 100 kDa dialysis tubes in 1 mM NaCl for 24 hours. The NaCl solution was exchanged after the first 12 h. The entire purification process was performed in dark at 4 °C.

4.2.2.3 MS2 quantification using double-layer plaque assay

MS2 concentration was measured using a double-agar layer assay. To quantify MS2, two agar media were prepared. The bottom layer contained 10 g tryptone, 1 g yeast extract, 8 g NaCl and 15 g agar, 1 g glucose, 0.294 g CaCl₂ and 10 mg thiamine in 1L of DI water. The top layer contained the same mixture of the components except for having 5 g (and not 15 g) of agar [120]. These media were boiled and cooled down to 50 °C. The bottom layer was then poured into 100 x 5 mm Petri dishes (15 ml in each), followed by drying in the biological

safety cabinet until the agar layer solidified. When it was still hot (~ 50 °C), the top layer agar was poured into every 20 mL culture tube at a volume of 2.5 mL and kept in a water bath at 43-45 °C. As for MS2 stock, it was serially diluted by pipetting 1 mL of the phage in 9 mL of broth until its final concentration was $\sim 10^3$ PFU/mL. After incubating the *E. coli* suspension for 6 h, one or two drops of the host stock was pipetted into every culture tube, followed by 100 μ m of diluted MS2 suspensions. The culture tube containing melted soft agar, *E. coli* and phage was gently mixed before pouring over a hard agar plate. After the top agar layer dried, the petri dish was placed upside down in the incubator for overnight until the lysis became visible. Every MS2 dilution was analyzed for MS concentration at least three times. The petri dishes with a number of countable lysis spots in the 50-300 range were chosen to determine MS2 concentration of MS2 stock.

4.2.3. Preparation and characterization of polyelectrolyte-coated surfaces

4.2.3.1 PEM deposition

PEMs were assembled on a gold crystal using QCM-D. Prior to the assembly, the crystal was cleaned following the cleaning procedure provided by the Biolin Scientific. It was first soaked in a 5:1:1 mixture of DI water, hydrogen peroxide (30%) and ammonia (25%) at 75 °C for 5 min. It was rinsed with DI water and then dried out with N₂, followed by 20 min ozone cleaning to remove hydrocarbon contaminants. The PE solutions were diluted to a repeat unit concentration of 0.02 M with the ionic strength (I_{LBL}) adjusted to 10 or 100 mM NaCl. The pH of

PSS and PDAD solutions was adjusted to 6.4 and 4.6, respectively, using 1 mM HCl and 1 mM NaOH solutions. After the crystals were cleaned, they were mounted within QCM-D modules. Resonance frequencies in air were established for each crystal, followed by a stable baseline for at least 5 min. This ensured that the crystals were completely clean. This step was also repeated in either 10 or 100 mM NaCl solution to establish a stable baseline in wet condition. To build up PEMs on a crystal, the PSS solution was first deposited for 5 min, followed by rinsing with NaCl solution to remove unbound PE chains. The PDAD solution was then deposited on top of the PSS layer, followed by 5 min NaCl rinsing. This cycle was repeated 4 or 4.5 times to create positive or negative PEMs. Every PE deposition and NaCl rinsing step lasted 5 min [121].

4.2.3.2 Measurements of the ζ -potential and hydrophobicity of PEMs

The zeta potentials of PEM surfaces were measured using an electrokinetic analyzer (EKA, Anton Paar) in 10 mM KCl. Due to the limitation of the instrument, surface charge of PEMs was only measured in 10 mM NaCl solution. Every measurement was repeated at least two times.

The PEM-coated surfaces were dried in room temperature overnight prior to the contact angle measurement. Contact angles of DI water, glycerol, and diiodomethane on the dried surfaces were then measured using a goniometer (model 250, Ramé-Hart). Contact angle values were calculated by DROPimage

Advanced software based on droplet shapes. PEM hydrophobicity was estimated based on free energy of cohesion in water, ΔG_{sws} (Table B1 in the Appendix B).

4.2.3.3 AFM characterization of PEM morphology

The surface roughness of PEM-coated surfaces was measured using AFM (Cypher) with the samples exposed to 10 mM NaCl or 100 mM NaCl solutions. The measured area for each sample was 2 μm x 2 μm . Statistical analysis of the recorded surface morphology rendered the followed data: average roughness, root-mean-square roughness and surface area difference.

4.2.4 QCM-D experiments

MS2 suspension used in the deposition tests was prepared by diluting the purified MS2 stock (see section 4.2.2.2) by either 10 mM or 100 mM NaCl solutions to a final concentration of $1.24 \pm 0.07 \cdot 10^{10}$ PFU/mL. The pH of the virus suspension was adjusted to 7. Zeta potential of MS2 was taken to be - 35 mV, which is the valued reported by Armanious et al. for MS2 at pH 7 [10]. Both PEM assembly onto the QCM-D sensor and MS2 deposition onto PEM-coated surface were carried out in situ within QCM-D modules at 25 $^{\circ}\text{C}$ and in a continuous flow mode at the flow rate of 0.15 mL/min using a digital peristaltic pump (IPC, 4 channels, ISMATEC). Values of frequency and dissipation were recorded every 1 min.

The frequency shifts acquired for a clean and PEM-coated sensor were fitted into the Sauerbrey equation [92] to determine the mass change, Δm , of PEMs on that QCM-D sensor: $\Delta m = -C\Delta f/n$, where C is the mass sensitivity constant ($C = -17.7 \text{ ng Hz}^{-1}\text{cm}^{-2}$), n is the overtone number ($n = 3$), and Δf is the frequency shift (Hz). The frequency shift (Δf) was obtained by subtracting the frequency of the clean sensor from the frequency of the PEM-coated sensor. The mass of MS2 deposited onto the PEM-coated sensor was calculated as the difference between the frequencies of the PEM-coated sensor before and after 1-hr of MS2 deposition.

4.2.5. Nomenclature

In what follows we use the following notation to describe different MS2 deposition scenarios: $X\text{-[PSS/PDAD]}_n\text{-}Y$. In this notation, X is the ionic strength (I_{LbL} , mM) of the NaCl solution from which the PEM was deposited and n is the total number of bilayers deposited while Y is the ionic strength (I_{MS2} , mM) of the MS2 suspension: For example, $100\text{-[PSS/PDAD]}_4\text{-}10$ denotes an experiment where MS2 bacteriophages deposit from 10 mM NaCl solution onto a 4-bilayer PDAD-terminated polyelectrolyte coating LbL-assembled from 100 mM NaCl solution.

4.3. Results and Discussion

4.3.1 Characteristics of polyelectrolyte multilayer coatings

The 10-[PSS/PDAD]₄ multilayer was hydrophobic ($\Delta G_{sls} = -16.3 \text{ mJ/m}^2$) and positively charged ($\zeta = 6.7 \text{ mV}$) (Table 4). Depositing the same sequence of polyelectrolytes from a solution with $I_{LbL} = 100 \text{ mM}$ led to a film (100-[PSS/PDAD]₄) that was slightly hydrophilic ($\Delta G_{sls} = 7.6 \text{ mJ/m}^2$) and had higher positive surface charge (27.5 mV). The 10-[PSS/PDAD]_{4.5} multilayer was highly hydrophilic ($\Delta G_{sls} = 45.2 \text{ mJ/m}^2$) and negatively charged ($\zeta = -5.7 \text{ mV}$).

Depositing the same sequence of polyelectrolytes from a solution with $I_{LbL} = 100 \text{ mM}$ led to a film (100-[PSS/PDAD]_{4.5}) that had higher negative charge (-17.8 mV) while the hydrophilicity remained statistically the same. For both [PSS/PDAD]₄ and [PSS/PDAD]_{4.5} films, their surface roughness was higher when they were deposited from the background solution of higher ionic strength ($I_{LbL} = 100 \text{ mM}$). The changes in roughness were due to the increased shielding, fewer cross-links between constituent polyelectrolytes leading to “loopier”, thicker, and rougher PEM films [117, 122].

Table 4: Zeta potentials, hydrophobicity, and morphological characteristics of [PSS/PDAD]₄ and [PSS/PDAD]_{4.5} surface coatings assembled from solutions of different background electrolyte concentrations (10 mM or 100 mM NaCl), rinsed, and exposed to either 10mM NaCl or 100 mM NaCl solutions.

* Root mean square roughness is the standard deviation of the average roughness.

** Surface area difference is the difference between the three-dimensional surface area over its two-dimensional projection or “footprint”.

Concentration of NaCl in the PEM LbL deposition solution, I_{LbL} (mM)	10		100	
Concentration of NaCl in the MS2 suspension, I_{MS2} (mM)	10	100	10	100
[PSS/PDAD]₄				
Zeta potential of the PEM, ζ (mV)	6.7 ± 2		27.5 ± 1	
Free energy of interfacial interaction, ΔG_{sws} (mJ/m ²)	-16.3 ± 2.1		6.9 ± 14.4	
Root-mean-square roughness of the PEM surface* (nm)	0.3	3.3	2.3	6.3
Surface area difference** (%)	0.04	0.5	0.5	3.3
[PSS/PDAD]_{4.5}				
Zeta potential of the PEM, ζ (mV)	-5.7 ± 2		-17.8 ± 0	
Free energy of interfacial interaction, ΔG_{sws} (mJ/m ²)	45.2 ± 0.6		44.3 ± 10.2	
Root-mean-square roughness of the PEM surface* (nm)	0.2	1.3	2.5	6.5
Surface area difference** (%)	0.03	0.07	0.08	0.9

4.3.2 XDLVO energy profiles for MS2-interactions with PEM surfaces

Figure 12 shows DLVO and XDLVO energy profiles for MS2 interaction with the positively charged 10-[PSS/PDAD]₄ and 100-[PSS/PDAD]₄ surfaces during phase 1 of the deposition process in the assumption that the surfaces are smooth. The calculated energy barrier (E_{max}) was high (> 69 kT) for all combinations of the surface type and the ionic strength of the solution (I_{MS2}) making it unlikely for MS2 to deposit in the primary minima. The secondary minima (E_{min}) in 10 mM solution were - 2.8 kT and - 9.6 kT for 10-[PSS/PDAD]₄ and 100-[PSS/PDAD]₄, respectively. Figure 13 shows DLVO and XDLVO energy profiles for MS2 interaction with the negatively charged 10-[PSS/PDAD]_{4.5} and 100-[PSS/PDAD]_{4.5} surfaces during phase 1 of the deposition process in the assumption that the surfaces are smooth. For all scenarios, E_{max} was very high (> 594 kT) and E_{min} low (< 0.7 kT) making irreversible deposition unlikely. XDLVO profiles were also calculated while taking surface roughness into account (see Appendix B, Figure B2). Roughness had only a very minor effect on the energy profiles and, specifically, on the values of E_{max} and E_{min} . XDLVO energy profiles for phase 2 (see Appendix B, Figure B4) were calculated using the same approach as for phase 1 except the electrical charge and surface energy parameters of the surface were assumed to be those of the MS2 phase.

4.3.3 QCM-D measurements of MS2 deposition onto polyelectrolyte-coated surfaces

In QCM-D tests, changes in both QCM frequency and dissipation were recorded. Frequency data translated into mass deposition rate, $m(t)$, are shown in Figure 14 and 15. Dissipation data, $D(t)$, and a summary of deposition kinetic parameters (deposition rate dm/dt and lag time t_1) can be found in the Appendix B (Figures B5 and B6, Table B2). Lag time is operationally defined as the time period between the start of the deposition test and the time mass deposition is detected by QCM

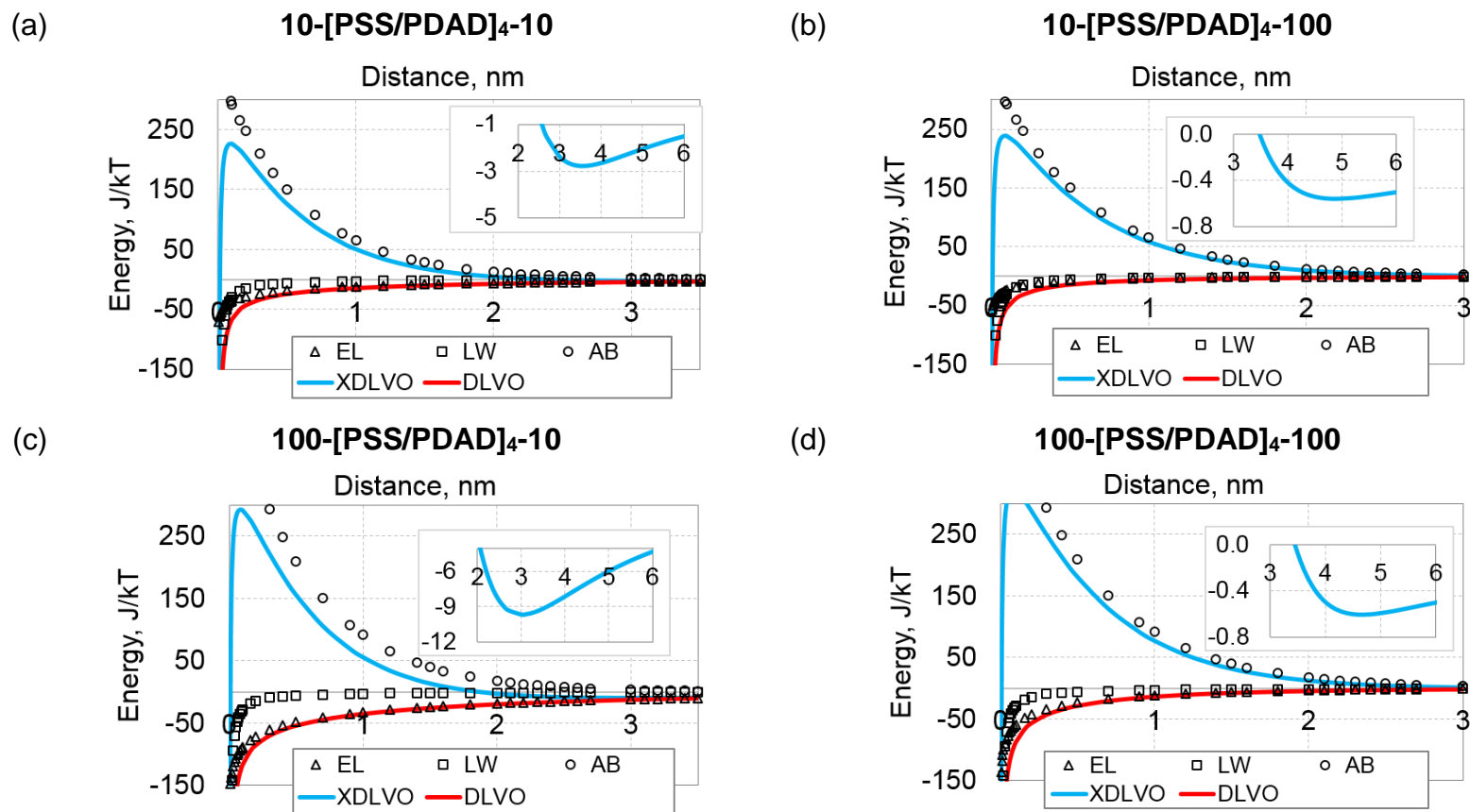


Figure 12: DLVO and XDLVO energy profiles of MS2 interaction with as-prepared (i.e. MS2-free) surfaces of 10-[PSS/PDAD]₄ (a, b) and 100-[PSS/PDAD]₄ (c, d) in 10 mM NaCl (a, c) and 100 mM NaCl (b, d) solutions. The profiles correspond to early stages of the phase 1 of MS2 deposition (see Figure 14).

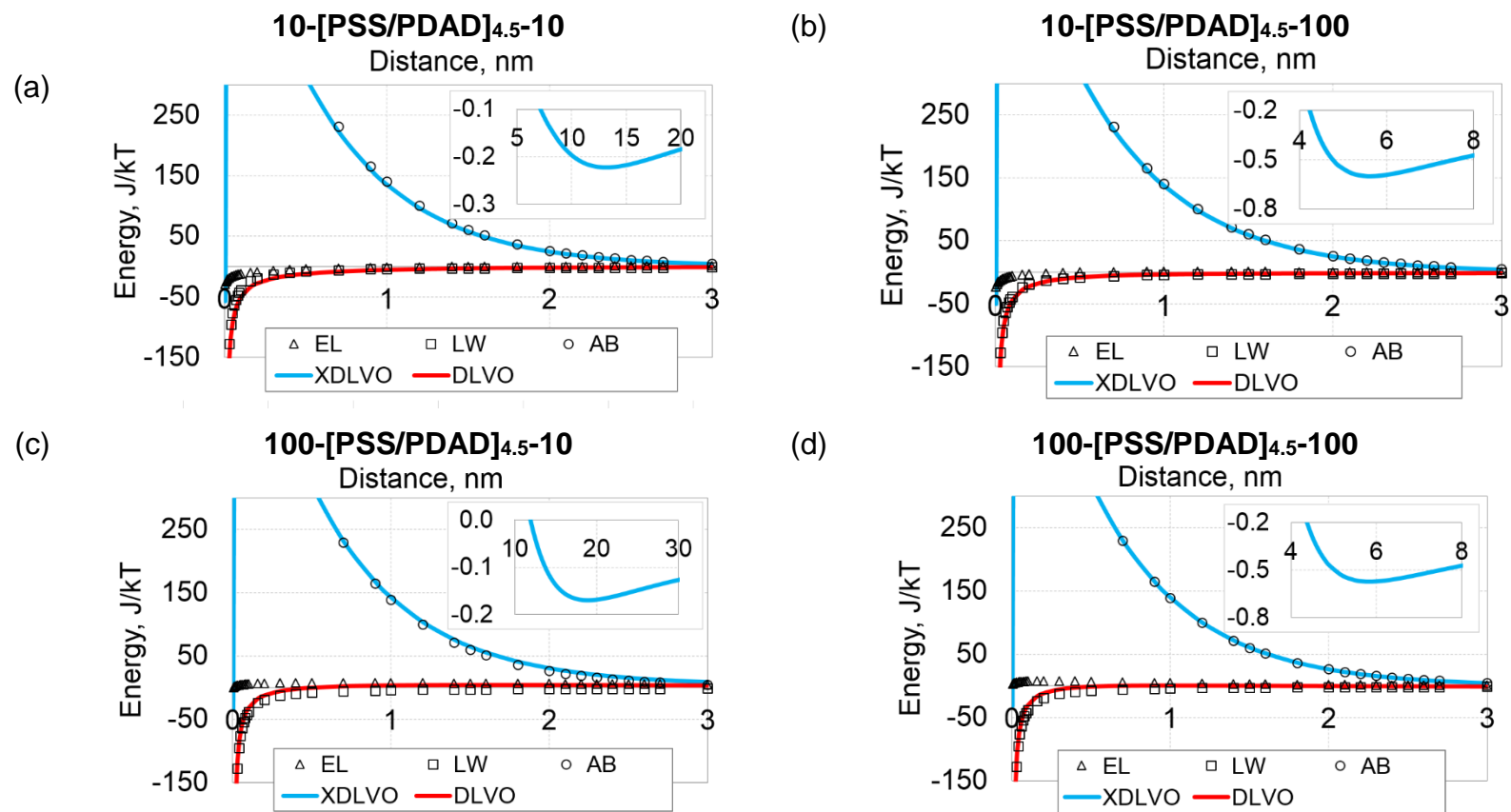


Figure 13: DLVO and XDLVO energy profiles of MS2 interaction with as-prepared (i.e. MS2-free) surfaces of 10-[PSS/PDAD]_{4.5} (a, b) and 100-[PSS/PDAD]_{4.5} (c, d) in 10 mM NaCl (a, c) and 100 mM NaCl (b, d) solutions. The profiles correspond to early stages of phase 1 of the MS2 deposition (see Figure 15).

4.3.3.1 Deposition of MS2 bacteriophage onto positively-charged PEM surfaces

Figure 14 illustrates the deposition kinetics of MS2 on the positively-charged surface of the 10-[PSS/PDAD]₄ and 100-[PSS/PDAD]₄ surfaces from solutions of different ionic strengths, I_{MS2} . In each of the four scenarios, deposition occurred in two distinct phases – an early stage with fast deposition kinetics (hereinafter, phase 1) and a stage where the deposition was much slower or is not observed at all (phase 2). The following specific trends could be identified:

1. The fastest phase 1 deposition kinetics was observed in 100-[PSS/PDAD]₄-10 experiments, where MS2-surface interactions (Figure 12c) are characterized by the secondary minimum in the total XDLVO energy (~ - 9.6 kT, Figure 12c and Table B2), the deepest XDLVO secondary minimum across all conditions considered in this study. The 100-[PSS/PDAD]₄ surface has the highest positive charge and the low ionic strength ($I_{MS2} = 10$ mM) offers less screening of electrostatic attraction between the virus and the surface. Comparison of with the 10-[PSS/PDAD]₄-10 scenario indicates that the modest difference in hydrophobicity between the two surfaces (6.7 mJ/cm² for 100-[PSS/PDAD]₄ vs -16.3 mJ/cm² for 10-[PSS/PDAD]₄) was less important than the weakly screened electrostatic attraction.
2. In tests with low ionic strength ($I_{MS2} = 10$ mM) no deposition was observed during phase 2. It appears that the deposition of the negatively charged

virus onto the PEM surface overcompensated the positive charge on 10-[PSS/PDAD]₄ and 100-[PSS/PDAD]₄ surfaces flipping electrostatic interactions between the virus and the surface to be repulsive. In consistence with this reasoning, at the higher ionic strength ($I_{MS2} = 100$ mM) the deposition on both 10-[PSS/PDAD]₄ and 100-[PSS/PDAD]₄ continued, albeit at a slower pace than during phase 1. Repulsive electrostatic interactions between the virus and the virus-coated surface are effectively screened in 100 mM NaCl electrolyte making a multilayer deposition possible.

3. Phase 1 deposition kinetics depended on ionic strength I_{MS2} for the highly charged 100-[PSS/PDAD]₄ but not for the weakly charged 10-[PSS/PDAD]₄. The trend is attributed to the screening of the attractive EL interactions, which were stronger for 100-[PSS/PDAD]₄.
4. Pair comparisons of 10-[PSS/PDAD]₄-10 vs 100-[PSS/PDAD]₄-10 and 10-[PSS/PDAD]₄-100 vs 100-[PSS/PDAD]₄-100 show that significantly more deposition occurred onto the 100-[PSS/PDAD]₄ than on 10-[PSS/PDAD]₄. The trend can be tentatively attributed to the higher roughness of the 100-[PSS/PDAD]₄ which translates into higher surface area and, therefore, stronger virus-surface interactions (attractive during phase 1). In general, the total deposited mass was determined by both the rate of deposition (highest in the 100-[PSS/PDAD]₄-10 scenario) and the adsorptive capacity of the surface (higher for 100-[PSS/PDAD]₄ surface).

5. The changes in dissipation (Figure B5 in the Appendix B) correlated with changes in the deposited mass indicating that the adsorbed layer was “soft” and exhibited a viscoelastic behavior.

6. Ionic strength (I_{MS2}) suppressed surface charge to determine total mass gain; in the other word phase 2 – virus-virus interactions- plays more important role in virus adsorption in long term.

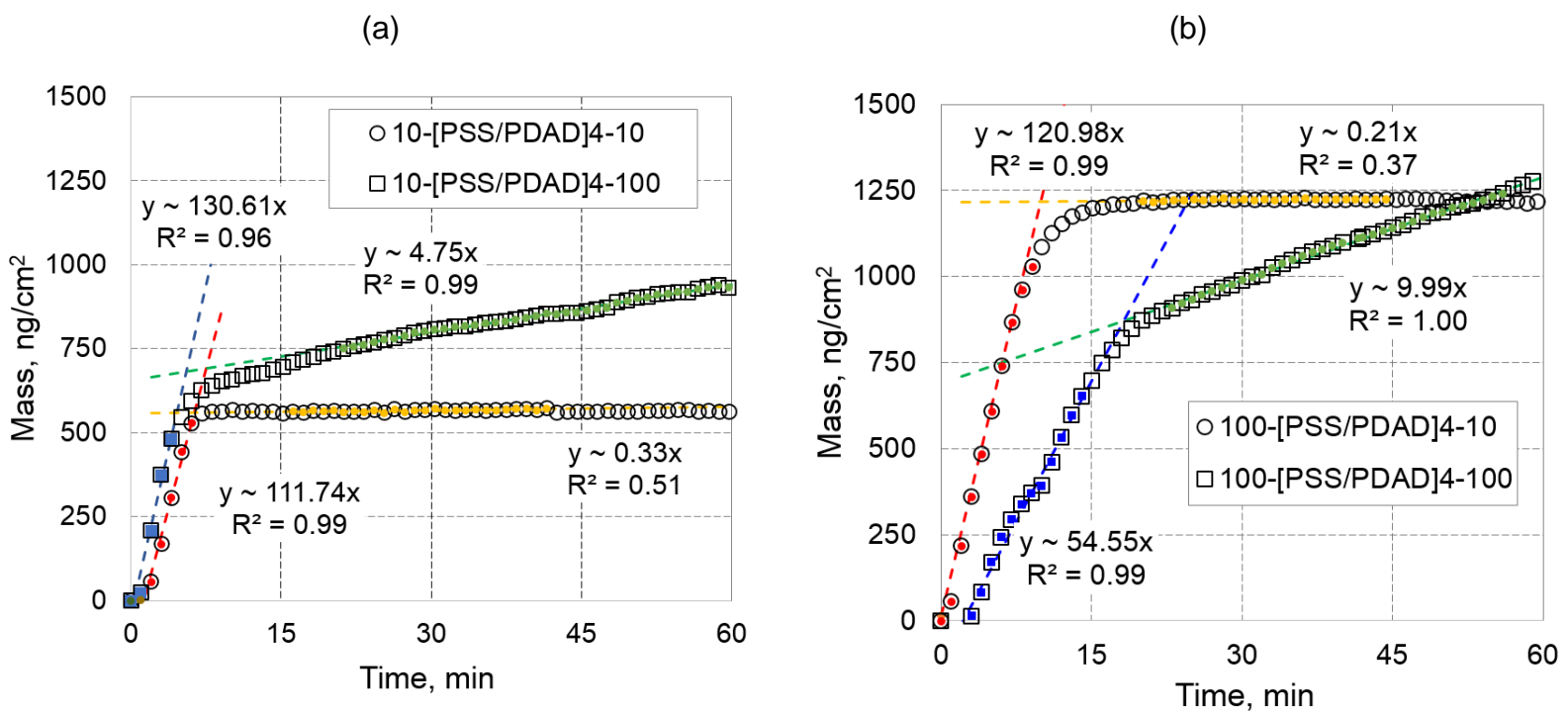


Figure 14: Kinetics of MS2 deposition onto (a) 10-[PSS/PDAD]₄, and (b) 100-[PSS/PDAD]₄ surfaces from solutions of different ionic strengths ($I_{MS2} = 10$ mM or 100 mM NaCl). Corresponding dissipation data are given in Appendix B (Figure B5)

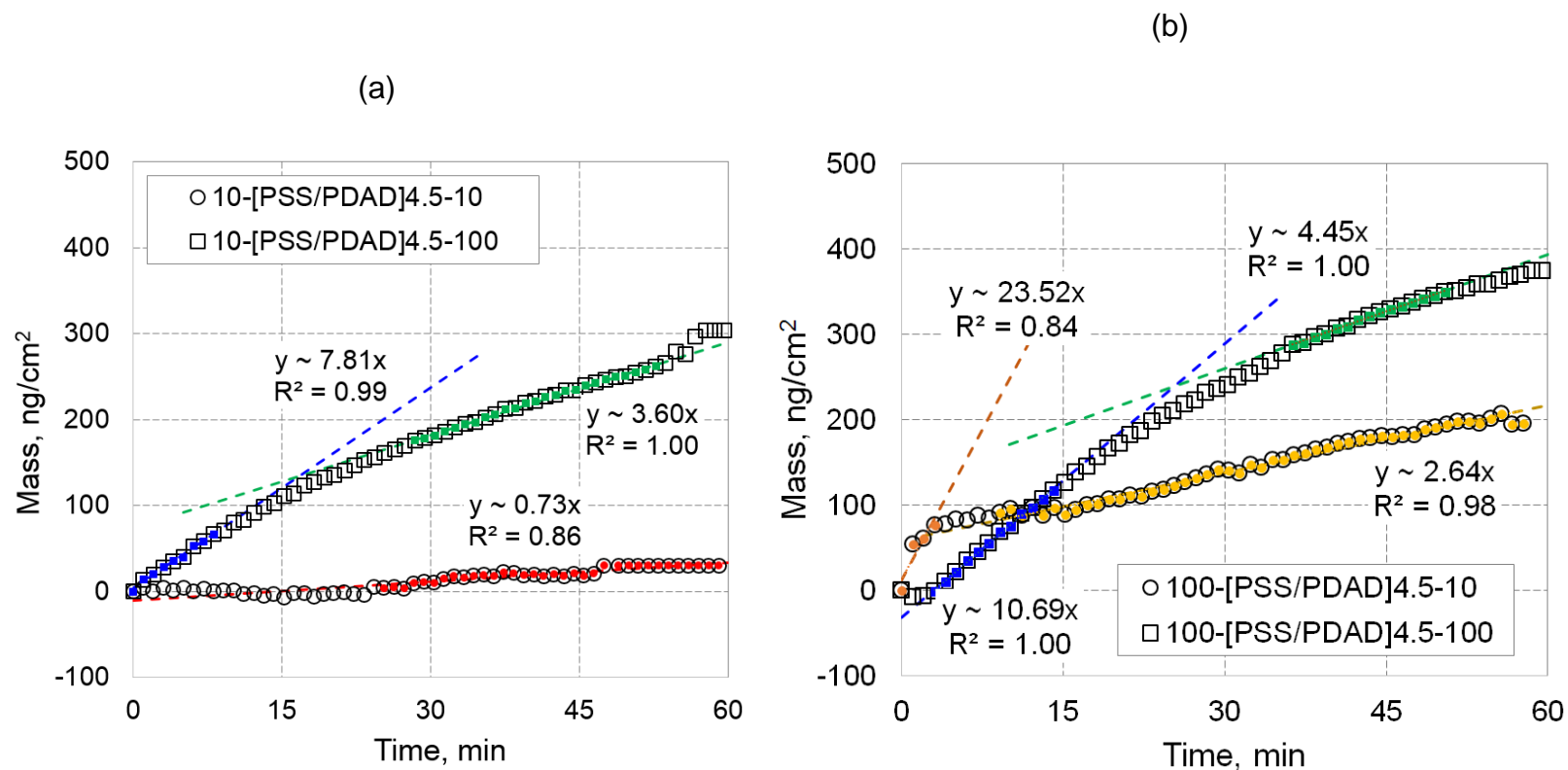


Figure 15: Kinetics of MS2 deposition onto (a) 10-[PSS/PDAD]_{4.5} and (b) 100-[PSS/PDAD]_{4.5} surfaces from solutions of different ionic strengths ($I_{MS2} = 10$ mM or 100 mM NaCl). Corresponding dissipation data are given in Appendix B (Figure B6).

4.3.3.2 Deposition of MS2 bacteriophage onto negatively-charged PEM surfaces

Figure 15 shows QCM-D frequency changes following 1 h of MS2 deposition onto the negatively-charged surface of 10-[PSS/PDAD]_{4.5} (Figure 15a) and 100-[PSS/PDAD]_{4.5} (Figure 15b) from solutions of 10 mM NaCl and 100 mM NaCl. Except for the 100-[PSS/PDAD]_{4.5}-10 scenario, the distinction between slow and fast phases of deposition was much less evident than for [PSS/PDAD]₄ surfaces. The following specific trends could be identified:

1. Deposition onto the negatively-charged surfaces was significantly (~ 3 to 5 times in terms of ng/cm²) weaker than on positively-charged ones as was expected based on the unfavorable electrostatic interactions and higher hydrophilicity of negatively charged for [PSS/PDAD]_{4.5} surfaces. This was consistent with XDLVO predictions of very shallow secondary minima (< 0.7 kT, Figure 13 and Table B2 in the Appendix B) for MS2-[PSS/PDAD]_{4.5} interactions. The difference was less pronounced in tests with MS2 deposition from 100 mM NaCl where the repulsive electrostatic interactions are screened more effectively.
2. The increase in adsorbed mass was monotonous in all cases except 100-[PSS/PDAD]_{4.5} and 10 mM background electrolyte when two deposition phases were observed.

3. Deposition from 10 mM NaCl onto 10-[PSS/PDAD]_{4.5} was negligible. Interestingly, this was not the case with the 100-[PSS/PDAD]_{4.5} surface, which could be due to differences in the surface morphology (Table 4 in the Appendix II).
4. Except for the 100-[PSS/PDAD]_{4.5}-10 scenario, the lag times were significantly higher (Table B2 in in the Appendix B) than for positively charged [PSS/PDAD]₄ surfaces.

4.3.3.3 Predictive ability of DLVO and XDLVO theories

AB interactions changed DLVO energy profiles to give rise to primary energy barriers and secondary minima. DLVO predicted overall attractive MS2 interactions with both 10-[PSS/PDA]₄ and 100-[PSS/PDA]₄ surfaces in both 10 and 100 mM NaCl solutions, which was consistent with QCM-D results. However, XDLVO predicted deeper secondary minima at low IS and for 100-[PSS/PDA]₄ pointing to more deposition in these cases. Overall, XDLVO proved to better predict how virus deposition depends on the ionic strength, I_{MS2} .

DLVO profiles also showed attractive interactions of MS2 with both 10-[PSS/PDA]_{4.5} and 100-[PSS/PDA]_{4.5} in both 10 and 100 mM NaCl solutions. This was not consistent with QCM-D results. In contrast, XDLVO profiles showed high energy barriers and shallow secondary minima, predicting unfavorable MS2-surface interactions. This is consistent with results of QCM-D tests wherein

almost no virus adsorption was observed in phase 1 (except for 100-[PEM]_{4.5-10}).

We conclude that XDLVO is better suited to describe virus-surface interactions attraction. AB interactions suppress EL interactions to control virus adsorption.

4.3.4. Principal component analysis

Principal component analysis was carried out on QCM-D experimental data (Figure 14 and Figure 15, Table B2 in the Appendix B) and XDLVO predictions (Figure 12 and 13, Table B2 in the Appendix B) to reveal correlations and trends that may not be obvious based on pair-wise comparisons of data subsets. The main objective was to discern correlations between PEM surface properties (ζ , ΔG_{sws}) and deposition conditions (I_{MS2}) on the one hand and MS2 deposition kinetics (dm/dt , t_1) on the other hand. The secondary objective was to assess the predictive ability of the DLVO model applied to MS2 deposition to PEMs. The analysis was performed using XLSTAT 2018 statistical software.

The PCA data matrix included the following active variables: deposition rates during phases 1 and 2 ($(dm/dt)_1$ and $(dm/dt)_2$), lag time (t_1), zeta potential of PEM surfaces (ζ), and the free energy of interfacial interaction (ΔG_{sws}). The secondary minima in XDLVO total energy of virus-surface interactions during phases 1 ($E_{min}^{(1)}$) and 2 ($E_{min}^{(2)}$) were used as supplementary variables. Because PEM surface roughness had only minimal effect on XDLVO predictions (Figure B1 and B2 in the Appendix B), it was not included in the PCA.

Figure 16 presents factor loadings and factor scores computed by PCA. More than 80% of variability is captured by the analysis based on the two principal components, PC1 and PC2. The factor loadings graph (Figure 16a) reveals the following correlations:

1. The deposition rate in each of the two phases is correlated to the depth of the secondary minimum of the corresponding XDLVO total energy of interaction: $(dm/dt)_1$ correlates with E_{min1} while $(dm/dt)_2$ correlates with E_{min2} . This result points to the predictive ability of the XDLVO model to describe deposition kinetics.
2. Deposition rates during phase 1 ($(dm/dt)_1$) and phase 2 ($(dm/dt)_2$) are nearly independent. The result is consistent with the premise that phase 1 deposition is governed by virus-surface interactions while phase 2 deposition – by virus-virus interactions.
3. The time of deposition during phase 1, t_1 , is countercorrelated with the deposition rate $(dm/dt)_1$. This can be rationalized in terms of the overall capacity of the surface for virus adsorption: the slower the deposition rate the longer it should take to saturate the capacity and to complete phase 1.
4. For the PEMs selected in this study, hydrophobicity and negative charge are counter correlated: regardless of the ionic strength of the PEM deposition solution (I_{LbL}), positively charged [PSS/PDAD]₄ surfaces are

more hydrophobic than the negatively charged [PSS/PDAD]₄[PSS] surfaces. Indeed, as shown in Table 4, both [PSS/PDAD]_{4.5} are strongly hydrophilic ($\Delta G_{sws} = 44.3$ and 45.2 mJ/m²) while [PSS/PDAD]₄ are either hydrophobic (-16.3 mJ/m²) or only slightly hydrophilic (6.7 mJ/m²). Because PEM hydrophilicity and negative charge both deter attachment of negatively charged MS2, the present selection of PEM surfaces is not optimal for separating the effects of these two PEM properties on MS2 deposition. Comparing a positively charged and hydrophilic PEM against a negatively charged and hydrophobic counterpart would bode better for such analysis.

Figure 16b presents factor scores for PEMs. Several general observations could be made:

1. The first principal component (PC1) separates the positively-charged [PSS/PDAD]₄ surfaces (negative PC1 domain) with high $(dm/dt)_1$ and ζ from the negatively-charged [PSS/PDAD]_{4.5} surfaces (positive PC1 domain) with high t_1 and ΔG_{sws} .
2. The second principal component (PC2 axis) separates surfaces based on ionic strength of the MS2 deposition solution (I_{MS2}). PEMs exposed to $I_{MS2} = 100$ mM NaCl (domain of positive and near-neutral PC2 values) are characterized by larger $(dm/dt)_2$ than PEMs exposed to $I_{MS2} = 10$ mM NaCl (negative PC2 domain).

3. The surfaces are grouped largely by the surface charge (and hydrophilicity, which is correlated with negative charge in the present case). Less hydrophilic and positively charged surfaces were characterized by much faster deposition kinetics during phase 1. In Figure 16b, the grouping is illustrated using solid shades. One surface -100-[PSS/PDAD]₄-100 - did not follow the grouping pattern due to its relatively low $(dm/dt)_1$ but high $(dm/dt)_2$. The QCM-D result showed that 100-[PSS/PDAD]₄-100 gained more viral mass than other -[PSS/PDAD]₄ surface after 1-hr virus deposition. Even though 100-[PSS/PDAD]₄ was more positive and hydrophobic than 10-[PSS/PDAD]₄, the high ionic strength ($I_{MS2} = 100$ mM) screened EL interactions, resulting in a weak adsorption during phase 1. During phase 2, however, the same effect of screening helped overcome the repulsive interactions between MS2 and MS2-coated surface.

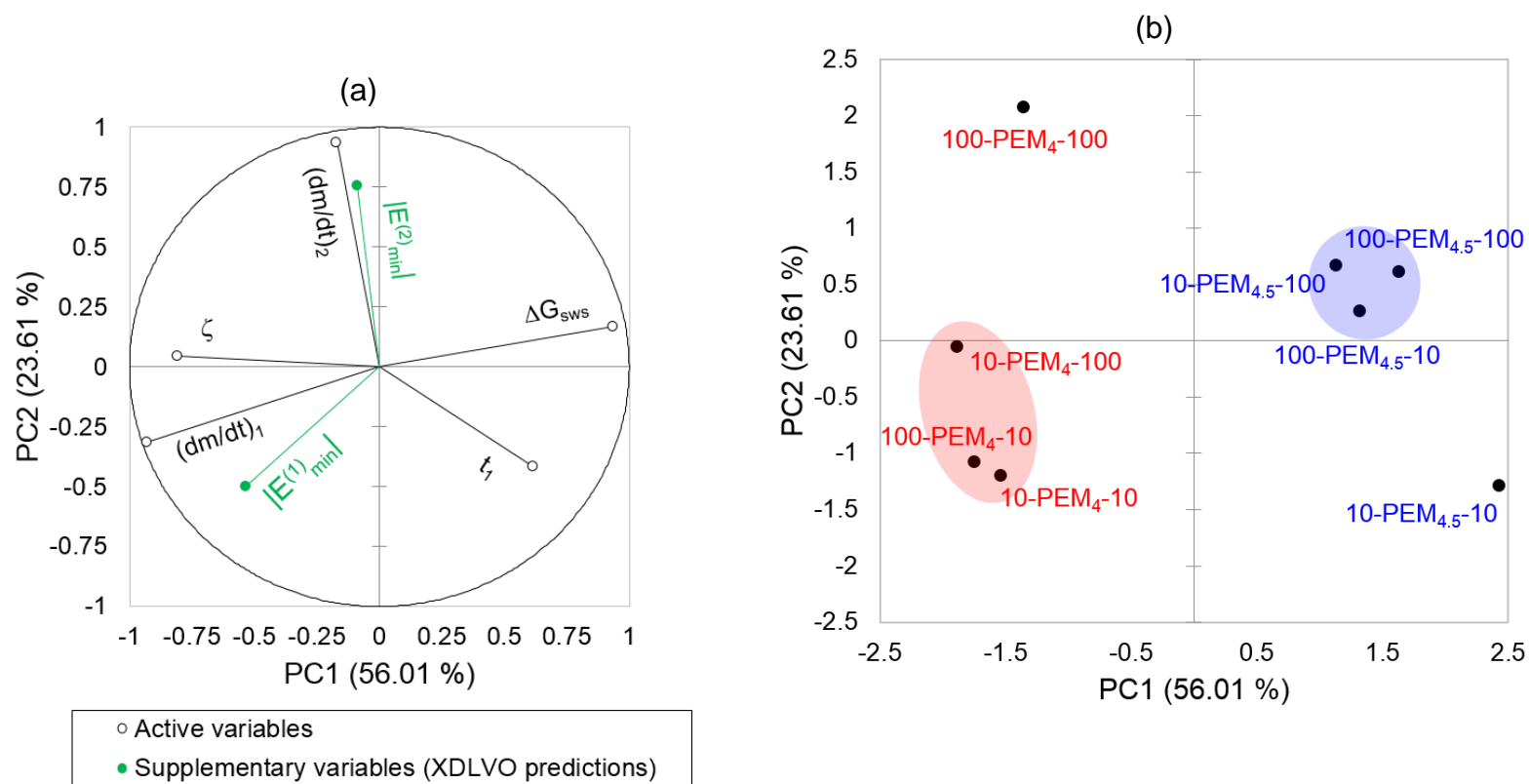


Figure 16: Principal component analysis (PCA): factor loadings (a) and factor scores (b)

4.4. Conclusions

Attachment of bacteriophage MS2 on the positively-and negatively-charged polyelectrolyte-coated surfaces was studied using quartz crystal microbalance with dissipation (QCM-D). The polyelectrolyte multilayers were terminated by with a cationic or an anionic polyelectrolyte and deposited from two different solutions (10 mM and 100 mM NaCl) yielding the total of four different coating types. Two deposition phases occurred in two distinct phases: the initial phase (phase 1) when the surface is relatively virus-free and phase 2 when the surface charge is affected by the viruses accumulated on the surface. The trends can be rationalized in terms of virus-surface interactions. The attractive electrostatic interactions between MS2, which is the negatively-charged at pH 7. The increase in ionic strength of the MS2 deposition solution, I_{MS2} , from 10 mM to 100 mM mitigated the effects of electrostatic interactions, i.e. decreased both repulsive interactions with surfaces carrying the electrical charge of the same sign and attractive interactions with the surfaces carrying the charge of the sign opposite to that of the virus. XDLVO theory showed that MS2 adsorption was governed by both electrostatic and hydrophobic interactions while van der Waals interaction played a relatively minor role. Surface roughness did not have a significant effect on MS2 deposition. The results point to the potential use of polyelectrolyte multilayers as surface coatings for controlling virus adhesion to reduce human exposure to viruses.

CHAPTER 5: SUGGESTED FUTURE RESEARCH: ATTACHMENT OF AIRBORNE VIRUSES TO HUMAN SKIN AND PERSONAL CARE PRODUCTS AS A FUNCTION OF ENVIRONMENTAL PARAMETERS

5.1. Introduction

Human skin functions as a semipermeable epidermal barrier that prevents loss of moisture and invasion of toxic substances as well as microbes [123]. Human skin is complex and, even when healthy, provides an elaborate habitat for organisms to live on. This resident microbiota includes commensal and pathogenic bacteria [124], viruses [125-128], and fungus [129]. They can be either harmless or pathogenic; the latter are of especially concern when the skin barrier is impaired [130]. There has been numerous reports on human skin diseases caused by microbes. For example, psoriasis affects 2 to 3 % of the population worldwide and is triggered by varying factors including *Malasseria* species [129, 131]. Atopic dermatitis affects ~20% of the population in developed countries [123, 132] and is associated with microbial infection [133]; of which more than 90% of correspond to *S.aureus*. High numbers of *Propionibacteria*, *Staphylococci* and *Malassezia* are detected on skin of patients with acnes [134].

Human *Papillomavirus* (HPV) was reported to cause commensal skin infections, associating with cutaneous and mucosal lesions and even anogenital cancers. Skin swab samples were taken from 50 individuals from each country and HPV was tested positive for 70% of the Swedish individuals, 68% of the Bangladesh

individuals, 54% of the Japanese individuals, 52% of the Ethiopian individuals and 42% of the Zambian individuals [135].) *Polyomaviruses*, *Papillomaviruses* and *Circoviruses* – all pathogenic viruses - were also detected on a healthy-appearing human skin [125]. A study on viral antigen in mice' brain by Esiri et al. [136] showed that facial skin is one of the most common site for herpes virus (HSV) to target the central nervous system. In the U.S., HSV-1 affects more than 35% of African-American children, 18% of white children at age 5 and approximately 5 to 10% university students every year [128].

Most of Americans use cosmetics in daily basic such as skin care products (moisturizers, sun creams), facial makeup (lipsticks, mascaras, eye shadows) and hair products (conditioners, gels and mousses). However, these products are considered to be a transmission pathway that picks up microbes normally present on human skin or eyelashes [137], incubate or even nourish these microbes with substances such as animal proteins and vitamins [138] to cause skin infection. Even though most of cosmetics products contain preservatives to prevent microbial activities, these chemicals may not be efficient to inhibit microbial growth [139] or even be inactivated by other substances such as animal proteins and vitamins [138].

In the period from October 1993 through September 1998, 1,370 food and cosmetic products, accounting for 36% of the recalls by U.S. Food and Drug Administration were associated with microbial contamination; of which *pseudomonas aeruginosa* was the most popular agent found in the cosmetic

products [140]. A study by Pack et al. [137] on microbial contamination of mascaras after 3 months of use by forty women showed that 36.4% of the mascara tubes was contaminated with microbes, most commonly *Staphylococcus epidermidis*, *Streptococcus* species and fungi. A test on quality of hair and skin care cosmetics in Jordan showed that 5.3% of 57 brands were contaminated with microbes at less than 10^2 CFU g⁻¹ and 28% at more than 10^4 CFU g⁻¹; *Bacillus* species, *Pseudomonas spp.* and *Staphylococci* were most frequently detected and inadequate preservative efficacy was accounted for 28.1% of the contaminated products [139].

Skin microbiota have been studied widely to identify bacterial and fungal species. Studies on viral contamination, however, have been limited due to the difficulties of cultivation and sequencing [125]. Skin infection was often blamed on specifics of cosmetic product usage (e.g. person-to-person transfer due to shared use of the product from the same container) [138]. However, another possible cause of skin infection could be adsorption of airborne viruses to human skin – bare or with cosmetics applied. The current lack of knowledge about related mechanisms of virus transport and fate motivated the research proposed herein.

5.2. Experimental

5.2.1. Cosmetic products

The cosmetic products will be selected based on three criteria: (1) sale volumes; (2) processability into a homogenous coating (this criterion will be examined

using SEM); (3) coverage of a range adhesion properties. Silica colloids will be first used for adhesion tests to scope out products' adhesion properties.

All the facial products will be purchased from L'Oréal Paris, a company that has been ranked as the most powerful and valuable cosmetics brand of the world for three years by Brand Finance with a total brand value of \$13.7 billion.

Suggested makeup products include oil-free (Super Blendable), waterproof (Advanced Never Fail) and long-lasting (Total Cover) foundations. Suggested skincare products are facial moisturizer (RevitaLift Daily Volumizing), facial oil (Age Perfect Cell Renewal Facial Oil Light), facial serum (RevitaLift Triple Power Concentrated) and sun cream (Age Perfect Day Cream SPF 15). Hair cosmetics includes gels (Advanced Hairstyle LOCK it Clean Style) and mousses (Advanced Hairstyle AIR DRY it Ruffled Body).

5.2.2. QCM-D procedure

Coating cosmetic products on a QCM-D sensor

Coating thin films of cosmetic products on a QCM-D sensor can be done either in situ within the QCM-D chamber (Figure 17) or using spin-coater. Prior to coating, the cosmetic product is diluted with DI water 10 to 100 times depending on its viscosity. The diluted product will then then pumped through the QCM-D chamber with clean sensors at a flow rate of of ~ 0.15 mL/min until the frequencies stabilize (i.e. achieve high signal-to-noise ratio) and level off (i.e. the average frequency reaches a steady state value). The coated-surfaces will be

characterized in terms of roughness using AFM. The overall morphology will be accessed using SEM (see *section 3.2.9* in Chapter 3).

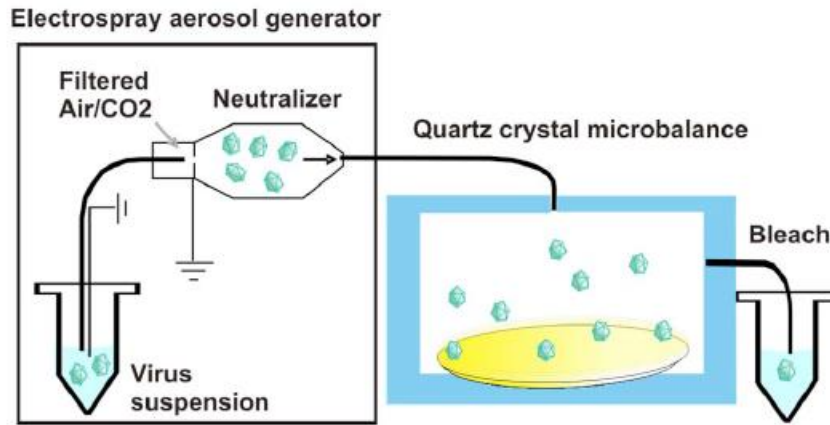


Figure 17: Schematics of QCM-D with electro spray aerosol generator (source: Lee et al. [117]).

When using a spin-coater, the cosmetic product will be diluted as much as possible to make a complete but thin film so that QCM-D resonance can be found. The diluted product will be pipetted onto a QCM-D sensor, followed by spin-coating at 2000 rpm for 30 s. The coated sensor will then be dried at the ambient temperature for about 10 min before being inserted into the QCM-D chamber for virus adsorption tests.

Virus deposition

An initial virus concentration of 10^9 – 10^{11} particles/mL will be aerosolized and neutralized using an electrospray aerosol generator before transported to contact with the cosmetics-coated surfaces within the QCM-D instrument. The gas flow rate will be kept constant at 4.0, 2.0 and 1.0 L/min. Humidity could be controlled by regulating the relative flow rate of the carrier gas (air and CO₂) and virus aerosol. Mass of virus adsorbed to the surface and viscoelastic properties of the adsorbed layer will be determined based on recorded frequency and dissipation shifts every min, respectively.

5.3. Objectives and hypotheses

Objective 1: Evaluate the effects of environmental parameters (wind velocity and humidity) on virus adsorption to cosmetics-coated surfaces.

Hypothesis 1: An increase in gas flow rate would result in an increase in virus adsorption rate; however, the adsorbed mass would achieve a steady state value faster.

Objective 2: Evaluate the effects of virus properties (enveloped and undeveloped RNA, sizes, charge and hydrophobicity) on virus adsorption to cosmetics-coated surfaces.

Hypothesis 1: Larger and more hydrophobic viruses adsorb more favorably to surfaces.

Objective 3: Evaluate the effects of properties of skin care products (hydrophobicity and surface roughness) on virus adsorption.

Hypothesis 3: Products with more hydrophobic and rougher surface are more attractive to viruses.

Objective 4: Evaluate the effects of properties of hair products (hydrophobicity and charge) on virus adsorption.

Hypothesis 4: Products with more hydrophobic surface and less negative charge are more attractive to viruses.

Objective 5: Compare mass of virus adsorbed to bare skin and to cosmetics-coated surfaces.

Hypothesis 5: Virus adsorb more favorably to coated-surfaces than to bare skin.

APPENDICES

APPENDIX A

Attachment of Human Adenovirus 40 and Bacteriophage MS2 onto Household Paints

A1. XDLVO calculation and deposition kinetics for viruses

Table A1: Results of XDLVO modeling (values of energy barriers, E_{max} , and secondary energy minima, E_{min} , in XDLVO energy profiles (Figures 5, 6)), and of QCM-D experiments (mass deposition rates for phase 1, $\left(\frac{dm}{dt}\right)_1$, and phase 2, $\left(\frac{dm}{dt}\right)_2$, as well as deposition lag time, t_1 (Figures 9)) for HAdV40 deposition to painted surfaces.

* Values used as active variables in the PCA (Figure 11a and 11b)

** Values used as supplementary variables in the PCA (Figure 11a)

Experiment code	Phase 1				Phase 2		
	t_1^* min	$\left(\frac{dm}{dt}\right)_1^*$ (ng/cm ² /min)	$E_{min}^{(1) **}$ (kT)	$E_{max}^{(1)}$ (kT)	$\left(\frac{dm}{dt}\right)_2^*$ (ng/cm ² /min)	$E_{min}^{(2) **}$ (kT)	$E_{max}^{(2)}$ (kT)
1-HAdV-LW-3.5	0.10	84.96	0.00	0.00	1.18	0.12	10.36
1-HAdV-LW-6.0	0.17	25.33	0.00	36.79	3.43	0.11	19.08
150-HAdV-LW-5.2	0.12	71.47	0.00	0.00	8.14	0.00	0.00
150-HAdV-LW-7.2	0.17	43.96	0.00	0.00	10.38	0.00	0.00
1-HAdV-AW-3.5	0.10	85.16	0.00	0.00	0.53	0.12	10.36
1-HAdV-AW-6.0	0.12	12.24	0.09	24.60	2.83	0.11	19.08
150-HAdV-AW-5.2	0.12	57.03	0.00	0.00	5.67	0.00	0.00
150-HAdV-AW-7.2	0.17	46.76	0.00	0.00	8.37	0.00	0.00
1-HAdV-AO-3.5	0.12	60.16	0.11	11.19	0.00	0.12	10.36
1-HAdV-AO-6.0	0.10	69.70	0.10	32.30	1.67	0.11	19.08
150-HAdV-AO-5.2	0.17	12.26	0.00	0.00	6.20	0.00	0.00
150-HAdV-AO-7.2	0.20	36.30	0.00	0.00	11.27	0.00	0.00

Table A2: Results of XDLVO modeling (values of energy barriers, E_{max} , and secondary energy minima, E_{min} , in XDLVO energy profiles (Figures 7, 8)), and of QCM-D experiments (mass deposition rates for phase 1, $(\frac{dm}{dt})_1$, and phase 2, $(\frac{dm}{dt})_2$, as well as deposition lag time, t_1 (Figure 10)) for MS2 deposition to painted surfaces.

Notes:

* Values used as active variables in the PCA (Figure 11a and 11b)

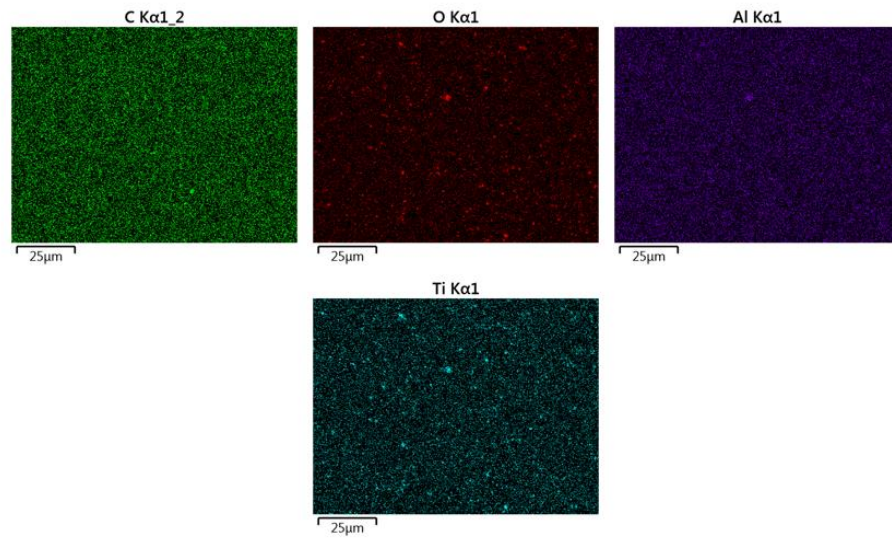
** Values used as supplementary variables in the PCA (Figure 11a)

† The lag time estimated using linear regression was ~14 min (Figure 10a). This time was selected as the start of deposition phase1. Due to the limited duration of the QCM-D test, Phase 2 was not observed. For completeness of PCA calculations (Figure 11), $(\frac{dm}{dt})_2$ in this test was assumed to be equal to $(\frac{dm}{dt})_1$.

Experiment code	Phase 1				Phase 2		
	t_1^* min	$(\frac{dm}{dt})_1^*$ (ng/cm ² /min)	$E_{min}^{(1) **}$ (kT)	$E_{max}^{(1)}$ (kT)	$(\frac{dm}{dt})_2^*$ (ng/cm ² /min)	$E_{min}^{(2) **}$ (kT)	$E_{max}^{(2)}$ (kT)
1-MS2-LW-3.5	0.00	0.00	0.00	261.41	3.22	0.04	558.53
1-MS2-LW-6.0	0.00	0.00	0.00	293.50	0.76	0.00	591.38
100-MS2-LW-3.5	0.00	0.00	0.03	261.98	4.23	0.51	558.36
1-MS2-AW-3.5	0.00	0.00	0.04	339.81	1.73	0.04	558.53
1-MS2-AW-6.0	0.00	0.00	0.00	350.61	0.00	0.00	591.38
100-MS2-AW-3.5	0.00	0.00	0.43	339.63	4.23	0.51	558.36
1-MS2-AO-3.5	0.00	0.00	9.68	113.42	2.54	0.04	558.53
1-MS2-AO-6.0	0.00	0.00	0.00	180.94	0.40	0.00	591.38
100-MS2-AO-3.5	0.00	0.00	0.61	130.82	4.23	0.51	558.36

A2. SEM images and elemental analyses from the paints-coated surfaces

A2.1. Latex water-based paint



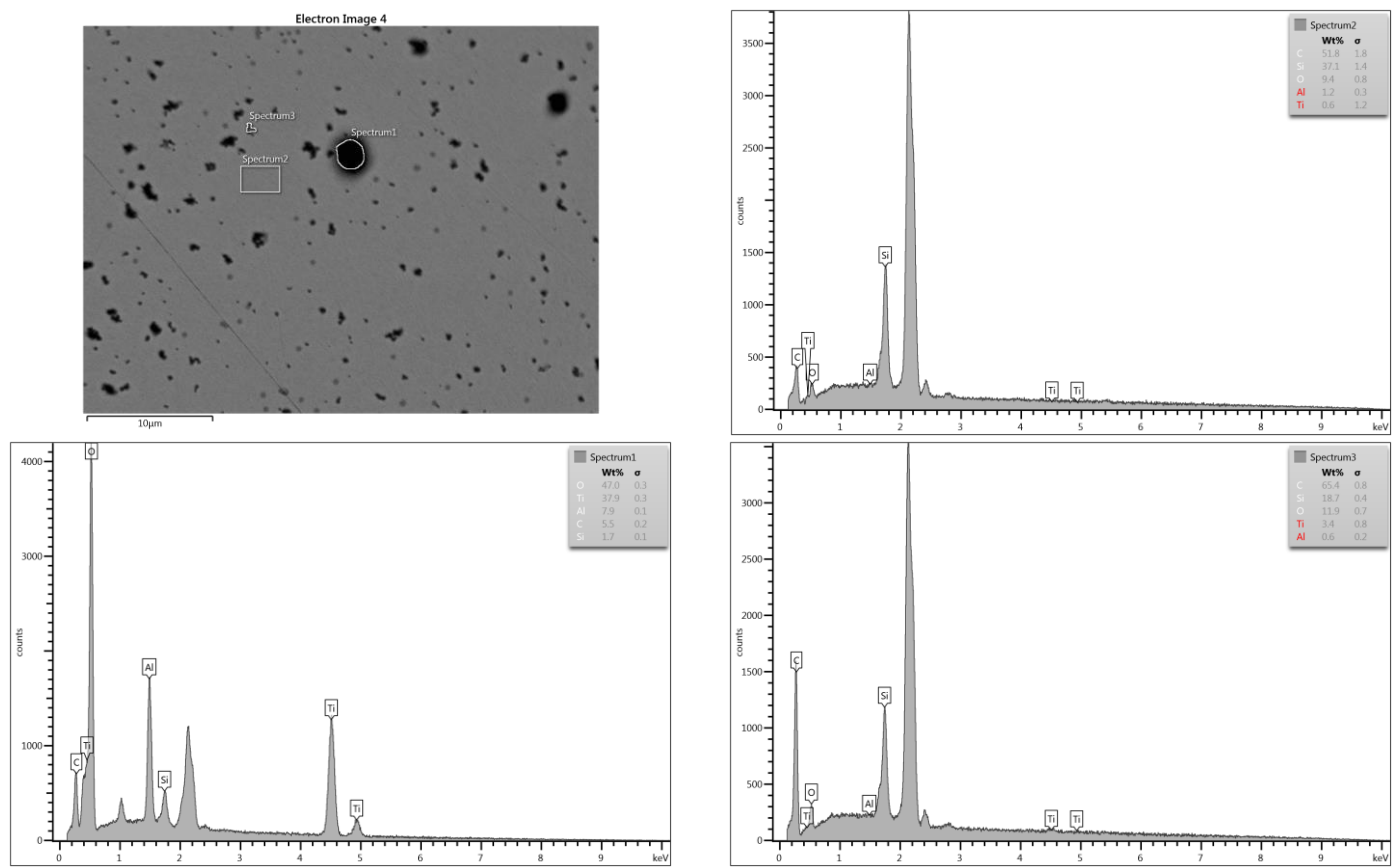
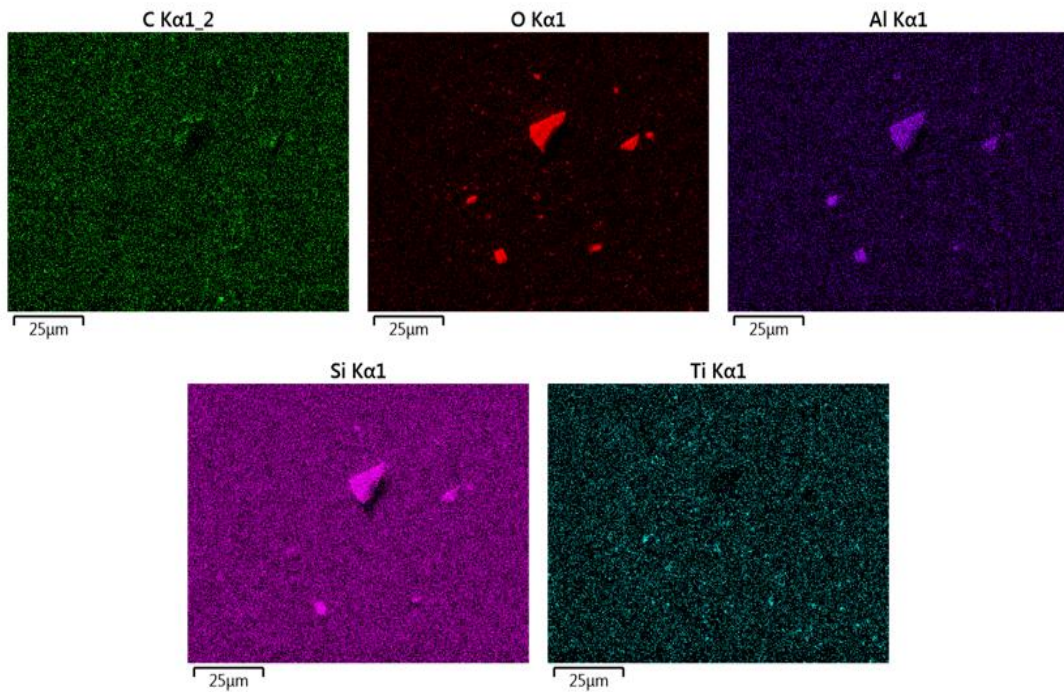


Figure A1: SEM image and elemental analyses for latex water paint-coated surface

Figure A1 shows SEM image and elemental analyses for latex water paint-coated surface. Based on the safety data sheet provided by BEHR, latex water-based paint composed of acrylic latex as the binder and pigments such as TiO_2 (10-30%), SiO_2 (1-5%) and $\text{Al}(\text{OH})_3$ (1-5%). Therefore, Ti, Si, Al, C, O and H were expected to see in the EDS analyses. The SEM image showed small dark islands scattering over the paint film, indicating two different morphologies. We chose three areas for elemental analysis: dark islands labeled as spectrums 1 and 3 and background area labeled as spectrum 2. In spectrums 1 and 3, we found O (11.9 -47%), Ti (3.4 - 37.9%), Al (0.6 - 7.9%), C (1.7 - 65.4%) and Si (1.7 – 18.7%). These elements were components of the pigments so the dark islands referred to accumulated pigments. The weights of Ti and Al in the spectrum 3 were less than those in spectrum 1 because the sampling zone for spectrum 3 covered a large portion of the film background. In spectrum 2, C (51.8%), Si (37.1%) and O (9.4%) were found as the dominating elements. Traces of Al (1.2%) and Ti (0.6%) were also detected. A high concentration of Carbon, one of the three constituents (C, O, H) of the binder revealed that this area is covered mostly with acrylic latex binder. The appearance of Al and Ti traces accounted for small amount of pigments in this area. The EDS analyses suggested that the paint-coated sensor was fully covered with the binder; however, pigments did not evenly contribute over the film but had tendency to accumulate in local areas as islands. In addition to the elements that were included in the paint, we also found a high percentage of Au (not labeled in the spectrums) in the list of elements detected from our samples analysis. Gold is not a component of the paint but

used for coating a thin layer (~100 nm) on a sensor. At a voltage of 10 kV, the X-ray could penetrate a depth of ~0.2 μm through the paint film into the sensor substrate to pick up on gold. A high percentage of Si (18.7-37.1%) was detected in the film background while this element accounted for less than 5% of the paint, possibly due to the penetrating of X-ray into the QCM-D substrate.

A2.2. Alkyd water-based paint



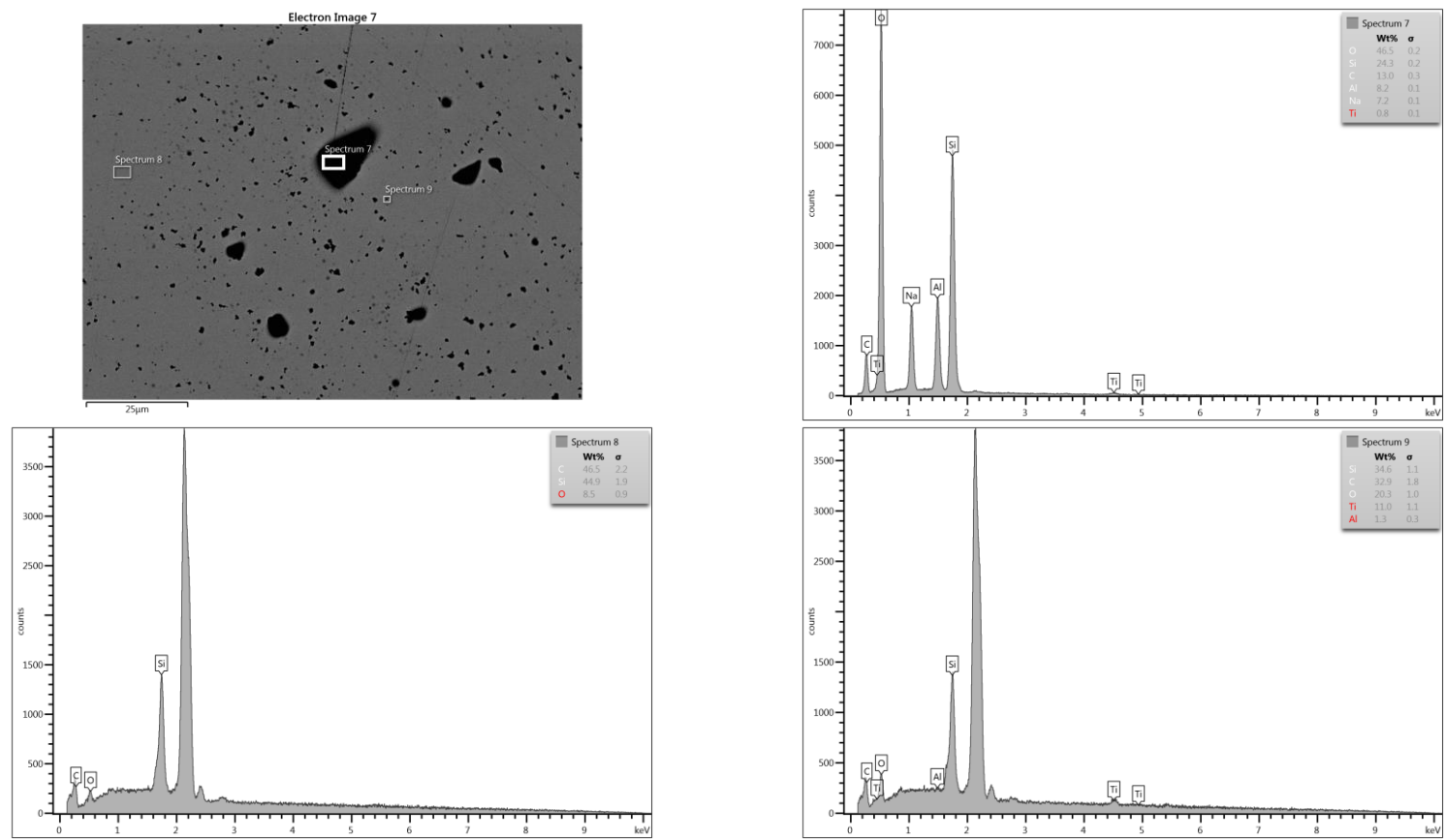
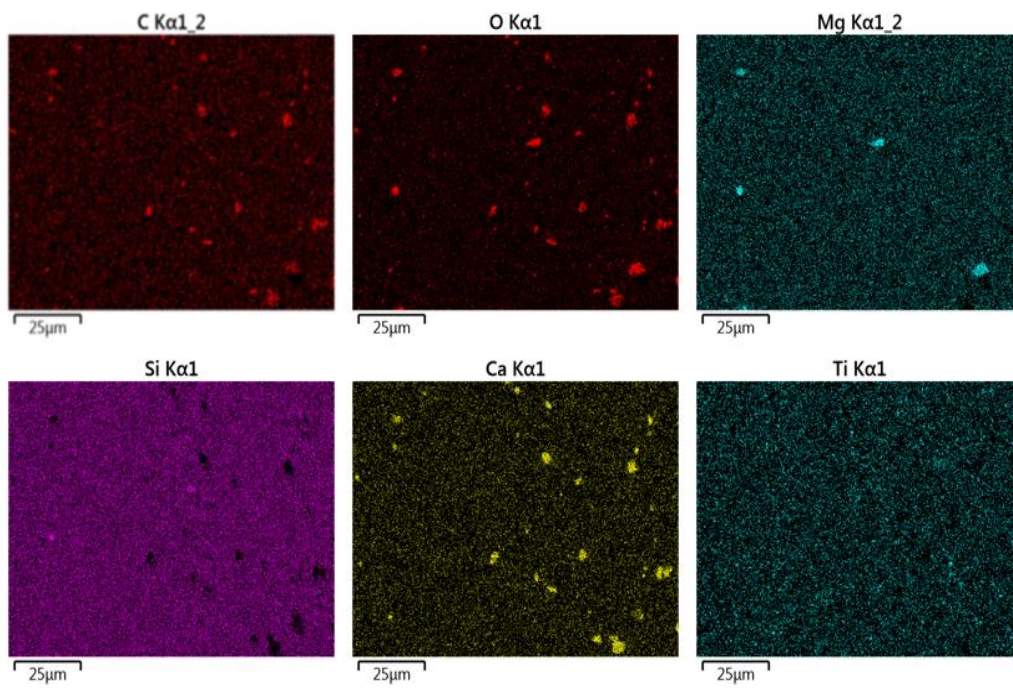


Figure A2: SEM image and elemental analyses for alkyd water paint-coated surface

Figure A2 shows SEM image of the alkyd water paint-coated surface and its elemental analyses. Alkyd water-based paint had alkyd as the binder and the same composition of pigments (TiO_2 (10-30%), SiO_2 (1-5%) and $\text{Al}(\text{OH})_3$ (1-5%)) as that in latex water-based paint. Therefore, we expected to find the same composition of the elements (e.g., Ti, Si, Al, C, O and H) in the EDS analyses. Based on the SEM image of the paint-coated sample, we also selected three different locations for EDS analysis: dark islands labeled as spectrums 7 and 9 and an area of the film background labeled as spectrum 8. In spectrums 7 and 9, the predominant elements found were O (20.3 -46.5%), Si (24.3 – 34.6 %) and C (13 – 32.9 %), followed by Al (1.3 - 8.2%), Na (7.2%) and Ti (0.8 – 11.0 %). As expected, these elements were constituents of the pigments so the dark islands in the SEM image corresponded to accumulated pigments. There was a fair amount of Na detected in our measurement, probably due to contamination. In spectrum 8, we found Carbon as the dominant element, accounting for 46.5%, followed by Oxygen (8.5%). These elements were main ingredients of the binder so the film background was mainly composed of the binder. Again, there were high amounts of Gold (not labeled in spectrums) and Silica found in our EDS analyses. These elements belonged to the composition of the QCM-D sensor.

A2.3. Alkyd oil-based paint



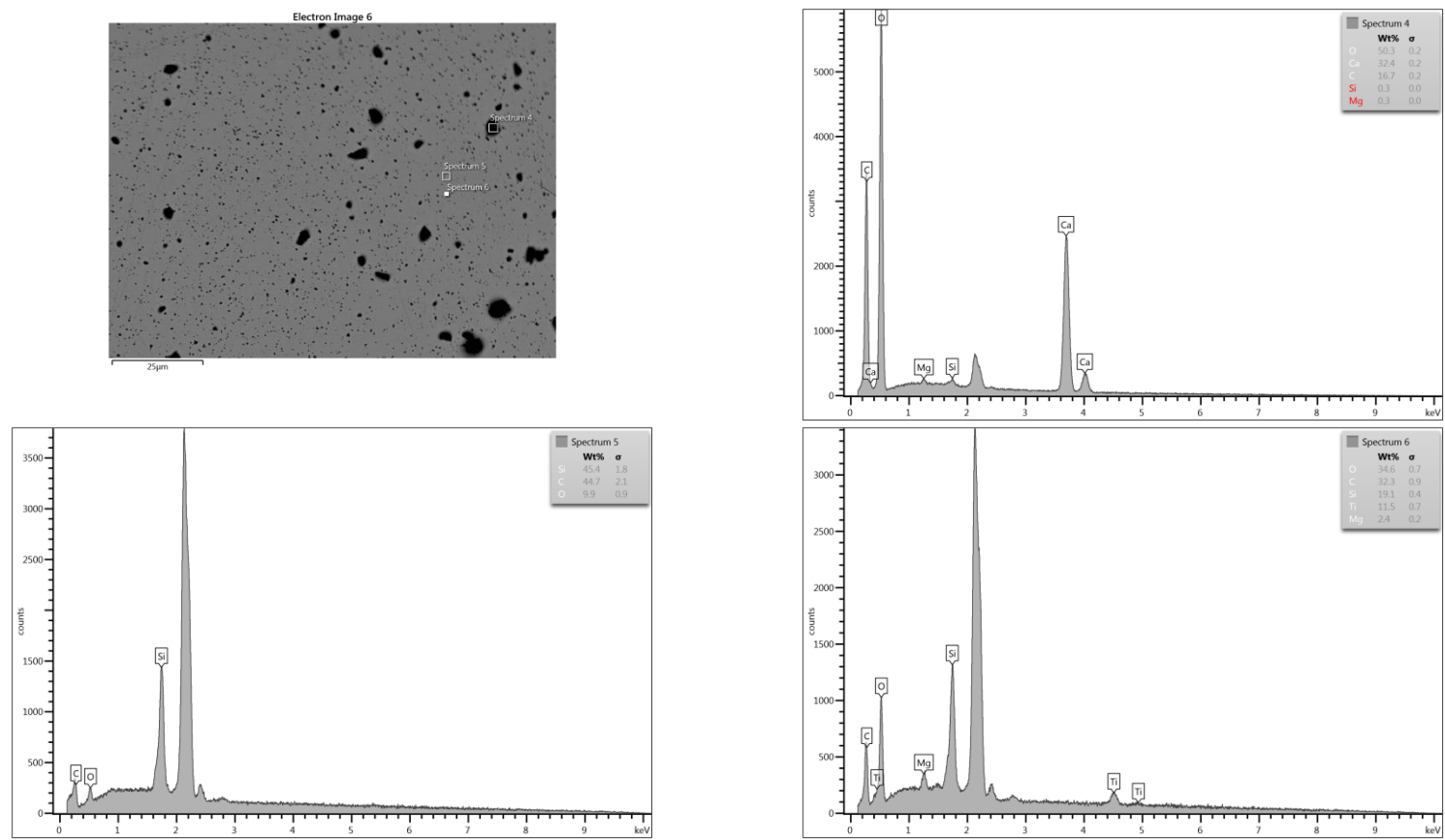


Figure A3: SEM image and elemental analyses for alkyd oil paint-coated surface

Figure A3 shows SEM image of the alkyd oil paint-coated surface and its elemental analyses. Based on the safety data sheet provided by BEHR, alkyd oil-based paint had alkyd as binder, petroleum as solvent and pigments such as TiO_2 (10-30%), SiO_2 (1-5%), CaCO_3 (1-5%) and $\text{Mg}_3\text{Si}_4\text{O}_{10}(\text{OH})_2$ (1-5%). Similar to what we observed in the SEM images for both latex and alkyd water-based paints, the SEM image of alkyd oil-based paint also showed dark spots over the paint film. These dark spots (spectrums 4 and 6) mainly composed of pigments with 34.6 - 50.3% O, 32.4 % Ca, 16.7- 32.3 % C, 0.3 -19.1 % Si, 11.5 % Ti and 0.3 – 2.4 % Mg. The film background (spectrum 5) composed mostly of alkyd where Carbon and Oxygen accounted for 44.7% and 9.9%, respectively. A large amount of Si (45.1%) and Au (not labeled in the spectrums) appeared in spectrum 5, contributed by the sensor's composition.

A3. SEM images and elemental analyses on the cross-section of the latex water paint

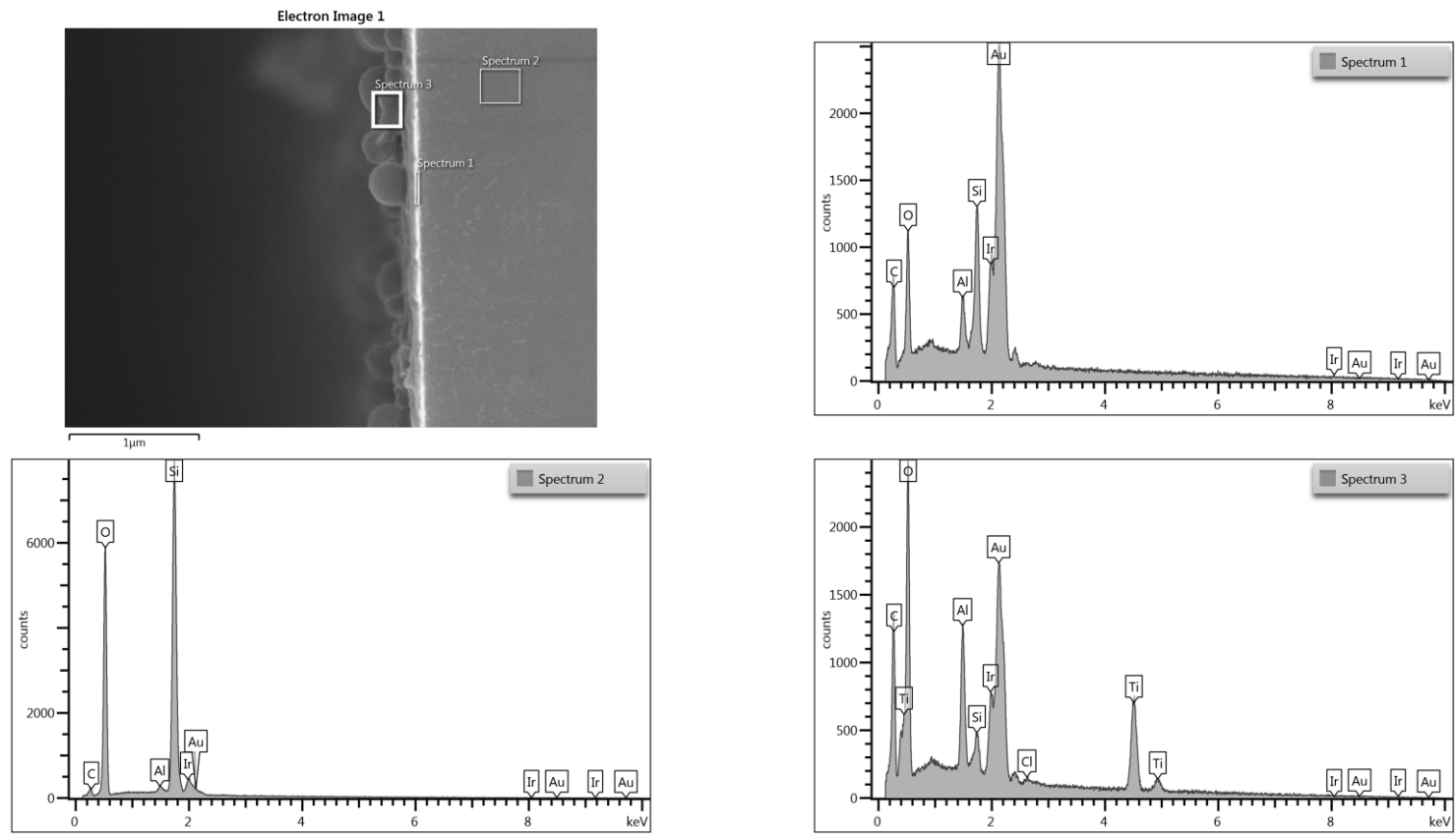


Figure A4: SEM images and elemental analyses on the cross-section of the latex water paint

Figure A4 shows SEM image of the cross-section of the latex water paint-coated surface and its elemental analyses. Based on the SEM image, we selected three different areas for elemental detection. These areas were labeled as spectrum 1, 2 and 3, locating on the cross-sections of the gold layer of the QCM-D sensor, QCM-D sensor substrate and paint film. In spectrum 1, Au was detected as a dominant element in that area, as expected for Au layer of QCM-D sensor. In addition to Au, other elements such as Si, Ir, O, Al and C were also detected; in which Ir was used to cover the sample with a thin layer (~2.7 nm) in attempt to create conductivity prior to the measurement. Other elements were components of the paint that accidentally fell on the cross-section of Au layer during sample fracturing process. In the spectrum 2, Silica was picked up as a major element in this area, consistent with composition of the QCM-D sensor. We also detected O and C as components of the paints in this area due to contamination. In the spectrum 3, we found almost all elements in the pigments (e.g., Ti, O, Si, Al). Gold was also found in the list of detected elements due to contamination.

A4. AFM measurement

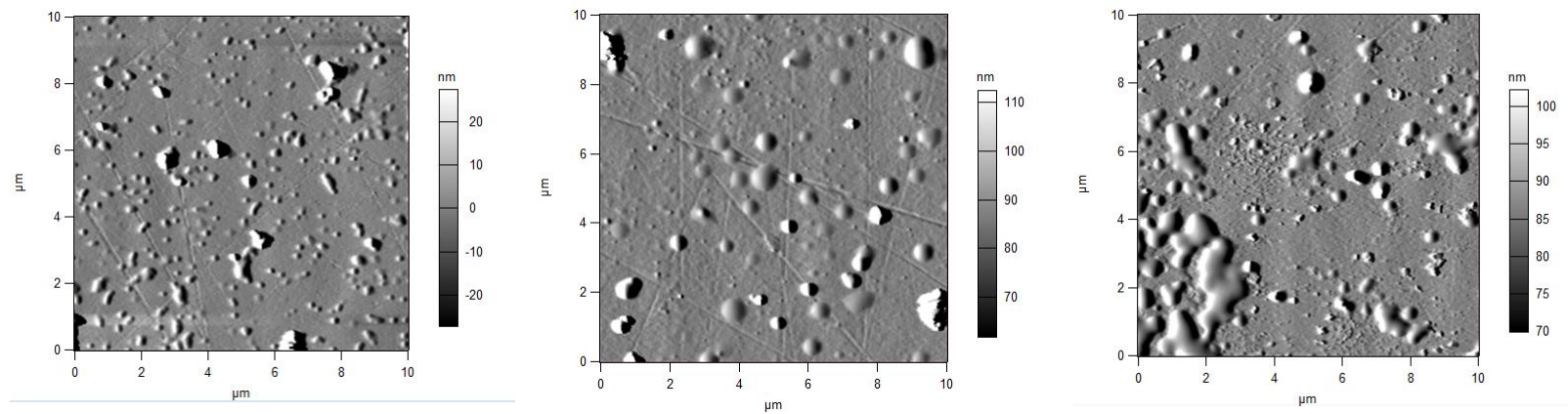


Figure A5: AFM images of latex water, alkyd water and alkyd oil-based paints

The AFM images for the paint-coated surfaces show that surface roughness of latex and alkyd water-based paints and alkyd oil-based paint was 24.2, 28.2 and 16.1 nm, respectively. The water-based paints made rougher coating surfaces than that of the oil-based paint.

A5. Dissipation shifts in 1 h virus deposition to the paint-coated surfaces

Figure A5 show dissipation shifts as a function of time in 1 h HAdV40 deposition to the paint-coated surfaces. The dissipation shifts indicate that adsorbed HAdV40 made the surface of the water-based paints relatively softer; while that of the oil-based paint stiffer.

Figure A6 shows dissipation shifts for the water and oil-based paints as a function of time in 1 h MS2 deposition. The dissipation shifts indicated that adsorbed MS2 formed a fairly soft layer. With very little virus adsorption, the dissipation shift for the oil-based paint (Figure A6b) was negative, probably due to rigid conformation of the surface.

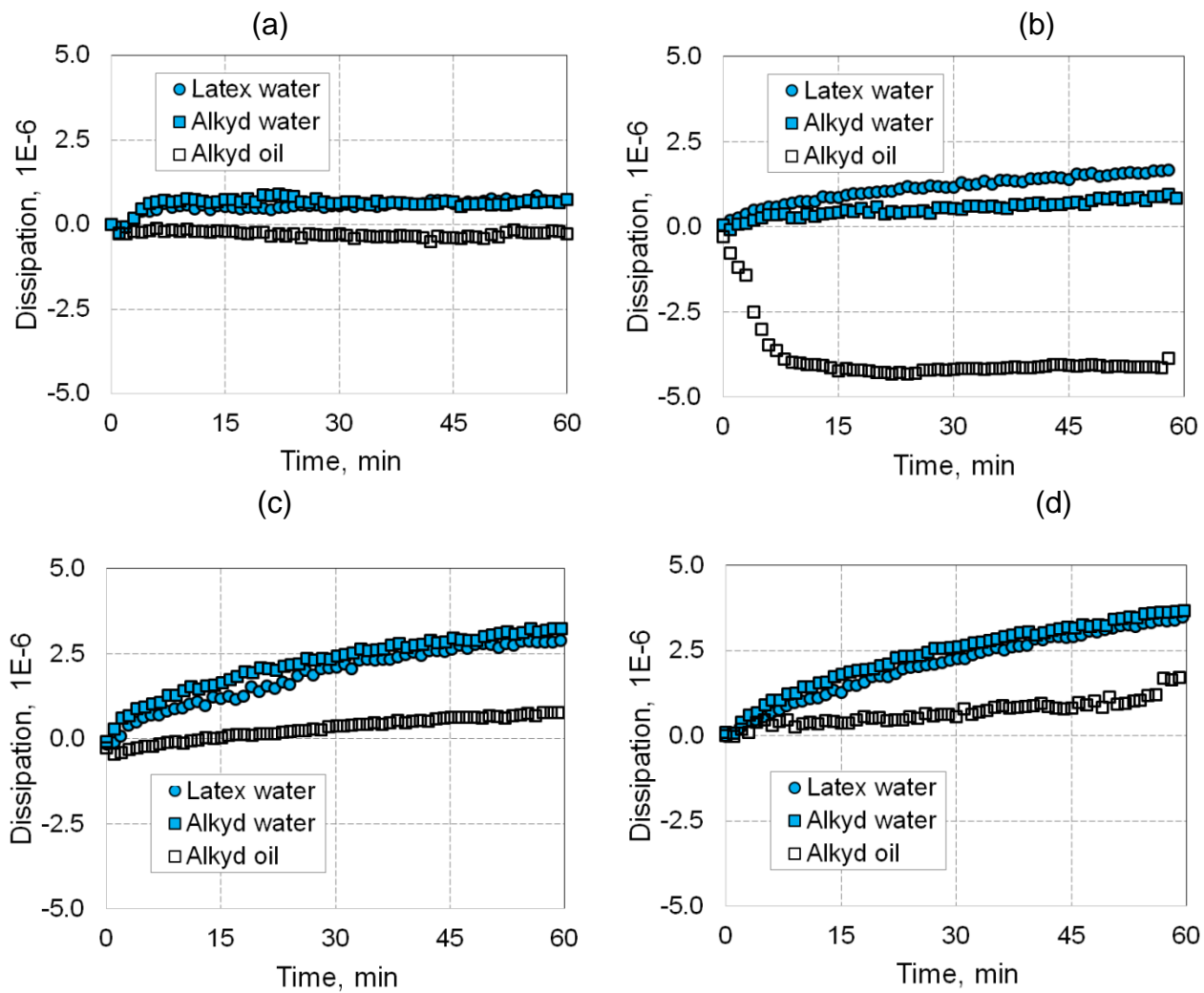


Figure A6: QCM-D dissipation shifts during 1 h of HAdV40 deposition onto three paint surfaces from 1 mM NaCl (a, b) and 150 mM NaCl (c, d) at pH 3.5 (a), pH 6 (b), pH 5.2 (c) and pH 7.2 (d).

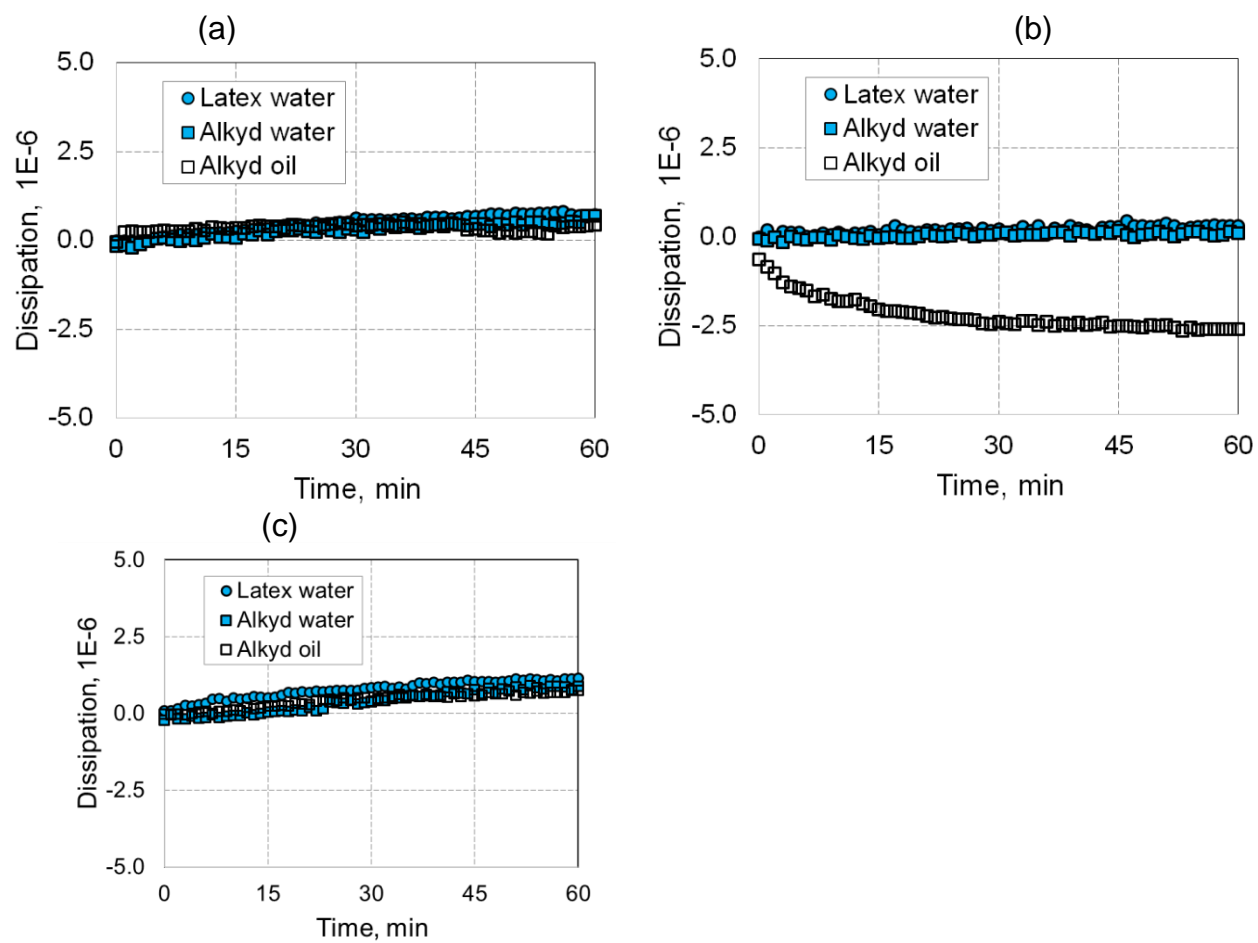


Figure A7: QCM-D frequency shifts during 1 h MS2 deposition onto three paint surfaces from 1 mM NaCl (a, b) and from 100 mM NaCl (c) at pH 3.5 (a, c) and pH 6.0 (b)

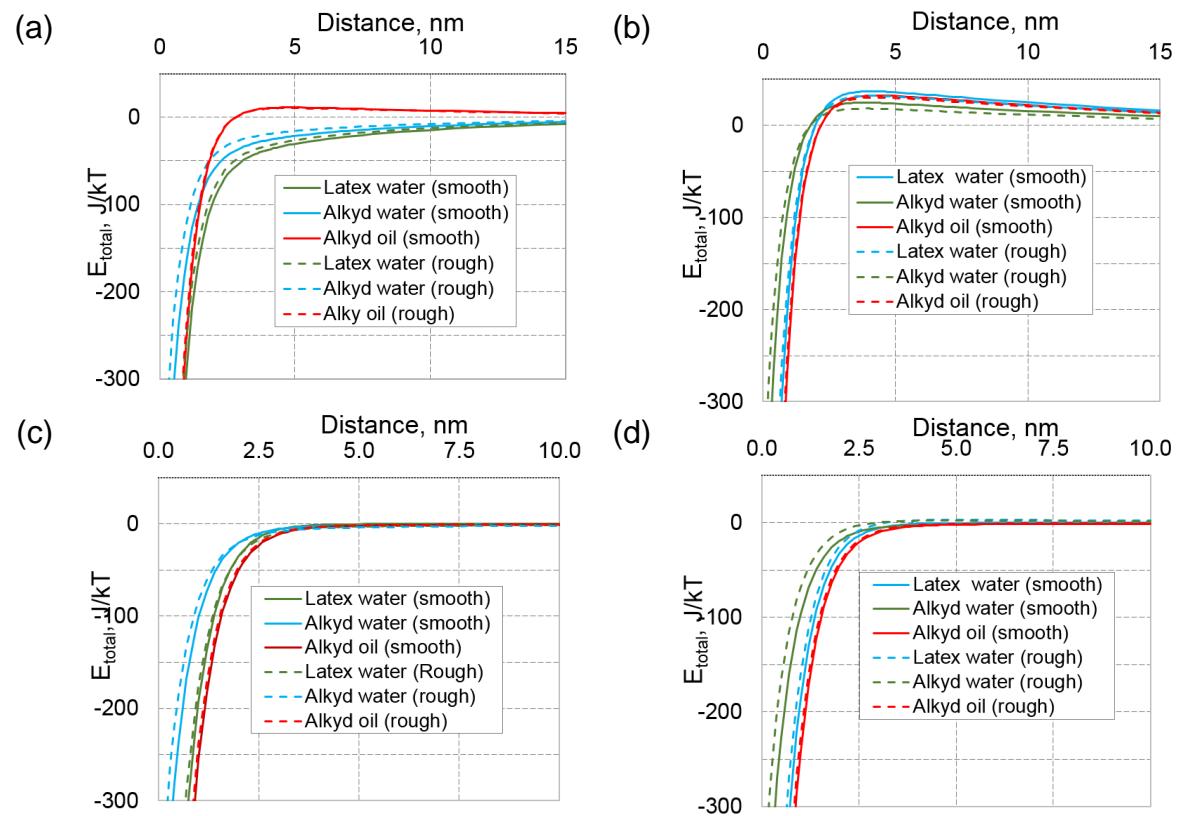


Figure A8: Effect of surface roughness on XDLVO energy of interaction between HADV40 and painted surfaces in 1 mM NaCl (a, b) and 150 mM NaCl (c, d): at pH 3.5 (a), pH 6.0 (b), pH 5.2 (c), pH 7.2 (d) during phase 1 of the deposition process.

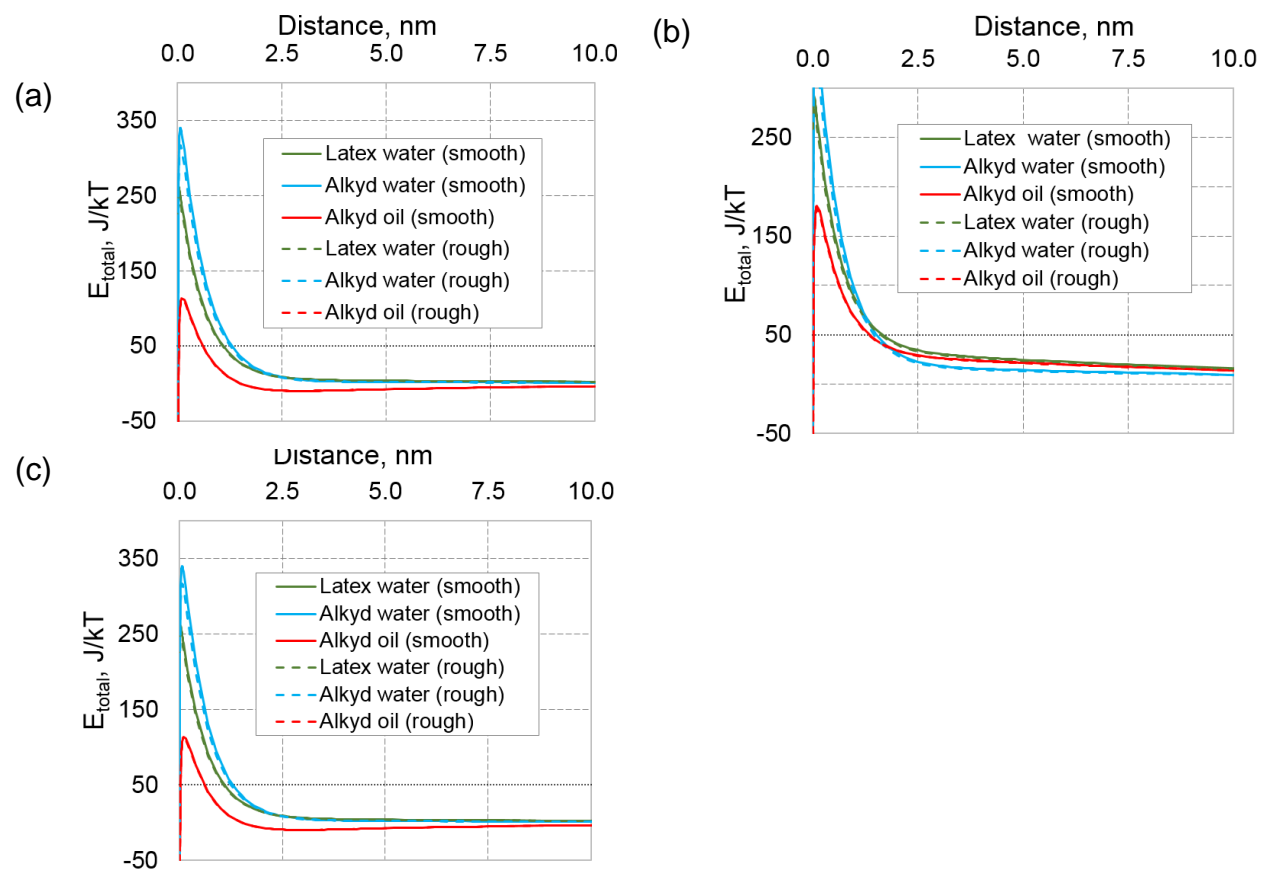


Figure A9: Effect of surface roughness on XDLVO energy of interaction between MS2 and painted surfaces in 1 mM NaCl (a, b) and 100 mM NaCl (c) at pH 3.5 (a, c); pH 6.0 (b) during phase 1 of the deposition process.

APPENDIX B

Deposition of Bacteriophage MS2 onto Polyelectrolyte-coated Surfaces

B1. DLVO and XDLVO theories

The XDLVO theory developed by Van Oss [141] defines the total energy of interaction E_{slv}^{XDLVO} between a particle (such as virus (v)) and a planar surface (s) in liquid medium (l) as a sum of the Lifshitz van der Waals E_{slv}^{LW} , electrostatic double layer E_{slv}^{EL} , and acid-base E_{slv}^{AB} energies:

$$E_{slv}^{XDLVO} = E_{slv}^{LW} + E_{slv}^{EL} + E_{slv}^{AB} \quad (\text{B1})$$

where

$$E_{slv}^{LW} = -A \frac{a}{6d} = -12\pi y_0^2 \Delta G_{y0}^{LW} \frac{a}{6d} \quad (\text{B2})$$

$$E_{slv}^{EL} = \Pi \varepsilon_r \varepsilon_0 a \left[2\psi_c \psi_s \ln \left(\frac{1 + e^{-kd}}{1 - e^{-kd}} \right) + (\psi_c^2 + \psi_s^2) \ln(1 - e^{-2kd}) \right] \quad (\text{B3})$$

$$E_{slv}^{AB} = 2\pi a \lambda \Delta G_{d_0}^{AB} \exp \left(\frac{d_0 - d}{\lambda} \right) \quad (\text{B4})$$

In the expressions above, a is the virus radius, d is the separation distance, ε_r is the dielectric constant of water ($\varepsilon_r = 79$), ε_0 is the relative permittivity in vacuum ($\varepsilon_r = 8.854 \cdot 10^{-12} \text{ CV}^{-1}\text{m}^{-1}$), ψ_c and ψ_s are the surface potentials of the colloid and surface, respectively, k is the reverse Debye length, λ is the characteristic delay length of the AB interaction in water ($\lambda = 0.6 \text{ nm}$), d_0 is the minimum separation distance ($d_0 = 0.158 \text{ nm}$).

The AB and LW free energies of adhesion per unit area (J/m²) at the separation distance d_0 are given by equations (S5) and (S6), respectively:

$$\Delta G_{d_0}^{AB} = 2\sqrt{\gamma_s^+}(\sqrt{\gamma_s^-} + \sqrt{\gamma_v^-} - \sqrt{\gamma_l^-}) + 2\sqrt{\gamma_s^-}(\sqrt{\gamma_s^+} + \sqrt{\gamma_v^+} - \sqrt{\gamma_l^+}) \quad (\text{B5})$$

$$-2(\sqrt{\gamma_s^+ \gamma_v^-} + \sqrt{\gamma_s^- \gamma_v^+})$$

$$\Delta G_{d_0}^{LW} = 2(\sqrt{\gamma_l^{LW}} - \sqrt{\gamma_s^{LW}})(\sqrt{\gamma_v^{LW}} - \sqrt{\gamma_l^{LW}}) \quad (\text{B6})$$

where, γ^+ is the electron acceptor parameter, γ^- is the electron donor parameter, γ^{LW} is the apolar surface tension component, and indices l , s , and v refer to liquid, surface and virus. The surface tension components (γ_s^{LW} , γ_s^+ and γ_s^-) are calculated using eq. (S7) based on the measured contact angles, θ , of three probe liquids (DI, glycerol and diiodomethane) and the known surface tension components of the probe liquids (γ_l^{LW} , γ_l^+ and γ_l^-). The square root of the electron donor parameter ($\sqrt{\gamma^+}$) was calculated to be negative (from -1.1 to -2.1) so the value of γ^+ was assumed to be zero. Negative values of $\sqrt{\gamma^+}$ or $\sqrt{\gamma^-}$ are often reported for microbial cell surfaces due to hydration [94, 142]; this is more likely to occur for surfaces that have higher γ^{LW} and lower water contact angle values.

$$(1 + \cos\theta)\gamma_l^{TOT} = 2\left(\sqrt{\gamma_s^{LW}\gamma_l^{LW}} + \sqrt{\gamma_s^+\gamma_l^-} + \sqrt{\gamma_s^-\gamma_l^+}\right) \quad (\text{B7})$$

The hydrophobicity of a surface can be evaluated based on its free energy of cohesion when immersed in water (ΔG_{sls}). ΔG_{sls} is twice the interfacial tension γ_{sl} between the surface and water:

$$\Delta G_{sls} = -2\gamma_{sl} = 2 \left(\sqrt{\gamma_s^{LW}} - \sqrt{\gamma_l^{LW}} \right)^2 - 4(\sqrt{\gamma_s^+ \gamma_s^-} + \sqrt{\gamma_l^+ \gamma_l^-} - \sqrt{\gamma_s^+ \gamma_l^-} - \sqrt{\gamma_s^- \gamma_l^+}) \quad (\text{B8})$$

A positive value of ΔG_{sls} indicates a hydrophilic surface while a negative value indicates that the surface is hydrophobic.

B2. Estimation of the mass of virus deposited on the QCM-D sensor

The maximum possible mass of *viable* MS2 ($\Delta m^{max} \approx 456$ ng/cm²) deposited per unit area of a QCM-D sensor was estimated by dividing the total mass (M) of the viable virus in the feed by the active area ($A \approx 0.97$ cm² [143]) of the QCM-D sensor:

$$\Delta m^{max} = \frac{M}{A} = \frac{C_v V m_v}{A} = \frac{C_v V \rho_v \pi d_v^3}{A \cdot 6}$$

where C_v is the viable virus concentration in the feed ($C_v = 1.24 \pm 0.07 \cdot 10^{10}$ PFU/mL, see section 2.4), m_v is the weight of one MS2 bacteriophage, ρ_v is the density of the virus (for MS2, $\rho_v = 1.38$ g/cm³ [144]), d_v is the diameter of the virus, and V is the volume of virus suspension passed through one QCM-D chamber that houses the sensor over the duration of the QCM-D tests. The value of d_v was taken to be the MS2 size determined by TEM imaging ($d_v \sim 27$ nm

[145]). The flow rate into one QCM-D chamber was 2.5 mL/h and the total duration of the test 1 h so that the total volume V was 2.5 mL.

Because the concentration of MS2 was measured using the plaque assay method, only viable virus was accounted. Thus, the true upper bound on the *total* (i.e. viable and non-viable) virus mass, which is what was measured in QCM-D tests, is expected to be much higher than the above estimate of 456 ng/cm². Indeed, values > 1250 ng/cm² in QCM-D tests with positively charged surfaces (Figure 14).

Table B1: Contact angles, calculated surface energy parameters, and free energy of the PEMs. Values of ΔG_{sws} are also provided in Table 4 and included here for convenience only.

Notes:

a: 10-[PSS/PDAD]₄; b: 100-[PSS/PDAD]₄; c: 10-[PSS/PDAD]_{4.5}; d: 100-[PSS/PDAD]_{4.5}

e: For all membranes, negative values for $\sqrt{\gamma^+}$ were obtained (see section S1).

PEM Ionic strength for PEM deposition solution (mM)	[PSS/PDAD] ₄		[PSS/PDAD] ₄ [PSS]	
	10 ^a	100 ^b	10 ^c	100 ^d
Contact angle (°) with the indicated probe liquid				
H ₂ O	64.4 ± 2.8	53.2 ± 7.8	29.6 ± 1.5	27.7 ± 2.8
Glycerol	54.1 ± 5.9	59.5 ± 4.7	54.4 ± 3.0	51.8 ± 3.5
Diiodomethane	37.5 ± 3.0	40.3 ± 1.6	23.2 ± 3.1	23.1 ± 1.3
Surface energy parameters (mJ/m ²)				
γ^{LW}	40.8 ± 1.3	39.5 ± 0.2	46.8 ± 1.0	46.8 ± 0.6
γ^{+e}	0.0	0.0	0.0	0.0
γ^-	20.6 ± 2.1	31.9 ± 9.1	60.1 ± 0.1	59.4 ± 7.6
γ^{AB}	0.0	0.0	0.0	0.0
γ^{tot}	40.8 ± 1.3	39.5 ± 0.2	46.8 ± 1.0	46.8 ± 0.6
Free energy of interfacial surface-surface interaction in water ΔG_{sws} (mJ /m ²)	-16.3 ± 2.1	6.9 ± 14.4	45.2 ± 0.6	44.3 ± 10.2

Table B2: Results of XDLVO modeling (values of energy barriers, E_{max} , and secondary energy minima, E_{min} , in XDLVO energy profiles (Figures 12, 13)), and of QCM-D experiments (mass deposition rates for phase 1, $(\frac{dm}{dt})_1$, and phase 2, $(\frac{dm}{dt})_2$, as well as deposition lag time, t_1 (Figures 14, 15)).

Notes:

* Values used as active variables in the PCA (Figure 16a and 16b)

** Values used as supplementary variables in the PCA (Figure 16a)

† The lag time estimated using linear regression (Figures 14 and 15). This time was selected as the start of deposition phase1. Due to the limited duration of the QCM-D test, Phase 2 was not observed. For completeness of PCA calculations (Figure 16), $(\frac{dm}{dt})_2$ in this test was assumed to be equal to $(\frac{dm}{dt})_1$.

Experimental conditions			Predictions and observations						
Experiment code	Ionic strength		Phase 1				Phase 2		
	PEM formation	MS2 deposition	t_1^* min	$(\frac{dm}{dt})_1^*$ (ng/cm ² /min)	$E_{min}^{(1)**}$ (kT)	$E_{max}^{(1)}$ (kT)	$(\frac{dm}{dt})_2^*$ (ng/cm ² /min)	$E_{min}^{(2)**}$ (kT)	$E_{max}^{(2)}$ (kT)
10-[PSS/PDAD] ₄ -10	10	10	0.3	111.7	-2.8	226.6	0.3	-0.1	576.5
100-[PSS/PDAD] ₄ -10	100		0.1	121.0	-9.6	292.9	0.2		
10-[PSS/PDAD] ₄ -100	10	100	0.3	130.6	-0.6	239.3	4.8	-0.5	575.8
100-[PSS/PDAD] ₄ -100	100		0.1	54.6	-0.6	322.0	10.0		
10-[PSS/PDAD] _{4.5} -10	10	10	13.9	0.7 [†]	-0.2	594.3	n/a [†]	-0.1	576.5
100-[PSS/PDAD] _{4.5} -10	100		0	23.5	-0.2	609.0	2.6		
10-[PSS/PDAD] _{4.5} -100	10	100	0	7.8	-0.6	600.5	3.6	-0.5	575.8
100-[PSS/PDAD] _{4.5} -100	100		2.9	10.7	-0.6	610.8	4.5		

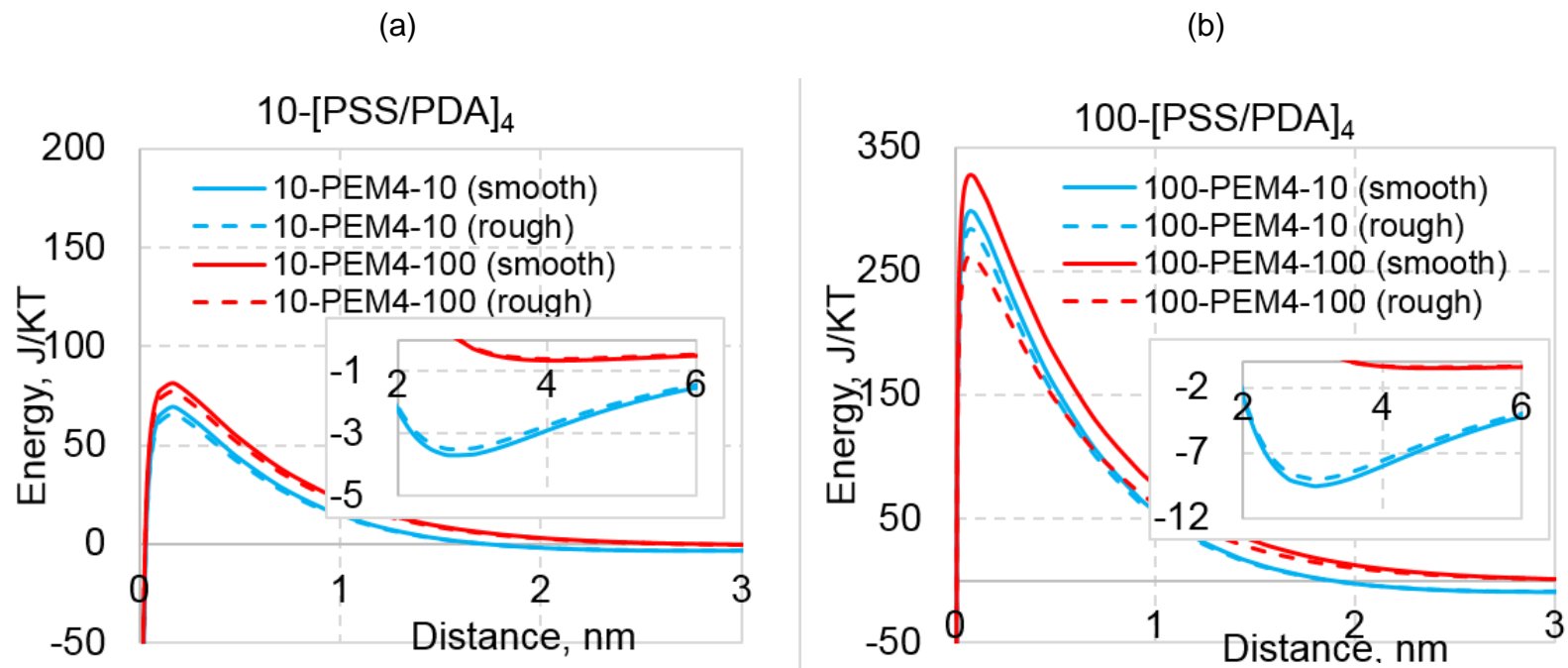


Figure B1: Effect of surface roughness on the of XDLVO energy of interaction between MS2 bacteriophage and PEM surface: a) 10mM[PSS/PDAD]_4 ; b) 100mM[PSS/PDAD]_4 during phase 1 of the deposition process.

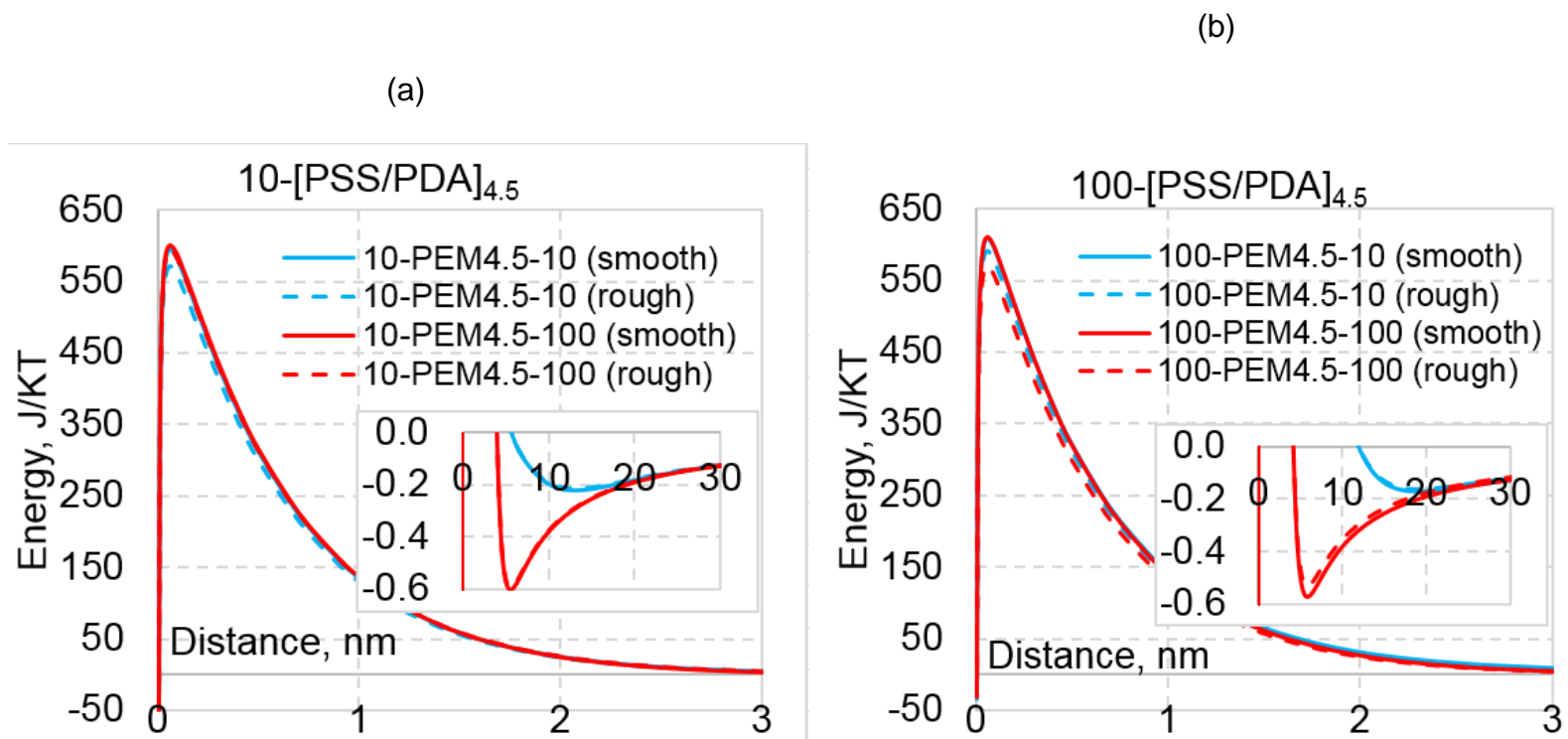


Figure B2: Effect of surface roughness on the of XDLVO energy of interaction between MS2 bacteriophage and PEM surface: a) $10\text{mM}[\text{PSS}/\text{PDAD}]_4[\text{PSS}]$; b) $100\text{mM}[\text{PSS}/\text{PDAD}]_4[\text{PSS}]$ during phase 1 of the deposition process.

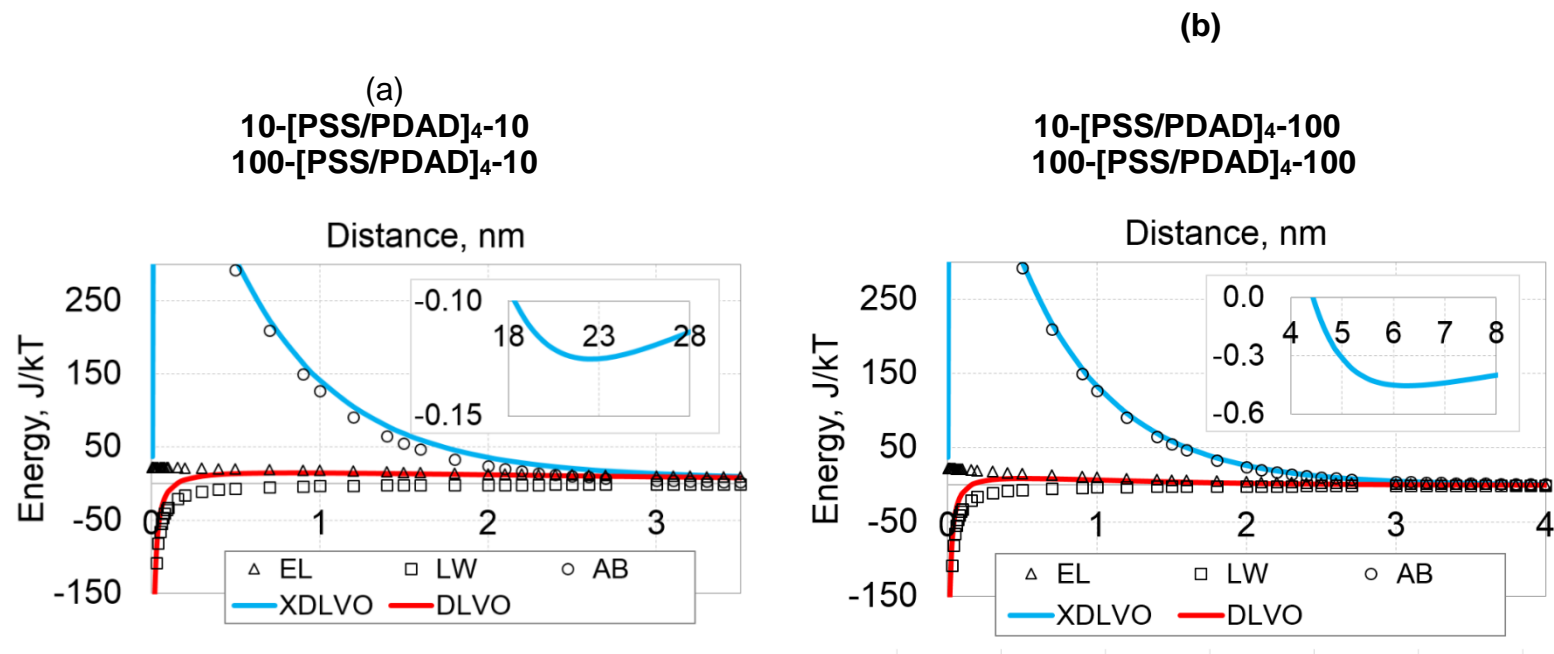


Figure B3: Profiles of XDLVO energy of interaction between MS2 bacteriophage and [PSS/PDAD]₄ surface in a) 10 mM NaCl and b) 100 mM NaCl solutions during phase 2 of the deposition tests. Because this XDLVO calculation is for the case of the interaction between a sphere and smooth flat surface and because the MS2-coated surface is assumed to have the electrical charge and hydrophobicity of MS2, XDLVO profiles are identical for 10-[PSS/PDAD]₄ and 100-[PSS/PDAD]₄ surfaces.

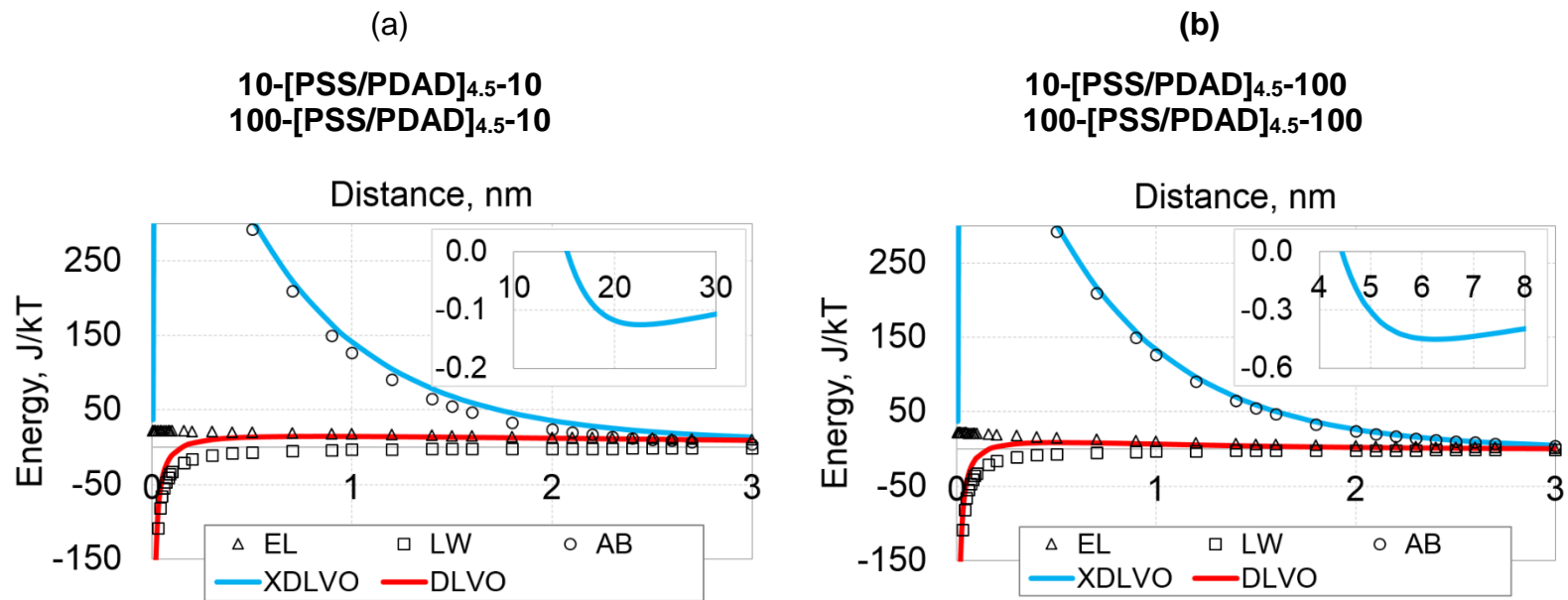


Figure B4: Profiles of XDLVO energy of interaction between MS2 bacteriophage and [PSS/PDAD]_{4.5} surface in a) 10 mM NaCl and b) 100 mM NaCl solutions during phase 2 of the deposition tests.

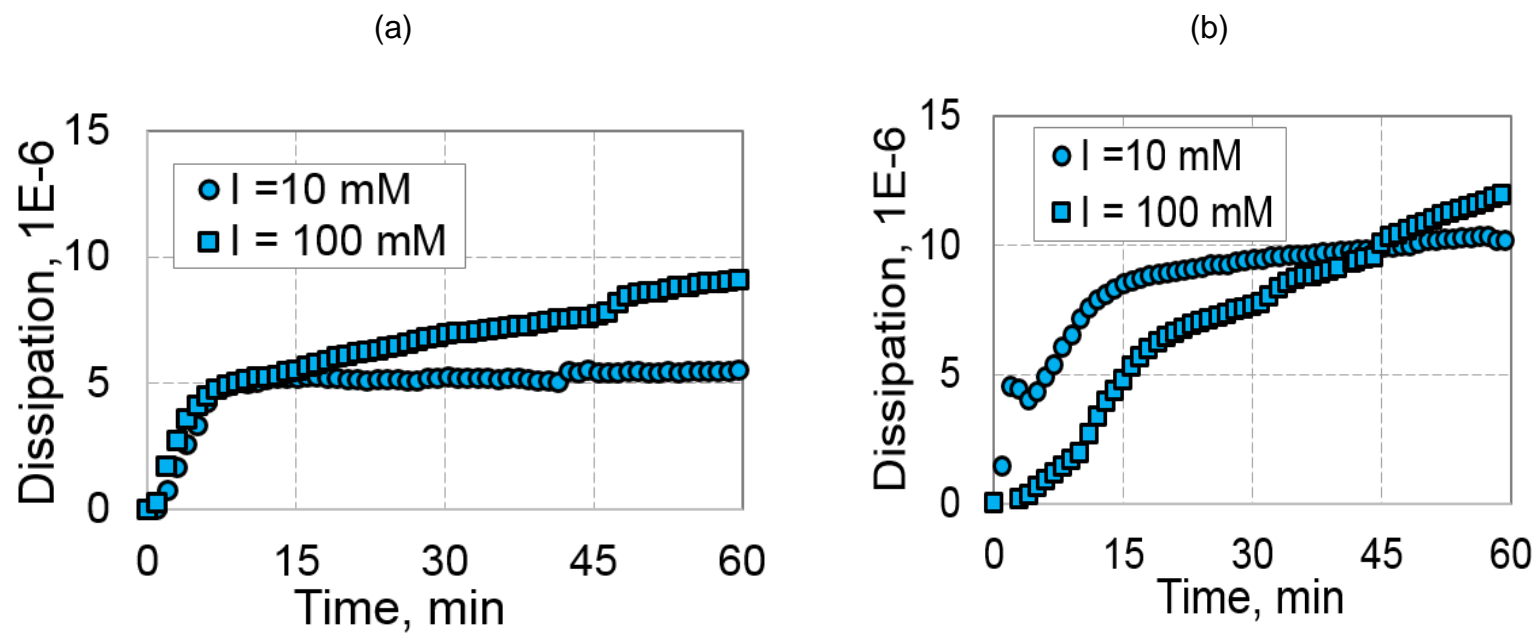


Figure B5: QCM dissipation during MS2 deposition onto (a) 10-[PSS/PDAD]₄, and (b) 100-[PSS/PDAD]₄ surfaces from solutions of different ionic strengths (10 mM or 100 mM NaCl). The dissipation data correspond to mass data show in Figure 14.

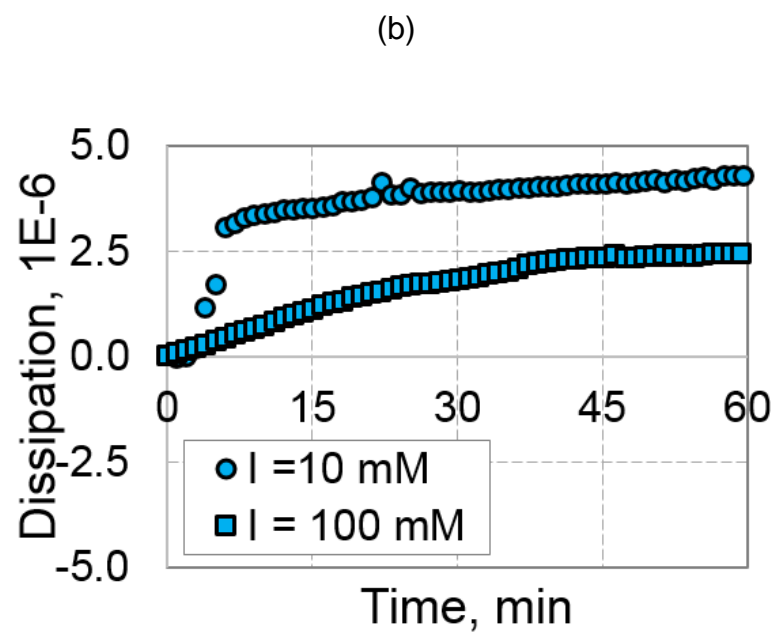
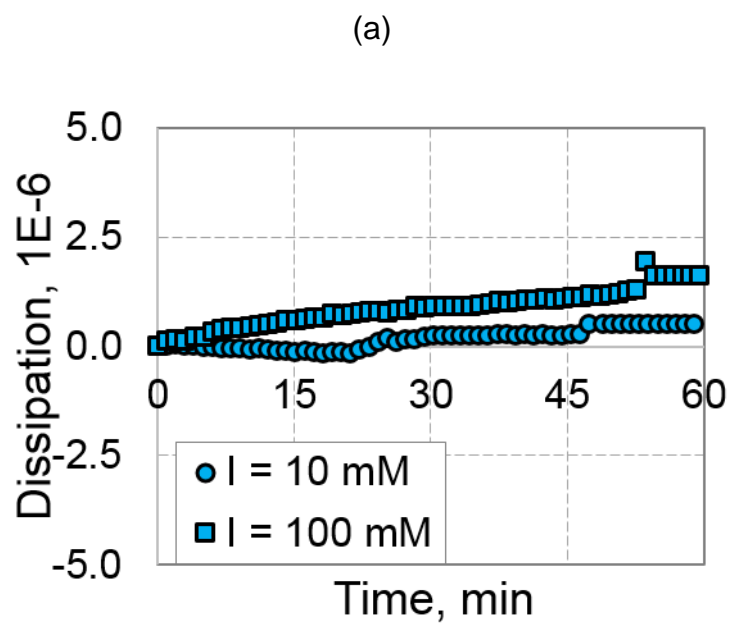


Figure B6: QCM dissipation during MS2 deposition onto (a) 10-[PSS/PDAD]_{4.5} and (b) 100-[PSS/PDAD]_{4.5} surfaces from solutions of different ionic strengths (10 mM or 100 mM NaCl). The dissipation data correspond to mass data show in Figure 15.

BIBLIOGRAPHY

BIBLIOGRAPHY

1. Mead, P.S., et al., *Food-related illness and death in the United States*. Emerg Infect Diseases, 1999. **5**(5): p. 607-625.
2. Sinclair, R.G., E.L. Jones, and C.P. Gerba, *Viruses in recreational water-borne disease outbreaks: a review*. J. Appl. Microbiol., 2009. **107**(6): p. 1769-1780.
3. Rockx, B., et al., *Natural History of Human Calicivirus Infection: A Prospective Cohort Study*. Clin. Infect. Dis., 2002. **35**(3): p. 246-253.
4. Patel, M.M., et al., *Noroviruses: A comprehensive review*. J Clin Virol., 2009. **44**(1): p. 1-8.
5. Fox, J.P., C.E. Hall, and M.K. Cooney, *The Seattle virus watch VII. Observations of adenovirus infections*. Am. J. Epidemiol., 1977. **105**(4): p. 362-386.
6. Gerba, C.P., et al., *Quantitative assessment of the adsorptive behavior of viruses to soils*. Environ. Sci. Technol., 1981. **15**(8): p. 940-944.
7. Tong, M., et al., *Deposition kinetics of MS2 bacteriophages on clay mineral surfaces*. Colloids Surf., B, 2012. **92**(1): p. 340-347.
8. Chrysikopoulos, C.V. and V.I. Syngouna, *Attachment of bacteriophages MS2 and λ X174 onto kaolinite and montmorillonite: Extended-DLVO interactions*. Colloids Surf., B, 2012. **92**: p. 74-83.
9. Yuan, B., M. Pham, and T.H. Nguyen, *Deposition kinetics of bacteriophage MS2 on a silica surface coated with natural organic matter in a radial stagnation point flow cell*. Environ. Sci. Technol., 2008. **42**(20): p. 7628-7633.
10. Armanious, A., et al., *Viruses at solid-water interfaces: a systematic assessment of interactions driving adsorption*. Environ. Sci. Technol., 2015. **50**(2): p. 732-743.
11. Lukasik, J., et al., *Influence of salts on virus adsorption to microporous filters*. Appl. Environ. Microbiol., 2000. **66**(7): p. 2914-2920.
12. Farrah, S.R., *Chemical factors influencing adsorption of bacteriophage MS2 to membrane filters*. Appl. Environ. Microbiol., 1982. **43**(3): p. 659-663.

13. Shi, H., et al., *Elution Is a critical step for recovering human adenovirus 40 from tap water and surface water by cross-flow ultrafiltration*. Appl. Environ. Microbiol., 2016. **82**(16): p. 4982-4993.
14. Shi, H., E.V. Pasco, and V.V. Tarabara, *Membrane-based methods of virus concentration from water: a review of process parameters and their effects on virus recovery*. Environ. Sci. Water Res. Technol., 2017.
15. Cookson, J.T., *Mechanism of virus adsorption on activated carbon*. J. Am. Water. Works. Assoc., 1969. **61**(1): p. 52-56.
16. Cookson, J.T. and W.J. North, *Adsorption of viruses on activated carbon. Equilibriums and kinetics of the attachment of Escherichia coli bacteriophage T4 on activated carbon*. Environ. Sci. Technol., 1967. **1**(1): p. 46-52.
17. Albinana-Gimenez, N., et al., *Comparison of methods for concentrating human adenoviruses, polyomavirus JC and noroviruses in source waters and drinking water using quantitative PCR*. J. Virol. Methods, 2009. **158**(1): p. 104-109.
18. Francy, D.S., et al., *Comparison of filters for concentrating microbial indicators and pathogens in lake water samples*. Appl. Environ. Microbiol., 2013. **79**(4): p. 1342-1352.
19. Gibbons, C., et al., *Evaluation of positively charged alumina nanofibre cartridge filters for the primary concentration of noroviruses, adenoviruses and male-specific coliphages from seawater*. J. Appl. Microbiol., 2010. **109**(2): p. 635-641.
20. Horswell, J., et al., *Mobility and survival of Salmonella Typhimurium and human adenovirus from spiked sewage sludge applied to soil columns*. J. Appl. Microbiol., 2010. **108**(1): p. 104-114.
21. Ikner, L.A., M. Soto-Beltran, and K.R. Bright, *New method using a positively charged microporous filter and ultrafiltration for concentration of viruses from tap water*. Appl. Environ. Microbiol., 2011. **77**(10): p. 3500-3506.
22. Lambertini, E., et al., *Concentration of enteroviruses, adenoviruses, and noroviruses from drinking water by use of glass wool filters*. Appl. Environ. Microbiol., 2008. **74**(10): p. 2990-2996.
23. Li, D., H.-c. Shi, and S.C. Jiang, *Concentration of viruses from environmental waters using nanoalumina fiber filters*. J. Microbiol. Meth., 2010. **81**(1): p. 33-38.

24. McMinn, B.R., *Optimization of adenovirus 40 and 41 recovery from tap water using small disk filters*. J. Virol. Methods, 2013. **193**(2): p. 284-290.
25. Pang, X.L., et al., *Pre-analytical and analytical procedures for the detection of enteric viruses and enterovirus in water samples*. J. Virol. Methods, 2012. **184**(1): p. 77-83.
26. Shi, H., E.V. Pasco, and V.V. Tarabara, *Membrane-based methods of virus concentration from water: a review of process parameters and their effects on virus recovery*. Environ. Sci.: Water Res. Technol., 2017.
27. Sun, S., et al., *Effective concentration, recovery, and detection of infectious adenoviruses from environmental waters*. J. Virol. Methods, 2016. **229**: p. 78-85.
28. Wei, J., et al., *Survival of Human Adenovirus 41 in Land-Applied Manure and Biosolids*. Food Environ. Virol. , 2009. **1**(3): p. 148.
29. Wong, K., D. Bouchard, and M. Molina, *Relative transport of human adenovirus and MS2 in porous media*. Colloids Surf., B, 2014. **122**: p. 778-784.
30. Wong, K., T.C. Voice, and I. Xagorarakis, *Effect of organic carbon on sorption of human adenovirus to soil particles and laboratory containers*. Water Res., 2013. **47**(10): p. 3339-3346.
31. Wu, J., et al., *A simple and novel method for recovering adenovirus 41 in small volumes of source water*. J. Appl. Microbiol., 2011. **110**(5): p. 1332-1340.
32. Chrysikopoulos, C.V. and V.I. Syngouna, *Attachment of bacteriophages MS2 and X174 onto kaolinite and montmorillonite: Extended-DLVO interactions*. Colloids Surf., B, 2012. **92**: p. 74-83.
33. Chattopadhyay, S. and R.W. Puls, *Adsorption of bacteriophages on clay minerals*. Environ. Sci. Technol., 1999. **33**(20): p. 3609-3614.
34. Dowd, S.E., et al., *Delineating the specific influence of virus isoelectric point and size on virus adsorption and transport through sandy soils*. Appl. Environ. Microbiol., 1998. **64**(2): p. 405-410.
35. Penrod, S.L., T.M. Olson, and S.B. Grant, *Deposition kinetics of two viruses in packed beds of quartz granular media*. Langmuir, 1996. **12**(23): p. 5576-5587.

36. Dehghan Monfared, A., et al., *Adsorption of silica nanoparticles onto calcite: Equilibrium, kinetic, thermodynamic and DLVO analysis*. Chem. Eng. J., 2015. **281**: p. 334-344.
37. Ohshima, H., *The Derjaguin–Landau–Verwey–Overbeek (DLVO) Theory of Colloid Stability*, in *Electrical Phenomena at Interfaces and Biointerfaces*. 2012, John Wiley & Sons, Inc. p. 27-34.
38. Brant, J.A. and A.E. Childress, *Assessing short-range membrane-colloid interactions using surface energetics*. J. Membr. Sci., 2002. **203**(1-2): p. 257-273.
39. Van Oss, C.J., M.K. Chaudhury, and R.J. Good, *Interfacial Lifshitz-van der Waals and polar interactions in macroscopic systems*. Chem. Rev., 1988. **88**(6): p. 927-941.
40. Boström M1, W.D., Ninham BW., *Specific ion effects: why DLVO theory fails for biology and colloid systems*. Phys Rev Lett., 2001 Oct. 15. **87**(16).
41. CJ, v.O., *Long-range and short-range mechanisms of hydrophobic attraction and hydrophilic repulsion in specific and aspecific interactions*. J Mol Recognit., 2003 Jul-Aug. **16**(4): p. 177-90.
42. Oss, C.J.v., *Interfacial forces in aqueous media, second edition*. CRC Press. , 2006.
43. Bayouhd, S., et al., *Assessing bacterial adhesion using DLVO and XDLVO theories and the jet impingement technique*. Colloids Surf., B, 2009. **73**(1): p. 1-9.
44. Bayouhd, S., et al., *Assessing bacterial adhesion using DLVO and XDLVO theories and the jet impingement technique*. Colloids Surf. B, 2009. **73**(1): p. 1-9.
45. Lin, H., et al., *A critical review of extracellular polymeric substances (EPSs) in membrane bioreactors: Characteristics, roles in membrane fouling and control strategies*. J. Memb. Sci., 2014. **460**: p. 110-125.
46. Bhattacharjee, S., J.Y. Chen, and M. Elimelech, *DLVO interaction energy between spheroidal particles and a flat surface*. Colloids Surf. A, 2000. **165**(1): p. 143-156.
47. Kidd, A.H., et al., *Adenovirus Type 40 Virions Contain Two Distinct Fibers*. Virology, 1993. **192**(1): p. 73-84.

48. Wong, K., et al., *Influence of Inorganic Ions on Aggregation and Adsorption Behaviors of Human Adenovirus*. Environmental Science & Technology, 2012. **46**(20): p. 11145-11153.
49. Wong, K., D. Bouchard, and M. Molina, *Relative transport of human adenovirus and MS2 in porous media*. Colloids Surf., B, 2014. **122**(Supplement C): p. 778-784.
50. Hoek, E.M.V. and G.K. Agarwal, *Extended DLVO interactions between spherical particles and rough surfaces*. J. Colloid Interface Sci., 2006. **298**(1): p. 50-58.
51. Shen, C., et al., *Coupled factors influencing detachment of nano- and micro-sized particles from primary minima*. J. Contam. Hydrol., 2012. **134**(Supplement C): p. 1-11.
52. Shen, C., et al., *Surface Roughness Effect on Deposition of Nano- and Micro-Sized Colloids in Saturated Columns at Different Solution Ionic Strengths* Vadose Zone J., 2011. **10**(3): p. 1071-1081.
53. Bradford, S.A., et al., *Contributions of Nanoscale Roughness to Anomalous Colloid Retention and Stability Behavior*. Langmuir, 2017. **33**(38): p. 10094-10105.
54. Huang, X., S. Bhattacharjee, and E.M.V. Hoek, *Is Surface Roughness a "Scapegoat" or a Primary Factor When Defining Particle - Substrate Interactions?* Langmuir, 2010. **26**(4): p. 2528-2537.
55. Johannsmann, D., I. Reviakine, and R.P. Richter, *Dissipation in films of adsorbed nanospheres studied by quartz crystal microbalance (QCM)*. Anal. Chem., 2009. **81**(19): p. 8167-8176.
56. Tong, M., et al., *Deposition kinetics of MS2 bacteriophages on clay mineral surfaces*. Colloids Surf., B., 2012. **92**: p. 340-347.
57. Tiliket, G., et al., *Polyethylenimine surface layer for enhanced virus immobilization on cellulose*. Appl. Surf. Sci., 2016. **370**: p. 193-200.
58. Rydell, G.E., et al., *QCM-D studies of human norovirus VLPs binding to glycosphingolipids in supported lipid bilayers reveal strain-specific characteristics*. Glycobiology, 2009. **19**(11): p. 1176-1184.
59. Da Silva, A.K., et al., *Adsorption and aggregation properties of norovirus GI and GII virus-like particles demonstrate differing responses to solution chemistry*. Environ. Sci. Technol., 2010. **45**(2): p. 520-526.

60. Dimitrova, M., et al., *Adenoviral gene delivery from multilayered polyelectrolyte architectures*. *Adv. Funct. Mater.*, 2007. **17**(2): p. 233-245.
61. Steinmetz, N.F., et al., *Assembly of multilayer arrays of viral nanoparticles via biospecific recognition: a quartz crystal microbalance with dissipation monitoring study*. *Biomacromolecules*, 2008. **9**(2): p. 456-462.
62. Huang, X., et al., *Quartz crystal microbalance based biosensor for rapid and sensitive detection of maize chlorotic mottle virus*. *Anal. Methods*, 2014. **6**(13): p. 4530-4536.
63. Lee, J., et al., *Real-time detection of airborne viruses on a mass-sensitive device*. *Appl. Phys. Lett.*, 2008. **93**(1): p. 013901.
64. Armanious, A., et al., *Viruses at solid-water interfaces: a systematic assessment of interactions driving adsorption*. *Environ. Sci. Technol.*, 2015. **50**(2): p. 732-743.
65. Rocholl, C., et al., *Adenoviral infections in children: the impact of rapid diagnosis*. *Pediatrics*, 2004. **113**(1): p. e51-e56.
66. Klepeis, N.E., et al., *The national human activity pattern survey (NHAPS): a resource for assessing exposure to environmental pollutants*. *J. Expo. Sci. Environ. Epidemiol.*, 2001. **11**(3): p. 231.
67. Prussin, A.J., E.B. Garcia, and L.C. Marr, *Total concentrations of virus and bacteria in indoor and outdoor air*. *Environ. Sci. Technol. Lett.*, 2015. **2**(4): p. 84-88.
68. Klevens, R.M., et al., *Estimating health care-associated infections and deaths in US hospitals, 2002*. *Public Health Rep.*, 2007. **122**(2): p. 160-166.
69. Weinstein, R.A., *Epidemiology and control of nosocomial infections in adult intensive care units*. *Am. J. Med.*, 1991. **91**(3): p. S179-S184.
70. Gu, L., et al., *Sustained viremia and high viral load in respiratory tract secretions are predictors for death in immunocompetent adults with adenovirus pneumonia*. *PLOS ONE.*, 2016. **11**(8): p. e0160777.
71. Franz, A., et al., *Correlation of viral load of respiratory pathogens and co-infections with disease severity in children hospitalized for lower respiratory tract infection*. *J. Clin. Virol.*, 2010. **48**(4): p. 239-245.

72. Maggi, F., et al., *TT virus in the nasal secretions of children with acute respiratory diseases: relations to viremia and disease severity*. J. Virol., 2003. **77**(4): p. 2418-2425.
73. Nicas, M., W.W. Nazaroff, and A. Hubbard, *Toward understanding the risk of secondary airborne infection: emission of respirable pathogens*. J. Occup. Environ. Hyg. , 2005. **2**(3): p. 143-154.
74. Xie, X., et al., *How far droplets can move in indoor environments - revisiting the Wells evaporation - falling curve*. Indoor Air., 2007. **17**(3): p. 211-225.
75. Yang, W. and L.C. Marr, *Dynamics of airborne influenza A viruses indoors and dependence on humidity*. PLOS ONE., 2011. **6**(6): p. e21481.
76. Lu, R., D. Mosiman, and T.H. Nguyen, *Mechanisms of MS2 bacteriophage removal by fouled ultrafiltration membrane subjected to different cleaning methods*. Environ. Sci. Technol., 2013. **47**(23): p. 13422-13429.
77. Dika, C., et al., *Impact of the virus purification protocol on aggregation and electrokinetics of MS2 phages and corresponding virus-like particles*. Phys. Chem. Chem. Phys., 2013. **15**(15): p. 5691-5700.
78. Langlet, J., F. Gaboriaud, and C. Gantzer, *Effects of pH on plaque forming unit counts and aggregation of MS2 bacteriophage*. J. Appl. Microbiol., 2007. **103**(5): p. 1632-1638.
79. Effros RM, H.K., Bosbous M, Castillo D, Foss B, Dunning M, Gare M, Lin W, Sun F., *Dilution of respiratory solutes in exhaled condensates*. Am. J. Respir. Crit. Care. Med., 2002 **165**(5): p. 663-9.
80. Walsh, B.K., et al., *Exhaled-breath condensate pH can be safely and continuously monitored in mechanically ventilated patients*. Respir. Care., 2006. **51**(10): p. 1125-1131.
81. Bikov, A., et al., *Exhaled breath condensate pH is influenced by respiratory droplet dilution*. J. Breath Res., 2012. **6**(4): p. 046002.
82. Hunt, J.F., et al., *Endogenous airway acidification: implications for asthma pathophysiology*. Am. J. Respir. Crit. Care Med. , 2000. **161**(3): p. 694-699.
83. Gessner, C., et al., *Exhaled breath condensate acidification in acute lung injury*. Respir. Care., 2003. **97**(11): p. 1188-1194.

84. Yang, W., S. Elankumaran, and L.C. Marr, *Relationship between humidity and influenza A viability in droplets and implications for influenza's seasonality*. PLOS ONE., 2012. **7**(10): p. e46789.
85. Meduri, G.U., et al., *Noninvasive face mask ventilation in patients with acute respiratory failure*. Chest., 1989. **95**(4): p. 865-870.
86. BEHR, *Technical data sheet : Alkyd semi-gloss enamel white base No. 3900*. BEHR, 2017.
87. BEHR, *Technical data sheet : BEHR marquee exterior semi-gloss enamel paint No. 5450*. BEHR, 2016.
88. BEHR, *Technical data sheet : Oil-base interior / exterior semi-gloss enamel No. 3800*. BEHR, 2016.
89. BEHR, *Safety data sheet : Alkyd semi-gloss enamel white base No. 3900*. BEHR, 2016.
90. BEHR, *Safety data sheet : BEHR marquee exterior semi-gloss ultra pure white No. 5450*., BEHR, 2016.
91. BEHR, *Safety data sheet : Oil-based interior / exterior semi-gloss enamel white No. 3800*. BEHR 2016.
92. Sauerbrey, G., *Verwendung von Schwingquarzen zur Wägung dünner Schichten und zur Mikrowägung*. Z. Phys., 1959. **155**(2): p. 206-222.
93. Van der Mei, H.C., R. Bos, and H.J. Busscher, *A reference guide to microbial cell surface hydrophobicity based on contact angles*. Colloids Surf., B, 1998. **11**(4): p. 213-221.
94. Hwang, G., et al., *Determination of reliable Lewis acid-base surface tension components of a solid in LW-AB approach*. J. Ind. Eng. Chem., 2011. **17**(1): p. 125-129.
95. Langlet, J., et al., *Aggregation and surface properties of F-specific RNA phages: implication for membrane filtration processes*. Water Res., 2008. **42**(10): p. 2769-2777.
96. Dixon, M.C., *Quartz crystal microbalance with dissipation monitoring: Enabling real -time characterization of biological materials and their interactions*. J. Biomol. Tech., 2008. **19**(3): p. 151-158.

97. Dika, C., et al., *Isoelectric point is an inadequate descriptor of MS2, Phi X 174 and PRD1 phages adhesion on abiotic surfaces*. *J. Colloid. Interface. Sci.*, 2015. **446**: p. 327-334.
98. Dika, C., et al., *Non-DLVO adhesion of F-specific RNA bacteriophages to abiotic surfaces: importance of surface roughness, hydrophobic and electrostatic interactions*. *Colloids Surf., A*, 2013. **435**: p. 178-187.
99. Patel, M.M., et al., *Noroviruses: A comprehensive review*. *J. Clin. Virol.*, 2009. **44**(1): p. 1-8.
100. Patel, M.M., et al., *Systematic literature review of role of noroviruses in sporadic gastroenteritis*. *Emerg. Infect. Dis.*, 2008. **14**(8): p. 1224-1231.
101. Dawson, D., et al., *Survival of viruses on fresh produce, using MS2 as a surrogate for norovirus*. *J. Appl. Microbiol.*, 2005. **98**(1): p. 203-209.
102. Dika, C., et al., *Isoelectric point is an inadequate descriptor of MS2, Phi X 174 and PRD1 phages adhesion on abiotic surfaces*. *J. Colloid Interface Sci.*, 2015. **446**: p. 327-334.
103. Tong, M., et al., *Deposition kinetics of MS2 bacteriophages on clay mineral surfaces*. *Colloids Surf. B*, 2012. **92**: p. 340-347.
104. Pham, M., E.A. Mintz, and T.H. Nguyen, *Deposition kinetics of bacteriophage MS2 to natural organic matter: Role of divalent cations*. *J. Colloid Interface Sci.*, 2009. **338**(1): p. 1-9.
105. Shi, H., E.V. Pasco, and V.V. Tarabara, *Membrane-based methods of virus concentration from water: a review of process parameters and their effects on virus recovery*. *Environ. Sci. Water Res. Technol.*, 2017. **3**(5): p. 778-792.
106. Syngouna, V.I. and C.V. Chrysikopoulos, *Cotransport of clay colloids and viruses in water saturated porous media*. *Colloids Surf. A*, 2013. **416**: p. 56-65.
107. Wong, K., D. Bouchard, and M. Molina, *Relative transport of human adenovirus and MS2 in porous media*. *Colloids Surf. B*, 2014. **122**: p. 778-784.
108. White, N., et al., *Highly selective separations of multivalent and monovalent cations in electrodialysis through Nafion membranes coated with polyelectrolyte multilayers*. *Polymer*, 2016. **103**: p. 478-485.

109. Ahmadiannamini, P., M.L. Bruening, and V.V. Tarabara, *Sacrificial polyelectrolyte multilayer coatings as an approach to membrane fouling control: disassembly and regeneration mechanisms*. J. Membr. Sci., 2015. **491**: p. 149-158.
110. Shan, W., et al., *Polyelectrolyte multilayer films as backflushable nanofiltration membranes with tunable hydrophilicity and surface charge*. J. Membr. Sci., 2010. **349**(1): p. 268-278.
111. Ishigami, T., et al., *Fouling reduction of reverse osmosis membrane by surface modification via layer-by-layer assembly*. Sep. Purif. Technol., 2012. **99**: p. 1-7.
112. Shi H, X.I., Parent KN, Bruening ML, Tarabara VV, *Elution is a critical step for recovering human adenovirus 40 from tap water and surface water by cross-flow ultrafiltration*. Appl Environ Microbiol 2016. **82**: p. 4982–4993.
113. Pasco, E.V., et al., *Polyelectrolyte multilayers as anti-adhesive membrane coatings for virus concentration and recovery*. J. Membr. Sci., 2014. **469**: p. 140-150.
114. Miller, M.D. and M.L. Bruening, *Correlation of the swelling and permeability of polyelectrolyte multilayer films*. Chem. Mater., 2005. **17**(21): p. 5375-5381.
115. Baba, A., F. Kaneko, and R.C. Advincula, *Polyelectrolyte adsorption processes characterized in situ using the quartz crystal microbalance technique: alternate adsorption properties in ultrathin polymer films*. Colloids Surf., A., 2000. **173**(1): p. 39-49.
116. Poptoshev, E., B. Schoeler, and F. Caruso, *Influence of solvent quality on the growth of polyelectrolyte multilayers*. Langmuir, 2004. **20**(3): p. 829-834.
117. Dubas, S.T. and J.B. Schlenoff, *Factors controlling the growth of polyelectrolyte multilayers*. Macromolecules, 1999. **32**(24): p. 8153-8160.
118. Serizawa, T., S. Kamimura, and M. Akashi, *Electrostatic adsorption of polystyrene particles with different surface charges onto the surface of an ultrathin polymer film*. Colloids Surf., A., 2000. **164**(2): p. 237-245.
119. Tong, M., et al., *Deposition kinetics of MS2 bacteriophages on clay mineral surfaces*. Colloids Surf., B, 2012. **92**: p. 340-347.
120. ATCC, *Product sheet : MS2 bacteriophage (ATCC 15597-B1)*. ATCC, 2013.

121. Hoogeveen, N.G., et al., *Formation and Stability of Multilayers of Polyelectrolytes*. Langmuir, 1996. **12**(15): p. 3675-3681.
122. Elźbieciak-Wodka, M., et al., *Comparison of permeability of poly(allylamine hydrochloride)/and poly(diallyldimethylammonium chloride)/poly(4-styrenesulfonate) multilayer films: Linear vs. exponential growth*. J. Electroanal. Chem, 2015. **738**: p. 195-202.
123. Segre, J.A., *Epidermal barrier formation and recovery in skin disorders*. Journal of Clinical Investigation, 2006. **116**(5): p. 1150-1158.
124. Grice, E.A., et al., *A diversity profile of the human skin microbiota*. Genome Research, 2008. **18**(7): p. 1043-1050.
125. Foulongne, V., et al., *Human Skin Microbiota: High Diversity of DNA Viruses Identified on the Human Skin by High Throughput Sequencing*. PLOS ONE, 2012. **7**(6): p. e38499.
126. Hamel R, D.O., Wichit S, Ekchariyawat P, Neyret A, Luplertlop N, Perera-Lecoin M, Surasombatpattana P, Talignani L, Thomas F, Cao-Lormeau V-M, Choumet V, Briant L, Desprès P, Amara A, Yssel H, Missé D, *Biology of Zika virus infection in human skin cells*. J Virol 2015. **89**: p. 8880–8896.
127. Wu, S.-J.L., et al., *Human skin Langerhans cells are targets of dengue virus infection*. Nature Medicine, 2000. **6**: p. 816.
128. Whitley, R.J. and B. Roizman, *Herpes simplex virus infections*. The Lancet, 2001. **357**(9267): p. 1513-1518.
129. Paulino, L.C., et al., *Molecular Analysis of Fungal Microbiota in Samples from Healthy Human Skin and Psoriatic Lesions*. Journal of Clinical Microbiology, 2006. **44**(8): p. 2933-2941.
130. R. R. Roth, W.D.J., *Microbial ecology of the skin*. Annu Rev Microbiol., 1988. **42**: p. 441–464.
131. Nickoloff, B.J. and F.O. Nestle, *Recent insights into the immunopathogenesis of psoriasis provide new therapeutic opportunities*. Journal of Clinical Investigation, 2004. **113**(12): p. 1664-1675.
132. Palmer, C.N.A., et al., *Common loss-of-function variants of the epidermal barrier protein filaggrin are a major predisposing factor for atopic dermatitis*. Nature Genetics, 2006. **38**: p. 441.

133. Grice, E.A. and J.A. Segre, *The skin microbiome*. Nature Reviews Microbiology, 2011. **9**: p. 244.
134. Till, A.E., et al., *The cutaneous microflora of adolescent, persistent and late-onset acne patients does not differ*. British Journal of Dermatology, 2000. **142**(5): p. 885-892.
135. Antonsson, A., et al., *Prevalence and type spectrum of human papillomaviruses in healthy skin samples collected in three continents*. Journal of General Virology, 2003. **84**(7): p. 1881-1886.
136. Esiri, M.M. and A.H. Tomlinson, *Herpes simplex encephalitis: Immunohistological demonstration of spread of virus via olfactory and trigeminal pathways after infection of facial skin in mice*. Journal of the Neurological Sciences, 1984. **64**(2): p. 213-217.
137. Pack, L.D., et al., *Microbial contamination associated with mascara use*. Optometry - Journal of the American Optometric Association, 2008. **79**(10): p. 587-593.
138. Smart, R. and D. F. Spooner, *Microbial spoilage in Pharmaceuticals and cosmetics*. J. Soc. Cosmet. Chem. 1972.
139. Abu Shaqra, Q.M. and R.M. Al-Groom, *Microbiological quality of hair and skin care cosmetics manufactured in Jordan*. International Biodeterioration & Biodegradation, 2012. **69**(Supplement C): p. 69-72.
140. Stephanie Wong, D.S., Sonia I. Delgado, Karl C. Klontz, *Recalls of Foods and Cosmetics Due to Microbial Contamination Reported to the U.S. Food and Drug Administration*. Journal of Food Protection, 2000. **63**(8): p. 1113-1116.
141. van Oss, C.J., *Interfacial forces in aqueous media*. 2006, Boca Raton: Taylor & Francis.
142. Van der Mei, H.C., R. Bos, and H.J. Busscher, *A reference guide to microbial cell surface hydrophobicity based on contact angles*. Colloids Surf. B, 1998. **11**(4): p. 213-221.
143. *Personal communication with Dr. Archana Jaiswal, Principal Application Scientist (Biolin Scientific Inc.). April 13, 2018.*
144. Strauss, J.H. and R.L. Sinsheimer, *Purification and properties of bacteriophage MS2 and of its ribonucleic acid*. J. Mol. Biol., 1963. **7**: p. 43-54.

145. Shi, H. and V.V. Tarabara, *Charge, size distribution and hydrophobicity of viruses: Effect of propagation and purification methods*. J. Virol. Methods, 2018. **256**: p. 123-132.